A Mössbauer spectroscopy study of Fe based cemented carbides

Gerrard Soobramoney Peters

A dissertation submitted to the Faculty of Science, University of the Witwatersrand, Johannesburg, in fulfilment of the academic requirements for the degree of Master of Science

Johannesburg
March 2018

Declaration

The measurements described in this dissertation were carried out at the University of the Witwatersrand. The processing and fabrication of the materials were performed at Pilot Tools (Pty) Ltd, Johannesburg, South Africa.

The data analysis and understanding of results is my original work and was carried out under the guidance of Professor Deena Naidoo (supervisor) and Dr Hilary Masenda (co-supervisor).

The work of other scientists is duly acknowledged when they are used in this dissertation.

I declare that this dissertation has not been submitted before for any degree or diploma examination in any other tertiary institution.

Gerrard Soobramoney Peters

28th March 2018

Abstract

In the cemented carbide industry, there are increasing demands to produce tungsten carbide (WC) tools with higher cutting speeds, and improved wear and corrosion resistance. Currently there are concentrated research efforts to find an alternative binder to cobalt (Co) in WC-Co alloys, due to its toxicity, availability, and strong price fluctuations. Iron (Fe) and nickel (Ni) binder alloys are envisaged as suitable replacements for Co, and are currently only used in very limited applications, which still warrants further research.

Mössbauer spectroscopic studies were performed on 10 wt% Fe, and Fe alloy binder cemented carbides (WC-Fe, WC-Fe/Ni and WC-Fe/Mn) to determine the Fe charge state, Fe complexes and hyperfine interaction parameters with the aim of understanding the role of different phases, structural changes and magnetic effects of the binder alloy.

The materials were sintered at three different temperatures (1340 °C, 1430 °C and 1510 °C), and are within the desired stoichiometric range for the Fe based cemented carbides as indicated by X-ray diffraction (XRD) and magnetic saturation results, except for the WC-FeMn grade sintered at the lowest temperature. This material contained a sub-stoichiometric phase (η-phase) due to oxidation of samples prior to sintering. X-ray diffraction results indicate only WC and the metal binder phase present in the materials. The WC-10Fe grade has the highest Vickers hardness measured using a 30 kg load, ranging from 1282 to 1320 HV_{30}, across the different sintering temperatures. The hardness of the WC-FeNi grade sintered at 1430 °C, 1250 HV_{30}, is similar to a WC-10Co grade sintered at the same temperature.

Transmission Mössbauer Spectroscopy (TMS) results show only α-Fe present in all the milled powders with a hyperfine magnetic field of ≈33 T. There is no evidence of iron oxide phases in the milled powders, suggesting that no oxidation takes place during the powder processing processes. Conversion electron Mössbauer Spectroscopy (CEMS) on the sintered WC-Fe grades show two magnetic fields present with hyperfine fields of ≈33 T and ≈17 T. These fields can be assigned to α-FeW and (FeW)C phases, respectively.

The CEMS spectrum for the lowest temperature (1340 °C) FeNi binder sample shows a paramagnetic doublet (δ = −0.08 mm/s and ΔE_Q = 0.00 mm/s) occupying 65% of the total area, and a weak magnetic field (15.7 T). The doublet was assigned to γ-FeNi and the magnetic component to γ-(FeNiW)C. At the higher sintering temperatures, the paramagnetic doublet is suppressed to ≈5% of the total area, and the remainder of the Mössbauer spectrum is characterised by a distribution of magnetic fields (33 T, 25 T and 9 T). These magnetic fields are tentatively assigned to γ-FeNi and multiple phases of FeNiW.

The η-phase present in the WC-FeMn material sintered at 1340 °C is identified by XRD as Fe_2W_2C, and is observed as a paramagnetic single line in the Mössbauer spectrum, with a positive isomer shift of 0.23 mm/s. The Mössbauer spectrum also shows a distribution of magnetic components having a range of magnetic fields (32.5 T, 31.3 T and 30.2 T). These sextets occupy 97% of the total area, and are possibly α-FeMn (32.5 T) and α-FeMnW phases. The increase in magnetic fields (B_{hf} = 35.3 and B_{hf} = 34.0 T) for the WC-FeMn sample sintered at the highest temperature of 1510 °C, could be the result of complex phases of disordered α-FeMn (W) present in the material.

The findings of this study confirm that Fe-based binder systems have better hardness properties than Co binders in cemented carbide alloys. In addition, Conversion electron Mössbauer Spectroscopy was utilised as a new investigative tool to obtain information of Fe based complex phases in the materials under study which are not easily detected by other spectroscopic techniques e.g. X-Ray Diffraction. The CEMS results can be useful in elucidating information on the fabrication process and/or material design of Fe-based cemented carbides i.e. composition of the material and sintering temperature.

Dedication

In memory of my mother:

Betty "Baby" Peters

13/02/1933 – 28/11/2012

- *Also to Meenoo and the kids for their patience and support.*

Acknowledgements

I wish to express my sincere gratitude and appreciation to my supervisor, Professor Deena Naidoo, who encouraged me to further my studies and also made it all possible. Thank you for your effort, time and support you gave me, other than mentoring, supervising and guiding this project. I am also greatly indebted to you for your valuable contributions, guidance and assistance with the data analysis and the writing of this dissertation.

My sincere thanks to my co-supervisor, Dr Hilary Masenda, for your guidance and assistance with this project as well as the valuable contributions in formatting this document. Thank you for the comments and valuable suggestions after reading through the many drafts.

I am extremely grateful to the management at Pilot Tools (Pty) Ltd, South Africa and Dr Christopher Freemantle for allowing me full access to their production facilities for fabricating the materials for this work, as well as their laboratory facilities for the routine quality control testing.

Thanks to Dr Stuart Miller and Mr Adam Shiner for their assistance with XRD measurements, and to Prof Daniel Wamwangi for assisting with the XRD data interpretation.

Thank you to Ndivhuwo Bryner Nelwalani for assisting with the SEM examination, and to Dr Rodney Genga for your advice and encouragement.

I am grateful to the School of Physics and Centre of Excellence in Strong Materials for allowing me the opportunity to pursue my postgraduate studies. Thank you to the Faculty of Science for supporting my studies. A special thank you to Mr Charles Sandrock for carrying the workload for the duration of my studies.

A very special thank you to my partner, Meenoo, for your sacrifice, and all the love and encouragement you gave me. Also to my spiritual mother, Mumsy, thank you for your guidance and prayers.

Table of Contents

List of Figures

List of Tables

Chapter 1

Introduction

1.1 Background

Tungsten carbide (WC) based hardmetals or cemented carbides consist of very hard WC particles embedded in a ductile metal binder, typically cobalt (Co). Cemented carbides are used extensively in applications requiring high wear resistance, such as metal cutting, drilling, wire drawing and metal forming. The high hardness and moderate toughness of the composite material provides excellent wear resistant properties. Since the early development of WC hardmetals in 1923 [1], Co has always been the preferred metal binder because of its unique properties. These qualities include good wetting behaviour [2], favorable solubility with WC, and good mechanical properties. Other metals, specifically nickel (Ni) and iron (Fe) are also used as binders in very limited and specialised applications where hot hardness (hardness of the material at elevated temperatures), thermal resistance and corrosion or oxidation resistance are required [3].

The limitations of Co as a metal binder in cemented carbides include its low melting temperature and relatively low hot hardness which result in rapid degradation during high speed machining operations. The hardness of WC-11Co having a grain size of 1.3 μm [4], decreases from 15 GPa at room temperature to 7 GPa at about 900 °C. In industry, there is constant pressure for increased cutting speeds which result in harsher machining conditions where temperatures in excess of 1000 °C are generated. As WC-Co cutting tools have a low hot hardness at these temperatures, they fail prematurely as a result of increased chemical wear. Cobalt binders are also corrosive, and oxidise in drilling and in high speed cutting applications, where lubricants are used, and where high temperatures are generated. Cobalt is also toxic [5], and as a politically strategic material, it can be subject to significant price fluctuations and availability.

At the 18th Plansee Seminar in 2013, Norgren *et al.* [6] presented a paper on the global trends in the Powder Metallurgy Hardmetals industry, which identified

alternate binders to Co as one of the focus areas which required further research and development due to health risks related to the use of Co in the hardmetals industry. The new European Community Regulation on chemicals and safe usage thereof, known as the REACH programme has classified Co as very toxic for human health. In addition, the United States National Toxicology Program (NTP) suggests that hardmetal (WC-Co) dust is more toxic than either cobalt or WC. This has resulted in an increase of activity to find alternatives to the Co binder in hardmetals.

Metal binders such as Fe and Ni alloys were identified as potential replacements for Co, however further development of alternate binders are required to compete with Co binders in its wide range of applications and production advantages. The following issues have been identified in Fe based binder systems: (a) the difficulty in controlling the carbon balance for achieving defect free structures, (b) the tendency of Fe to form martensite and other phases (phase transformations) during cooling, (c) a lower transverse rupture strength and, (d) problems associated in using conventional production and standard quality control testing methods (magnetic saturation for example).

1.2 Literature Review

1.2.1 Phase Equilibria

Thermodynamic modelling [6] is used for the fundamental understanding and development of new carbide grades. It is based on calculation of the Gibbs free energy of individual phases which is implemented into software packages used for phase diagram calculations. In hardmetal systems, the software programs provide predictions such as stability regions, melting ranges, carbon balances and recipes. The carbon balance in cemented carbide production is crucial for obtaining a stoichiometric composition after sintering.

1.2.1.1 WC-Co system

In hardmetals, W-Co-C phase equilibria is the most extensively analysed system both experimentally, and by thermodynamic calculations [4,7]. For W/C atomic

ratios that are close to 1, the stable phases are WC + β, where β = Co metal binder with an fcc crystal structure. The favourable two-phase region, WC + β only exist in a narrow carbon window between 5.40 and 5.55 wt% C as indicated by the red lines in Figure 1.1. This window is the desired stoichiometric composition range which is targeted for optimal properties. At lower carbon concentrations, the brittle eta-phase (η-phase) is formed in the 3-phase region WC + β + η. The sub-stoichiometric eta-phase can exist in a variety of compositions, and these are generally grouped into two families or classes, namely, $M_{12}C$ and M_6C (MC = metal carbide). In the WC-Co system, M_6C includes Co_3W_3C and Co_2W_4C phase compositions. The formation of other ternary phases of W_2C will only occur at much lower carbon levels, or very low Co content. At W/C atomic ratios below 1, primary carbon (graphite) will precipitate and remain in equilibrium with the WC and β in solidified alloys. This is the 3-phase region (WC + β + Graphite) to the right of the stoichiometric composition, WC + β (fcc), as shown in Figure 1.1.

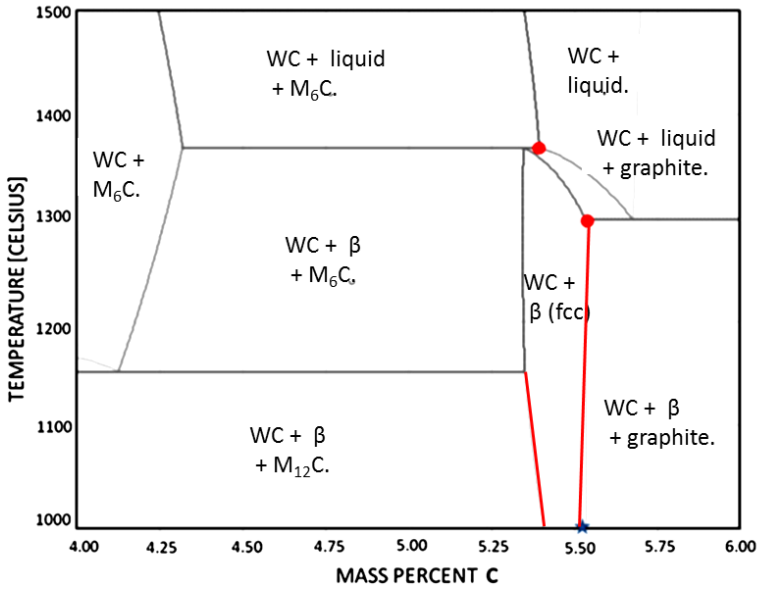

Figure 1.1: Vertical section of the Co-W-C phase diagram calculated for 10 wt% Co [1].

1.2.1.2 WC-Fe system

The phase relationships in the W-Fe-C system [7] seem to be very similar to the W-Co-C system. A vertical section of the W-Fe-C system is shown in Figure 1.2 for a 10 wt% Fe binder concentration. The stoichiometric phase field is shifted to the right in comparison to the Co system (Figure 1.1) with the minimum carbon level at 5.55 wt%. Unlike cobalt, iron is a carbide former [8] and hence, a carbon-rich composition is necessary, which is still difficult to control through the narrow two-phase stoichiometric region. Iron has a magnetic [7] bcc crystal structure (α-Fe) that can only dissolve 0.021 wt% C at 910 °C. For the temperature range 912 °C - 1400 °C, a phase transformation of Fe from bcc (α-Fe) to fcc (γ-Fe) take place. The γ-Fe phase is non-magnetic which can dissolve significantly more carbon, up to 2.14 wt% at 1146 °C.

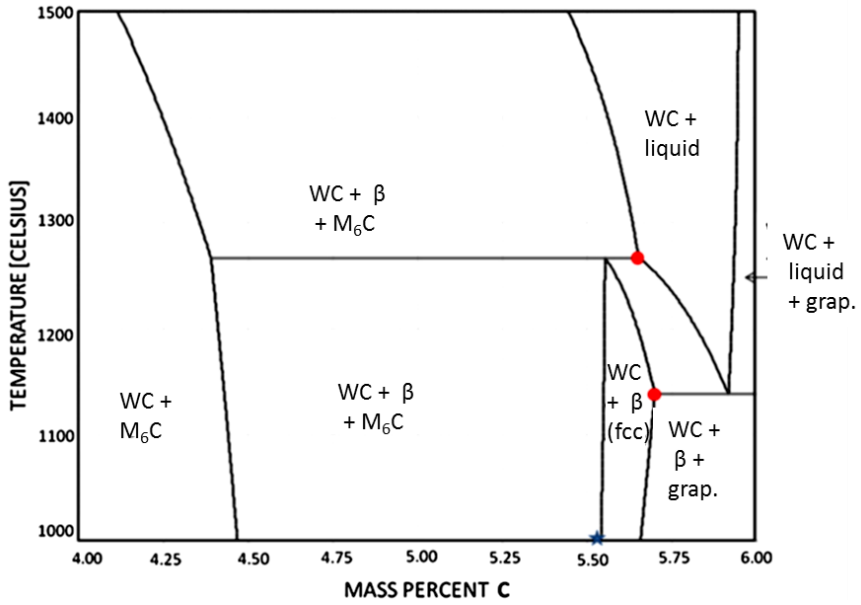

Figure 1.2: Vertical section of the W-Fe-C phase diagram calculated for 10 wt% Fe [1].

In Fe binder systems [9], tungsten as an alloying element facilitates martensitic transformation during cooling, particularly in the presence of Ni and Mn. However, the solubility of WC in Fe is much lower at its eutectic temperature of 1143 °C compared to Co which has a eutectic temperature of 1320 °C.

1.2.1.3 WC-Fe-Ni system

Thermodynamic calculations [9] as a function of temperature and composition of a 20 wt% FeNi binder show a general increase in the eutectic temperature when the Ni ratio is increased. The favourable stoichiometric field [10] fcc + WC occurs at lower carbon contents relating to the stoichiometric composition as shown in Figure 1.3. In a 3:1 Fe:Ni ratio, M_6C phases form at 1350 °C even in a stoichiometric composition. Although the alloy would reach a stable two-phase field (WC + fcc) on cooling, the M_6C precipitates remain in a metastable state suggesting that a higher carbon content of 5.1 wt% is required to avoid M_6C precipitation. For lower binder contents, 10 wt% FeNi, the two-phase (stoichiometric region) field becomes narrower. Increasing the Fe content in the binder displaces the two-phase field to higher carbon contents and lowers the liquidus temperature.

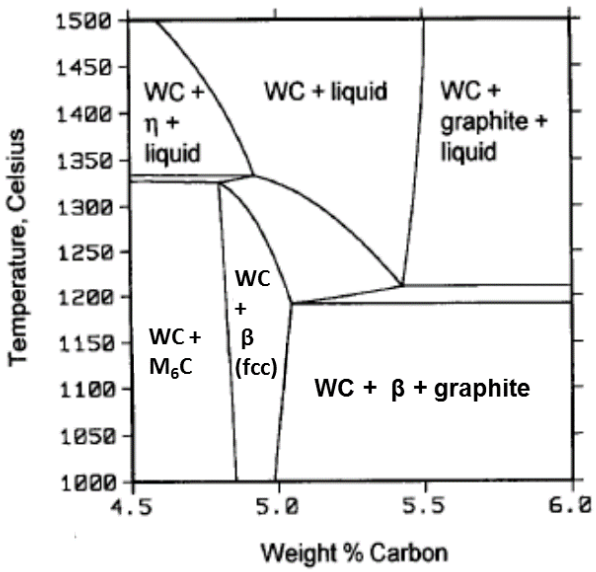

Figure 1.3: Vertical section of the Fe-Ni-W-C phase diagram calculated for 20 wt% 1:1 FeNi [10].

1.2.1.4 WC-Fe/Mn system

Cemented carbides with Fe-Mn binders are reported [2] to have similar characteristics to Co binders pertaining to melting temperature, crystal structure and γ (fcc) → ε (hcp) phase transformation on cooling. Manganese is an austenite

stabiliser and Fe-Mn binders containing 13.5 wt% Mn can retain fully or partially austenitic (γ) structures at room temperature. Studies by Maccio *et al*. [8] of the Fe-Mn-W-C phase diagram show that M_6C formation during sintering is a major challenge as WC + fcc field is enclosed by a three-phase field of WC + liquid + M_6C as shown in Figure 1.4 for a 20 wt% binder (Fe-Mn) composition. This suggests that sintering parameters such as temperature and cooling rate must be carefully controlled to prevent the formation of M_6C. Cementite (M_3C) is predicted [8, 11] for slightly higher carbon contents.

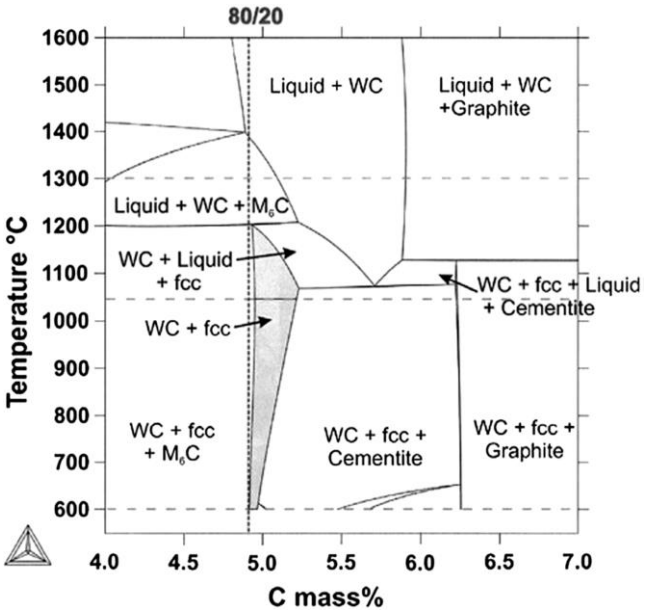

Figure 1.4: Vertical section of the Fe-Mn-W-C phase diagram calculated for 20 wt% Fe-Mn [8].

1.2.1.5 WC-Ni system

The structure and properties of Ni [12] are similar to cobalt and the lattice parameter of fcc Ni is marginally lower than fcc Co. To obtain satisfactory densification, higher sintering temperatures are required for sintering WC-Ni alloys even though the melting point of Ni (1455 °C) is lower than that of Co (1495 °C). Thermodynamic calculation of the W-C-Ni phase diagram show that the width of two-phase field (WC + β) is similar to that of W-C-Co, however the field is shifted

towards lower carbon contents as shown in Figure 1.5. During sintering the stoichiometric composition of WC-Ni is within the two-phase field, but graphite precipitation occurs on cooling. This situation is opposite to Fe binders, and hence Fe-Ni binders are considered more favourable in obtaining stoichiometric composition.

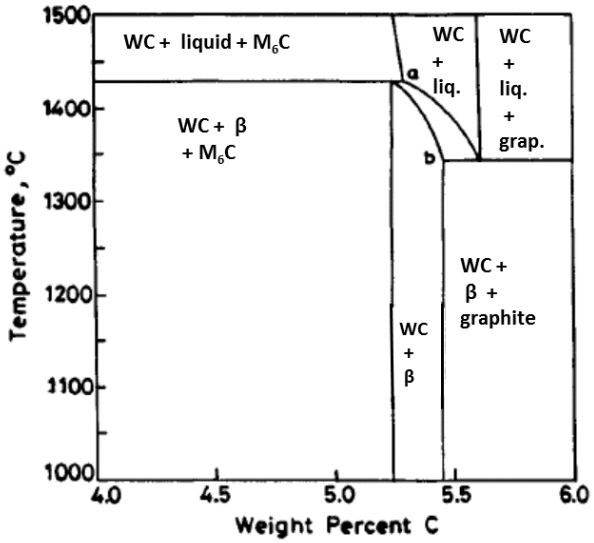

Figure 1.5: Vertical section of the W-Ni-C phase diagram calculated for 10 wt% Ni [4].

1.2.2 Production of cemented carbides

The production of cemented carbides involves the processes of powder consolidation and liquid phase sintering. The powder consolidation process includes milling, drying or granulation, and powder compaction. The selected composition, WC grain size, binder content and additives, of the hardmetal powder are dependent on the application of the sintered material [9]. In general, Co is used as the binder metal and additives such as VC, Cr_2C_3 and TiC are added as grain refiners which improves selected properties of the sintered hardmetal.

1.2.2.1 Powder consolidation

Milling is carried out by conventional ball milling (which is the most common process), attritor milling, or vibratory milling [4, 9]. The objectives of milling, apart from breaking down agglomerates and reducing WC particle size, is to achieve a homogeneous mixture of all the components and ensure that carbide particles are covered with cobalt metal. Organic liquids such as acetone or ethanol are used as a milling liquid to prevent heat generation leading to the oxidation of the carbide particles. Wax or organic lubricants such as poly-ethylene glycol (PEG) is added to the mill charge. This aids in the pressing of green bodies during compaction of the milled powders. Cemented carbide balls are used as milling media, and the powders are milled for 24 to 48 hours, or until the desired grain size is achieved.

The milled powder is granulated [4] using a spray dryer. In the spray drying process, the carbide slurry is sprayed into a stream of preheated inert gas (nitrogen) which is dried at the same time at temperatures between 170 °C to 210 °C. The granules obtained using this process are spherical, and uniform in size, making it easier and more economical for compaction.

The granulated powders [9] are then compacted into shapes using uniaxial pressing, cold isostatic pressing (CIP), extrusion and injection moulding. The green compacts should have sufficient green strength to allow handling and even machining of the components. Typical compaction pressures of 21 to 42 kg/mm^2 are used for pressing green compacts [4].

1.2.2.2 Liquid phase sintering

The process of sintering cemented carbides [4] is known as liquid phase sintering, although 50% of the densification takes place below the melting temperature in a process known as solid state sintering. The stages of sintering are [4, 9]; i) solid state sintering, ii) initial flow stage in which particle rearrangement takes place, iii) solution-reprecipitation stage, and iv) final coalescence in which full densification occurs. The different sintering stages are shown schematically in Figure 1.6. During

the initial stage of heating (< 400 °C), the organic lubricant PEG is decomposed into gaseous species such as CO, CO_2, H_2O and CH_4. As the pores are still open, the gases are allowed to escape however, some carbon is lost in this process.

At 800 °C [9] shrinkage of the compact takes place, and at about 1000 °C, the Co metal starts diffusing on to the WC surfaces. Solid state sintering of the WC grains (WC-WC bonding) takes place at around 1250 °C where the capillary forces of the wetting liquid pulls the WC grains together. This rearrangement in the structure increases the densification process.

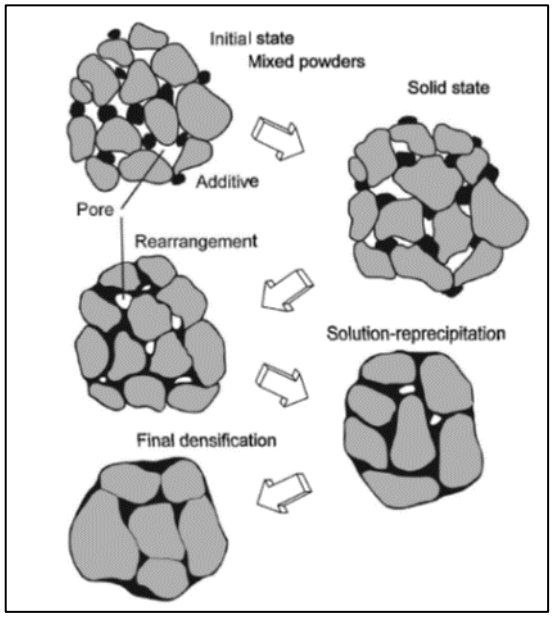

Figure 1.6: Schematic showing the structural changes that occur during different stages of liquid phase sintering [9], which include i) solid state sintering, ii) particle rearrangement, iii) solution-reprecipitation, and iv) final coalescence and densification.

At the next sintering stage, the surfaces of the WC grains are dissolved by fresh liquid and there is a net transport from smaller grains to larger grains. Over time the larger grains grow at the expense of the smaller grains in the process known as solution-reprecipitation. When the liquid reaches saturation, sinter bonds develop between solid grains giving the compact a rigid skeletal structure with liquid dispersed between the spaces. Further densification occurs slowly during the final

sintering stage and external gas pressure is used to close any residual pores. This process is known as hot isostatic pressing (HIP).

1.2.3 Properties of cemented carbides

The physical properties of cemented carbides are determined by the binder content (wt% Co), WC grain size and binder chemistry. These parameters are influenced by the carbon content and additives (VC, Cr_3C_2, TiC). The basic mechanical properties include hardness, fracture toughness, strength and elastic moduli. Magnetic properties such as magnetic saturation and coercivity are used mainly as process control parameters. These measurements [13] are quick, simple and sensitive to small chemical and microstructural changes in the sintered compact.

1.2.3.1 Magnetic properties

Magnetic saturation measurements provide information on the binder chemistry, and composition of the ferromagnetic Co. The carbon level in the sintered compact can be estimated by magnetic saturation measurements. The technique is used to determine whether the material is within the two-phase field (stoichiometric composition) after liquid phase sintering [13]. It is very sensitive to changes in the carbon level of the sintered compact, when there is a carbon deficiency (η-phase) or carbon enrichment (free carbon) as shown in Figure 1.7.

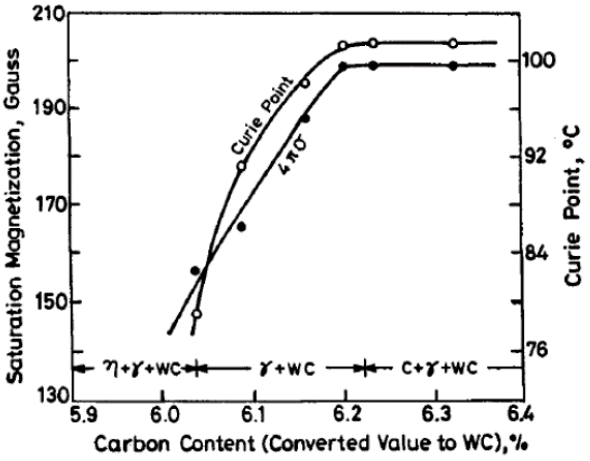

Figure 1.7: Effect of carbon content on magnetic saturation and Curie point [4].

For materials within the stoichiometric range, increasing or decreasing tungsten in solid solution with the cobalt binder is indicated by magnetic saturation values. The magnetic saturation for pure Co is 202 $\mu Tm^3/kg$ [12], and decreases to 150 – 155 $\mu Tm^3/kg$ when the level of tungsten in solution is 15%. This effect is much greater in Ni binders where a decrease in magnetic saturation from 68 $\mu Tm^3/kg$ to 20 $\mu Tm^3/kg$ is observed for 16% W in solution for WC-10Ni. A list of magnetic saturation (σ_s) values for some ferromagnetic metals and compounds taken from the Sigmameter instrumentation manual [14] are given in Table 1.1.

Table 1.1: Magnetic saturation values for selected metals and compounds [14].

Material	Magnetic saturation (σ_s) $G.cm^3/g$	Magnetic saturation (σ_s) $T.m^3/kg$
Nickel	54.5	68.5×10^{-6}
Cobalt	160	201×10^{-6}
α-Fe	217	275×10^{-6}
α-Fe_3C	132	166×10^{-6}
γ-Fe_2O_3	80	100.5×10^{-6}
Fe_3O_4	92	115.5×10^{-6}
1 $G.cm^3/g = 4\pi \times 10^{-7}$ $T.m^3/kg$		

Coercivity measurements are structure sensitive and information on the degree of sintering, cobalt distribution, WC grain size and internal stress component of the sintered hardmetal can be obtained [4]. Excess carbon and higher sintering temperatures leads to WC grain growth and hence a decrease in the coercivity values of the material.

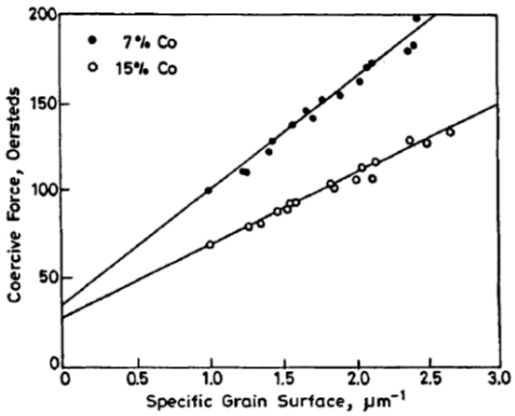

Figure 1.8: Effect of grain size on coercive force for cemented carbides containing 7 and 15 wt% cobalt [4].

The addition of additives (VC, Cr_3C_2) which act as grain growth inhibitors increase the coercivity values. The relationship between coercivity and WC grain size is shown in Figure 1.8 for different cobalt grades.

1.2.3.2 Mechanical properties

The combination of the hard, brittle WC particles [15] together with the soft, ductile metal binder matrix gives cemented carbide its unique mechanical properties. The high hardness and strength of the covalent carbide (WC) coupled with the toughness and plasticity of the metal binder (Co, Ni, Fe) make them outstanding as tool materials in the manufacturing industry. The metal cutting industry accounts for 67% of their total use, followed by mining (13%), wood and plastics (11%) and construction (9%). Generally, a decrease in WC grain size results in an increase in hardness, compressive and bending strength, but reduces impact strength, rupture strength and fracture toughness. As the cobalt content is increased, the hardness, modulus of elasticity, and compressive strength properties are reduced, however, the bending strength and fracture toughness are increased.

The hardness of WC-Co alloys [4] depend mainly on the average grain size and cobalt content. The effect of WC grain size and cobalt content on the hardness property is shown in Figure 1.9.

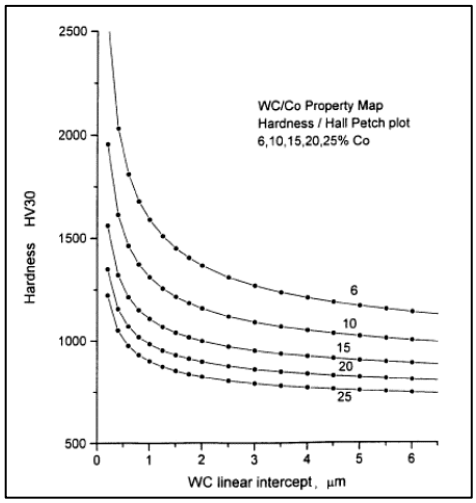

Figure 1.9: Effect of WC grain size and cobalt binder content on the hardness property [13].

A property map showing the effect of cobalt content on hardness, compressive strength and transverse rupture strength (TRS) for a given WC grain size (2 µm) is shown in Figure 1.10.

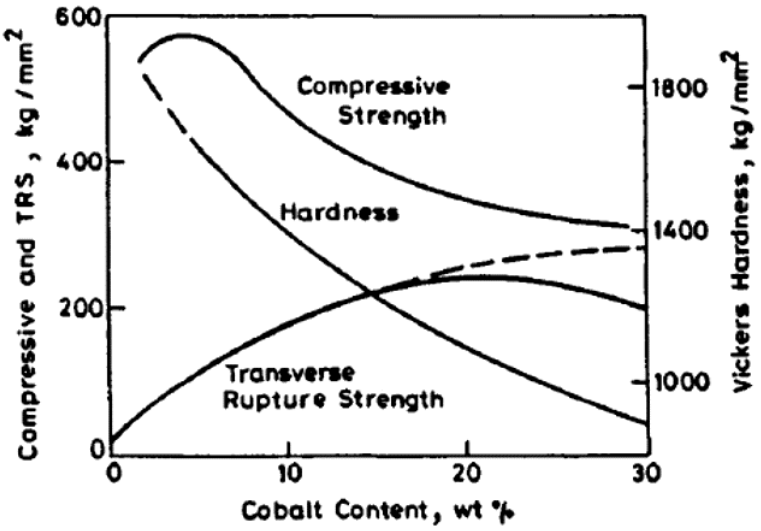

Figure 1.10: Effect of cobalt content on hardness, compressive strength and TRS for 2 µm grain size WC-Co hardmetals [4].

In general, there is an inverse relationship between hardness and fracture toughness as shown in Figure 1.11. In WC-Co alloys [4], the fracture toughness (K_{IC}) increases

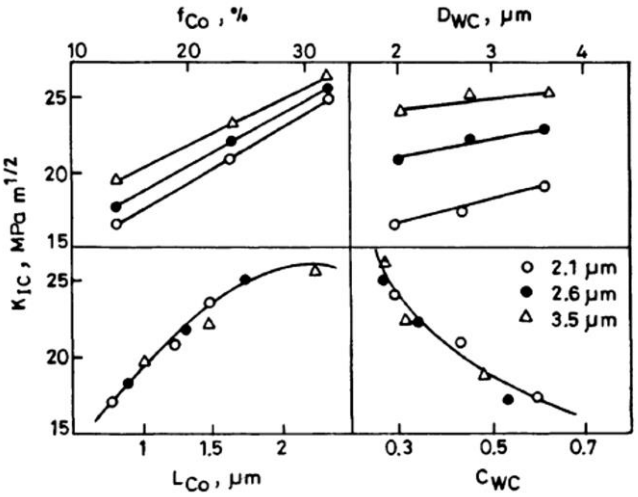

Figure 1.11: Fracture toughness as a function of Co volume fraction and microstructural parameters for WC-Co alloys with different WC grain sizes [4].

as the cobalt volume fraction, WC grain size and Co mean free path are increased, while an increase in carbide contiguity causes a decrease in K_{IC}.

Cobalt is the main binder for conventional cemented carbides [1], and is widely used for most applications. However, cobalt has poor hot hardness and oxidation/corrosion resistance [16]. Therefore, in certain applications such as the chemical and food industry, Fe and Ni binders are used. Early studies [17] indicated that Fe and Ni binders have inferior mechanical properties compared to Co. The difficulty in controlling the carbon balance in Fe binders resulted in the formation of the unwanted η-phase or free graphite [12], thereby causing a reduction in the mechanical properties (hardness, toughness and strength). One of the reasons for the reduced mechanical strength of Ni binders [6] is the higher stacking fault energy which makes work hardening only moderate. Also, Ni binders are sintered at higher temperatures making them prone to WC grain growth which causes a reduction of strength and hardness properties. Improvements in the processing and sintering technologies as well as the addition of grain refiners such as VC and TiC, have shown matching or exceeding mechanical properties [6, 8].

Chang *et al*. [17] compared the properties of WC-FeNi alloys to WC-Co for different sintering temperatures, and showed that the optimum mechanical properties were obtained at 1400 °C for WC-FeNi alloy and 1350 °C for WC-Co. The mechanical properties for the WC-15FeNi alloy are given as 85.3 HRA (920 HV) for hardness, 2524.5 MPa for rupture strength and 15.1 $MPa.m^{½}$ for toughness, whilst the WC-15Co alloy returned values of 84.4 HRA (860 HV), 2471.2 MPa (TRS) and 10.2 $MPa.m^{½}$ (K_{IC}). The WC-FeNi alloy showed a significant improvement in mechanical properties compared to WC-Co. However, Uhrenius *et al*. [10] reported that the hardness value of 20 wt% FeNi binder (890 HV) was 100 – 150 HV lower than that of WC-20Co (1030 HV). The study of the mechanical properties of WC-10FeNi by Gonzalez *et al*. [18] reported hardness values of 1603 HV and 1200 HV for grain sizes of 1 and 6 µm grades, respectively similar to WC-10Co grades. The fracture toughness of the WC-10FeNi alloy showed a slight increase after heat treatment without sacrificing the hardness property.

Shon *et al*. [19] showed that Fe binders have a higher hardness compared to Co and Ni binders. Hardness values of 1814 HV, 1776 HV and 1750 HV were reported for WC-10Fe, WC-10Co and WC-10Ni, respectively, with a grain size of 0.5 µm. Studies by Hanyaloglu *et al*. [1] on cemented carbides containing Fe-13.5Mn binders revealed that the Fe-Mn binders have improved hardness and toughness compared to Co binders. These results are summarised in Table 1.2.

Table 1.2: Fracture toughness and hardness values for WC-Co and WC-FeMn hardmetals determined by Hanyaloglu *et al*. [1].

Binder wt%	Niihara K_{IC} MPa.m^{½}	HV GN.m^{-2}
15Co	7 - 8	11
25Co	14 - 17	8
15FeMn	15	15
25FeMn	20	14

1.2.4 Mössbauer spectroscopy

In 1957, Rudolph Mössbauer discovered the recoilless gamma (γ) ray emission and absorption by atomic nuclei in solids, now known as the Mössbauer effect. This effect is crucial to the success of the technique referred to as Mössbauer spectroscopy [20].

Mössbauer spectroscopy [20] can be applied to many areas of science including Physics, Chemistry, Biology and Metallurgy. The technique is able to provide information about the chemical, structural, magnetic and time-dependent properties of a material. The most common Mössbauer isotope is ^{57}Fe, and resonance only occurs when the transition energy of the emitting and absorbing nucleus are an exact match. Thus the application of the technique may be suitable for hardmetals with Fe or Fe alloy binders. The electronic, structural and magnetic properties of the binder alloys can be measured using Mössbauer spectroscopy to obtain information on the Fe charge states, Fe phases and the hyperfine interaction parameters.

During the drilling process of iron and other ores, the common wear process of WC-Co tools are abrasion and cracking due to impacts and thermal fatigue. Banganayi and Mulaba-Bafubiandi *et al*. [21, 22] used X-ray diffraction (XRD) and Mössbauer spectroscopy to examine the role of Fe oxidation on WC-Co drill bit inserts. In their investigations, powders were produced using high energy ball milling of hematite (α-Fe_2O_3) ore with Co, WC and WC-Co powders. After 15 hrs of milling α-Fe_2O_3 with WC (50:50), the Mössbauer spectra were fitted with the following spectral components: (a) a magnetic sextet with a magnetic hyperfine field (B_{hf}) of 51.4 T, an isomer shift (δ) of 0.37 mm/s and quadrupole splitting (ΔE_Q) of -0.17 mm/s, and (b) a paramagnetic doublet with δ = 0.39 mm/s and ΔE_Q = 0.46 mm/s. The sextet component was assigned as bulk crystalline α-Fe_2O_3 which was mostly unaffected by the milling process. The central doublet was attributed to the smaller (superparamagnetic) particles ≈10 nm. The observed distribution of magnetic fields and/or doublet was ascribed to amorphous iron oxide phases which were not detected by XRD.

Wang *et al*. [23] synthesised WC powders by high energy ball milling tungsten and activated carbon powders (50:50 ratio). The powders with anticipated Fe contamination from extended milling was analysed using ^{57}Fe Mössbauer spectroscopy. The WC phase was detected using XRD only after 170 hrs of milling and after 310 hrs, the material comprised predominantly of WC. The Mössbauer spectrum for this material was fitted with a single line with $\delta = -0.16$ mm/s, and two sextets with magnetic hyperfine fields of 33 T and 20.5 T, respectively. The single line component was assigned to Fe_3W_3C (η-phase) and the two sextets to α-Fe and Fe_3C, respectively.

Mercado *et al*. [24] also used high energy ball milling to produce Fe_6W_6C by milling Fe, W and C powders. After 30 h of milling two paramagnetic phases were detected in the Mössbauer spectrum corresponding to Fe_3W_3C and Fe_6W_6C. The paramagnetic phases were fitted with two doublets (D1 and D2) with δ = 0.169 mm/s and ΔE_Q = 0.594 mm/s for D1, and $\delta = -0.079$ mm/s and ΔE_Q = 0.342 mm/s for D2. In addition, a magnetic component with a hyperfine field of 37.7 T was fitted and was tentatively assigned to a tungsten iron oxide phase.

Sufianu [25] and Ibwanga [26] evaluated WC-20Fe10Co and WC-20Fe10Co6TiC alloys, respectively using Mössbauer spectroscopy for their MSc Dissertations at the University of the Witwatersrand in 2016. The Mössbauer spectrum for the WC-20Fe10Co alloy [25] was fitted with two sextets with magnetic hyperfine fields of 33.6 and 35.1 T, respectively. These fields were correlated to a Fe-rich cobalt phase and a $Fe_{50}Co_{50}$ phase, respectively. Two sextets, a doublet and a singlet [26] gave satisfactory fits for the WC-20Fe10Co6TiC spectrum. The hyperfine fields for the two sextets were 37.2 and 35.6 T, respectively and was assigned to two different phases of FeCo. The doublet with hyperfine parameters of δ = 0.28 mm/s and ΔE_Q = 0.54 mm/s was attributed to a FeWC phase, and the single line with δ = 0.026 mm/s corresponded to a TiFe phase.

1.3 Motivation

There is a need in the cemented carbide industry to find an alternative binder to replace Co in WC-Co alloys. This is due to the toxicity of Co, and huge price fluctuations and availability of Co [5, 6]. Fe and Ni binders have been identified as suitable replacements [6] for Co, however, it is difficult to control the carbon levels in Fe and Ni based binders. Therefore, more research work is required on alloy design and quality control for Fe binder systems. The control of carbon in the fabrication process is critical to the binder phase composition and WC grain size control, which affect the properties of the sintered material.

The properties of metals and alloys are determined by their fabrication process, and post fabrication treatments such as heat treatment, cooling rates (fast or slow), alloying, mechanical deformation and ageing [27]. All these factors could influence the arrangement of atoms and thus their interaction properties, and hence would influence the electrical or heat conductivity, magnetism, elasticity, density and reactivity of the material under study. Mössbauer spectroscopy is a useful tool for investigating metals and alloys since the technique is sensitive to changes in electron density, electric field gradient and magnetic field. The technique is also

sensitive to changes of the mean square displacement (Debye-Waller factors) of the Mössbauer isotope.

The metallic binder systems being investigated in this study are Fe-based, making it suitable for ^{57}Fe Mössbauer spectroscopy investigations. There are limited Mössbauer studies on milled WC, Fe and Co powders [21, 22]. Literature searches do not show any published studies on sintered WC hardmetals. To our knowledge, only recently have Mössbauer investigations been carried out at the University of the Witwatersrand on sintered hardmetals [25, 26] containing 20Fe10Co and 20Fe10Co6TiC binders. The current investigations expands the scope of Mössbauer spectroscopy to other Fe-based binder systems.

1.4 Aim and objectives of this study

The purpose of this study is to ascertain whether more information on the arrangement of atoms and their interaction properties in WC-Fe, WC-Fe/Ni and WC-Fe/Mn cemented carbides can be obtained by employing Mössbauer Spectroscopy. This will provide a better understanding of the structural, electrical and magnetic properties of the materials under study. The objectives of the project are:

- To assess the microstructures of Fe and Fe alloy binders and identify the phases present using Optical microscopy (OM), scanning electron microscopy (SEM) and energy dispersive spectrometry (EDS).
- To determine the phases present in the milled powders and sintered materials components using XRD analysis.
- To measure the density, magnetic properties and hardness of the materials.
- To investigate the Fe charge states, Fe phases and hyperfine interactions using Mössbauer Spectroscopy on the milled powders and sintered structures.
- To understand the formation Fe complexes.

1.5 Dissertation outline

The current chapter provides the background and comprehensive literature review on conventional (Co binders) and new grades (alternate binders) of cemented carbides, and also relevant Mössbauer investigations. Chapter 2 describes the basic principles of X-ray diffraction, magnetism and the Mössbauer effect, including an overview of hyperfine interactions. The experimental details are outlined in Chapter 3 which includes powder preparation (milling), consolidation, and sintering of the materials. The analysis techniques used to evaluate the sintered components are also described. These include density measurements, magnetic property (magnetic saturation and coercivity), hardness measurements, microstructural assessment, X-ray diffraction and Mössbauer spectroscopy. Data analysis and interpretation of results are presented and discussed in Chapter 4. A summary of the project, including recommendations for further study ends the dissertation in Chapter 5.

Chapter 2

Principles of X-Ray Diffraction and the Mössbauer Effect

2.1 Introduction

Powder X-ray diffraction and Mössbauer spectroscopy are the principle tools of analysis used in this work. This chapter describes the basic principles of these techniques. A brief introduction to powder X-ray diffraction covering the unit cell, crystal lattices, Miller indices and the Bragg equation will be presented. The basic principles of magnetism are discussed, which include the different types of magnetism. The Mössbauer effect will be reviewed, including the theory of gamma ray emission and absorption, and hyperfine interactions. These hyperfine interactions include the electric monopole interaction, electric quadrupole interaction and magnetic dipole interaction.

2.2 Theory of Powder X-ray Diffraction

Powder X-ray diffraction [28] is widely used for phase analysis and for solving the crystal structures in solid state materials. In addition, this technique is also employed for evaluating structural imperfections, and accurately measuring unit cell dimensions. The arrangement of atoms in crystal structures is the basis for understanding materials.

2.2.1 The Unit Cell and Crystal Lattice

Crystalline materials [29] are characterised by their chemical composition and the regular arrangement of atoms in three dimensions. A unit cell is the smallest unit that contains the structural and chemical information that uniquely defines the material [30]. The atoms in a crystal [31] can be mathematically represented as points in a three dimensional real space lattice. When the points are assembled in a periodic fashion then real space base vectors **a**, **b** and **c**, and the angles α, β and γ can be defined as shown in Figure 2.1. The distance between the two nearest neighbour atoms in the *x*, *y* and *z* axes are represented by the vectors **a**, **b** and **c**.

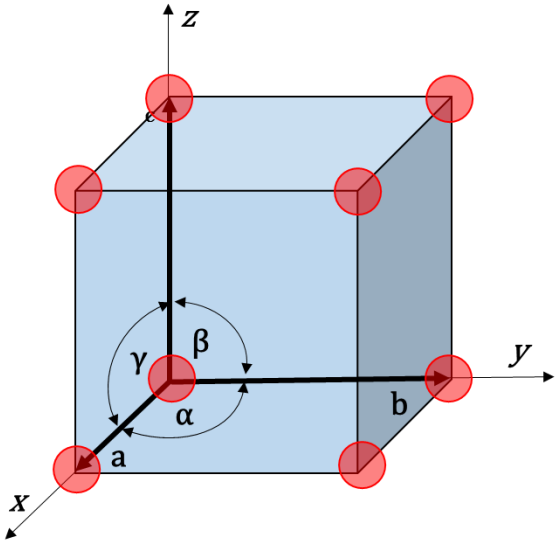

Figure 2.1: Unit cell in a simple cubic lattice with atoms at each corner [31].

In crystallography [30] there are 6 crystal families, 7 crystal systems, 5 centering positions, 14 Bravais lattices and 32 crystal classes. The unit cell can be divided into 6 families based on the angles and length of the axes sides. The 6 crystal families are cubic, hexagonal, tetragonal, orthorhombic, monoclinic and triclinic. The hexagonal family can also appear as trigonal, and thus is divided into two systems giving 7 crystal systems for the 6 families. A crystal system can only have 5 rotation axes; 1-fold, 2-fold, 3-fold, 4-fold and 6-fold which allows unit cells to grow uniformly without any opening between them. This crystallographic restriction results in 32 classes or point groups classified by symmetric operations, which are rotation, reflection and inversion. The combination of lattice type and crystal system is known as the Bravais lattice. The cubic system [31] for example has three Bravais-lattice types which are face centred cubic (FCC), body centred cubic (BCC) and the primitive or simple cubic system.

2.2.2 Crystal Planes and Direction

A lattice plane [31] is defined by passing through three non-collinear lattice points. The vector that is perpendicular to the plane gives the orientation of a plane. If two

vectors $\boldsymbol{r}_1$ and $\boldsymbol{r}_2$ connects two lattice points as shown in Figure 2.2a, the cross product of the vectors is given as

$$\boldsymbol{r}_1 \times \boldsymbol{r}_2 = xyz\left[\frac{\mathbf{b}\times\mathbf{c}}{x} + \frac{\mathbf{c}\times\mathbf{a}}{y} + \frac{\mathbf{a}\times\mathbf{b}}{z}\right]. \quad (2.1)$$

A general shorthand notation [u v w] is used to specify a translation direction in a lattice [32]. In a cubic lattice [31] where $\boldsymbol{r}_1$ = u**a** and $\boldsymbol{r}_2$ = v**b**, represents a plane consisting of $\boldsymbol{r}_1$ and $\boldsymbol{r}_2$ is in the *xy*-plane (Figure 2.2b). The direction of the plane is

$$\boldsymbol{r}_1 \times \boldsymbol{r}_2 = \mathrm{u}\mathbf{a} \times \mathrm{v}\mathbf{b} = \mathrm{uv}\mathbf{c} \quad (2.2)$$

along the *z*-direction and is enclosed in a square bracket [uvw].

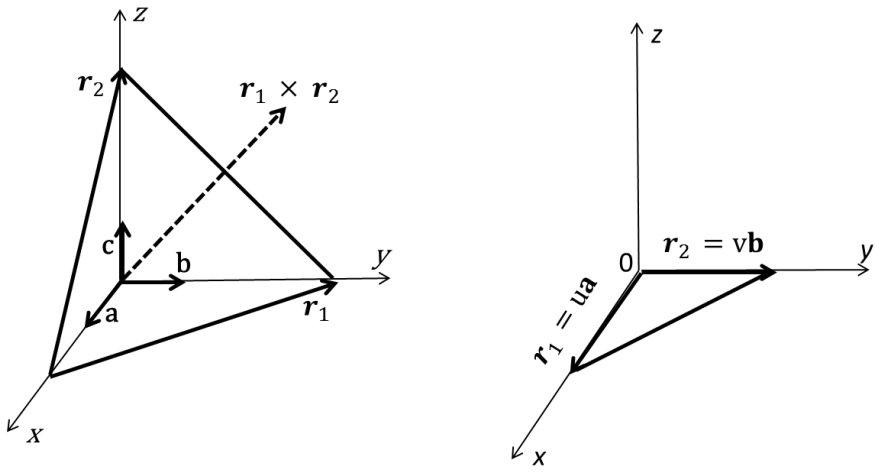

Figure 2.2: (a) Diagram showing the cross product of two vectors r_1 and r_2 in a plane. (b) Example of a xy-plane with its direction along the z-direction.

The Miller indices *hkl* specify the direction of the plane. The direction is obtained by three intercepts on the *x*, *y* and *z*-axes in terms of the lattice constants **a**, **b** and **c** (**a**/*x*, **b**/*y* and **c**/*z*). The reciprocals of these three numbers are reduced to the smallest integer by multiplying by a common factor "n" to give (*hkl*). When a plane

intercepts the *x*, *y* and *z*-axes at 1, 1 and ∞, the reciprocals are 1, 1 and 0, respectively. Hence the Miller indices are (110) as shown in Figure 2.3.

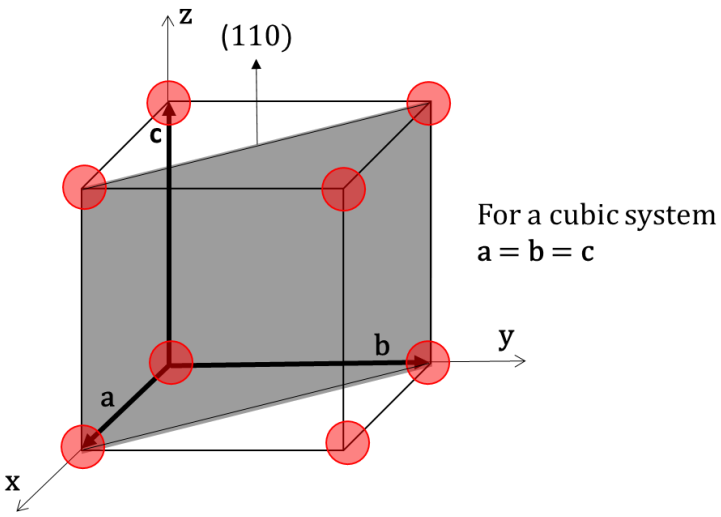

Figure 2.3: Schematic diagram showing the (110) plane in a cubic lattice.

Lattice planes [33] are defined by their orientation in a crystal and their interplanar distance or *d*-spacing. In a cubic system where **a** = **b** = **c**, the interplanar distance is

$$\frac{1}{d_{hkl}^2} = \frac{h^2 + k^2 + l^2}{\mathbf{a}^2} \tag{2.3}$$

therefore,

$$d_{hkl} = \frac{\mathbf{a}}{\sqrt{h^2 + k^2 + l^2}}. \tag{2.4}$$

A typical X-ray diffraction pattern [34] from a material usually contains many distinct peaks, with each peak matching a different interplanar spacing, *d*.

2.2.3 Bragg's Law

The Bragg equation [35] is the easiest access to structural information in powder diffraction. X-ray diffraction can be described by the Bragg equation as a reflection of X-rays by a set of lattice planes with the same indices that are equally spaced, and separated by the distance, d_{hkl}. When an incident beam of X-rays is reflected by different planes, the beam reflected by the lower plane travels an extra distance than that reflected by the upper plane as shown in Figure 2.4.

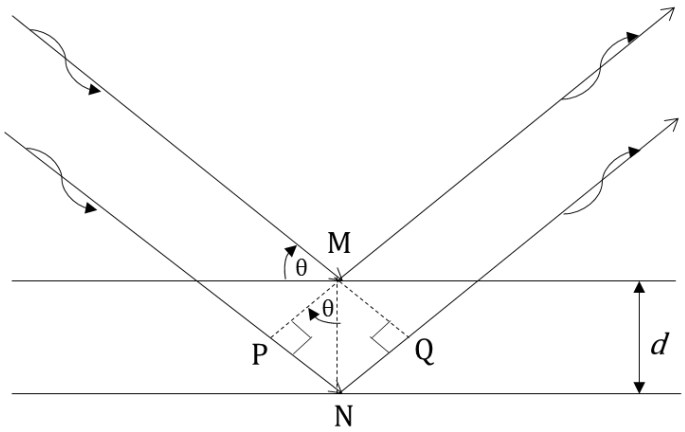

Figure 2.4: Geometric illustration used for the derivation of Bragg's law.

In Figure 2.4, the beam reflected by the lower plane must travel the extra distance PN + NQ for the two beams to continue travelling adjacent and parallel. The extra distance is

$$\Delta = \mathrm{PN} + \mathrm{NQ} = 2\mathrm{PN} \tag{2.5}$$

where Δ is the path difference.

In triangle MPN,

$$\mathrm{PN} = d \sin\theta. \tag{2.6}$$

The path difference is

$$\Delta = 2d \sin\theta \tag{2.7}$$

where d is the interplanar distance, and 2θ is the diffraction angle. If the two planes are to scatter in phase, then Δ must equal an integral number of wavelengths, $n\lambda$. Thus giving the Bragg equation

$$n\lambda = 2d \sin\theta \quad (2.8)$$

where n is an integral number (0, 1, 2, 3….) and λ is the wavelength. The d-spacing can be determined from the Bragg angle which allows for the calculation of the lattice parameters **a**, **b** and **c** which contain vital structural information. Also, unknown structures can be resolved in powder diffraction using the d-spacings.

2.3 Types of magnetism

An atom contains a nucleus in its centre with negatively charged electrons orbiting the nucleus, which consists of positively charged protons and neutrons which have no charge [36]. A magnetic field is produced by electrons orbiting the nucleus, and the direction of the magnetic field is determined by the direction of the electron spin and orbit. The strength of the magnetic field is called the magnetic moment. When two electrons are spinning and orbiting the nucleus in opposite directions, the magnetic field strength is zero as the opposite spins of the electrons cancel their magnetic fields. If an atom has a higher number of electrons spinning in a clockwise compared to a lower number of electrons spinning in an anti-clockwise direction, then the atom has some magnetic field strength. Electrons that occupy the same orbital of an atom with orbit and spin in opposite directions are known as paired electrons. A single electron that occupies an orbital is called an unpaired electron. The general types of magnetism obtained are diamagnetism, paramagnetism, ferromagnetism and anti-ferromagnetism.

2.3.1 Diamagnetism

Materials that are weakly repelled to a magnet or an external magnetic field are known as diamagnetic materials [36]. These materials have all paired electrons, and thus have no net magnetic moment or magnetic field strength. When diamagnetic materials are placed in an external magnetic field, the magnetic moment inside the

diamagnetic material is less than the magnetic moment in the air surrounding the material. Superconductors are considered as diamagnetic materials as they exhibit both perfect conductivity and perfect diamagnetism at low temperatures.

2.3.2 Paramagnetism

Materials that are slightly attracted to a magnet are called paramagnetic materials. These materials are weakly magnetised when they placed in the presence of a strong external magnetic field [36]. There are more unpaired electrons in paramagnetic materials. In pure paramagnetic materials, the magnetic moment or magnetic field strength of the electrons do not interact with each other, and are randomly aligned in the absence of a strong external magnetic field as show in Figure 2.5. The resultant net magnetic field is zero. When a strong external magnetic field is applied, the magnetic moment of the electrons are aligned in the direction of the magnetic field, and hence the direction of the magnetic field strength is in the direction of the applied external magnetic field. Paramagnetic materials lose their magnetism when the strong external magnetic field is removed.

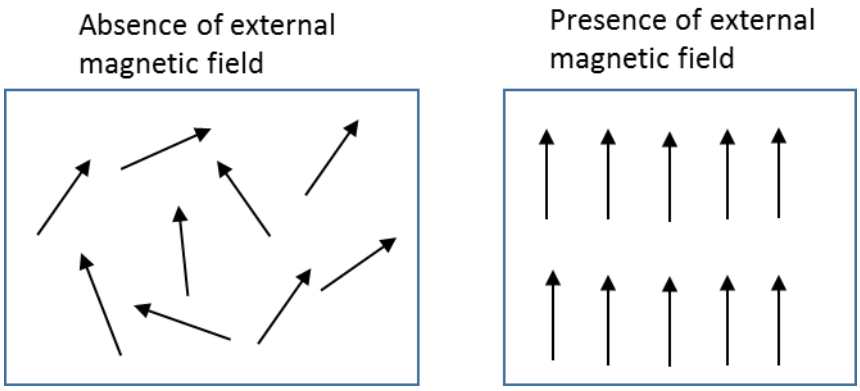

Figure 2.5: The magnetic moments of electrons in the absence of an external magnetic field (randomly aligned), and in the presence of a strong external magnetic field [36].

2.3.3 Ferromagnetism

Ferromagnetic materials are strongly magnetised when placed in a strong external magnetic field. These materials continue to hold magnetism even in the absence of

a strong external magnetic field [36]. Individual atoms of a ferromagnetic material exhibits permanent magnetic moments or magnetic field strength of its own due to unpaired electrons. The magnetic moments interact with each other in a way that the magnetic moments of a group of atoms align themselves in one particular direction, referred to as a magnetic domain, as shown in Figure 2.6.

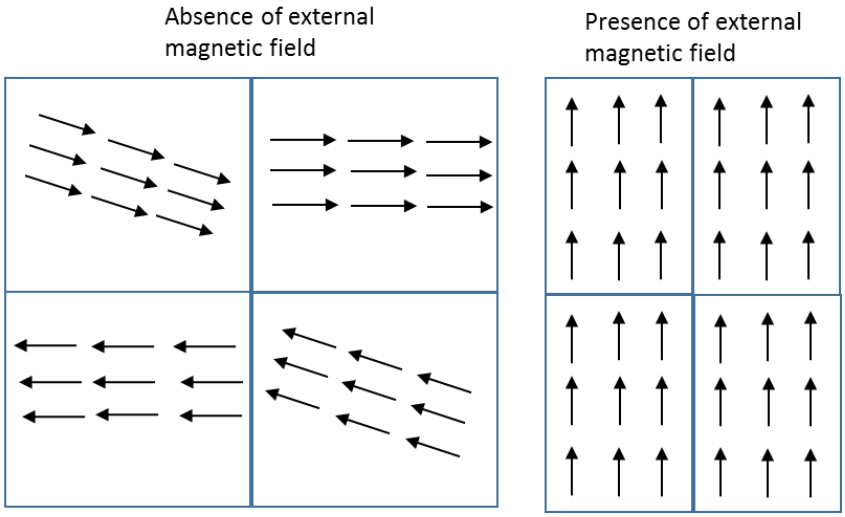

Figure 2.6: Magnetic domains for a ferromagnetic material in the absence and presence of a strong external magnetic field [36].

2.3.4 Anti-ferromagnetism

In anti-ferromagnetic materials, the magnetic moments of the neighbouring electrons point in opposite directions [36]. Therefore, the net magnetic moment is zero. The alignment of the magnetic movement of the atoms are combinations of parallel and anti-parallel, as shown in Figure 2.7.

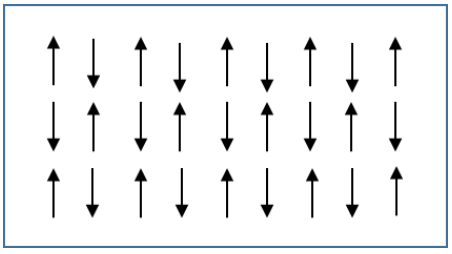

Figure 2.7: The alignment of the magnetic domains in anti-ferromagnetic are both parallel and anti-parallel [36].

2.4 Mössbauer Spectroscopy

Mössbauer spectroscopy is a useful technique which is capable of probing the local environment on an atomic scale. This provides useful information on the lattice sites, symmetry, charge states, magnetic interactions and dynamic processes. The success of the technique [37] stems from the discovery of recoilless emission and absorption of gamma rays between nuclei observed by Rudolph Ludwig Mössbauer in 1957, now commonly referred to as the Mössbauer effect. The 1961 Nobel Prize in Physics was awarded to Rudolph Mössbauer for this discovery where he first observed resonant absorption of 129 keV γ-ray using ^{191}Ir [38].

2.4.1 The Mössbauer Effect

Early attempts to detect resonant emission and absorption of gamma rays did not succeed because of nuclear recoil by the free nucleus. The nucleus recoils due to the conservation of momentum [20], similar to the recoil action of a gun when firing a bullet. The recoil of a free nucleus having a recoil energy of E_R is shown in Figure 2.8.

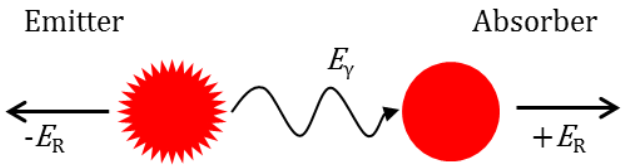

Figure 2.8: Recoil of free nuclei during emission or absorption of a γ-ray.

The nucleus of mass M [27] moves with velocity $\vec{v}$ in an opposite direction of the γ-ray emission and takes up kinetic recoil energy

$$E_R = \frac{1}{2} M v^2 \ . \qquad (2.9)$$

Due to the conservation of momentum,

$$p_{\mathrm{n}} = -p_{\gamma} = \frac{-E_{\gamma}}{c} \tag{2.10}$$

where p_{n} is the momentum of the nucleus, p_{γ} is the momentum of the γ-ray and c is the velocity of light. The energy of the γ-ray is

$$E_{\gamma} = E_0 - E_{\mathrm{R}}. \tag{2.11}$$

As the nucleus has a large mass, the recoil energy may be written in a nonrelativistic approximation as

$$E_{\mathrm{R}} = \frac{p_{\mathrm{n}}^2}{2M} = \frac{E_{\gamma}^2}{2Mc^2}. \tag{2.12}$$

Should emission occur when the nucleus is moving at velocity v_{n}, as atoms in a gas are never at rest, the γ-photon of energy E_{γ} receives a Doppler energy E_{D} where

$$E_{\mathrm{D}} = \frac{v_{\mathrm{n}}}{\mathrm{c}} E_{\gamma}. \tag{2.13}$$

This Equation is added to E_{γ}

$$E_{\gamma} = E_0 - E_{\mathrm{R}} + E_{\mathrm{D}}. \tag{2.14}$$

The Doppler broadening of the transition line $\overline{E_{\mathrm{D}}}$ can be calculated from

$$\overline{E_{\mathrm{D}}} = E_{\gamma} \overline{(2E_{\mathrm{K}}/Mc^2)}^{1/2} \tag{2.15}$$

where E_{K} is the mean kinetic energy of all moving nuclei. $\overline{E_{\mathrm{D}}}$ is taken over all angles ϑ between $\overrightarrow{p_{\gamma}}$ and $\overrightarrow{v_{\mathrm{n}}}$. The Doppler broadening of the emission and absorption lines overlap in a small energy region due to the low probability of resonance.

Rudolph Mössbauer discovered that when atoms are bound in a solid matrix of mass M_a [39], the effective mass of the nucleus bound in a solid is much greater than the mass of a free nucleus. Thus, the loss in energy due to recoil becomes infinitesimally small, resulting in the possibility of *recoil free emission* and subsequent absorption by a similar nucleus (same number of protons (Z) and neutrons (N)) in its ground state whereby transitions to the excited state E_e occurs. This process is referred to as nuclear resonant absorption of γ-rays as depicted in Figure 2.9.

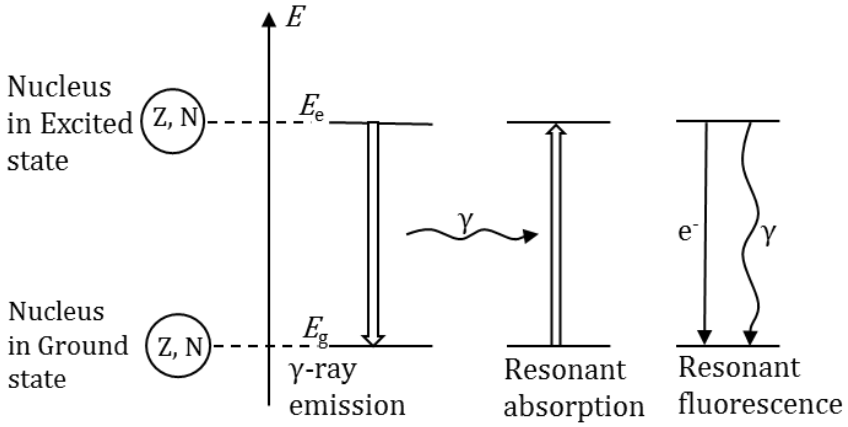

Figure 2.9: Representation of nuclear resonance absorption of γ-rays and nuclear resonance fluorescence.

2.4.2 Recoil Free Fraction

In a solid matrix, nearly all of the recoil energy E_R [27, 40] is transferred to the lattice vibrational system which dissipates by heating the lattice surroundings. There is a certain probability factor *f* that no lattice excitation takes place during emission or absorption, known as the zero-phonon process. The recoil-free fraction *f* represents the fraction of nuclear transitions without recoil and is given as

$$f = 1 - k^2 \langle x^2 \rangle \tag{2.16}$$

where $\langle x^2 \rangle$ is the mean-square displacement of the nucleus in the *x*-direction and *k* is the propagation vector. Since $k^2 \langle x^2 \rangle \ll 1$,

$$f = \exp(-k^2 \langle x^2 \rangle). \tag{2.17}$$

The recoil-free fraction can further be calculated in the Debye solid model as

$$f(T) = \exp\left[\frac{-6E_{\mathrm{R}}}{k_{\mathrm{B}}\Theta_{\mathrm{D}}}\left\{\frac{1}{4}+\left(\frac{T}{\Theta_{\mathrm{D}}}\right)^{2}\int_{0}^{\Theta_{\mathrm{D}}/T}\frac{x}{\mathrm{e}^{x}-1}\,\mathrm{d}x\right\}\right] \tag{2.18}$$

where k_{B} is the Boltzman constant and Θ_{D} is the Debye temperature, which is a measure of bonds between atoms. In this case, $f\,(T)$ is generally known as the Debye-Waller factor, or the Lamb-Mössbauer factor, and equation (2.18) can be further reduced to

$$f(T) = \exp\left[-\frac{E_{\mathrm{R}}}{k_{\mathrm{B}}\Theta_{\mathrm{D}}}\left(\frac{3}{2}+\frac{\pi^{2}T^{2}}{\Theta_{\mathrm{D}}^{2}}\right)\right] \text{ for } T \ll \Theta_{\mathrm{D}}\,, \tag{2.19}$$

$$f(\mathrm{T}) = \exp\left(-\frac{6E_{\mathrm{R}}T}{k_{\mathrm{B}}\Theta_{\mathrm{D}}^{2}}\right) \text{ for } T > \Theta_{\mathrm{D}}\,. \tag{2.20}$$

The equations above show that *f* increases with decreasing temperature. This is the reason that Rudolph Mössbauer unexpectedly observed an increase in resonance, while attempting to reduce the resonance effect by decreasing temperature. The Debye-Waller factor *f*, also increases with decreasing recoil energy, and increases with increasing Debye temperature Θ_{D}.

2.4.3 Natural Linewidth and Spectral Lineshape

The energy level of an atom in the excited state, E_{e} having a mean lifetime τ cannot be measured to a precise value due to the wave-particle duality of the nucleus [40]. This energy level spreads over a certain range of width ΔE, and correlates with the measure of uncertainty in time Δt ($\approx \Delta\tau$) which is given by the Heisenberg uncertainty relation

$$\Delta E \Delta t \geq \hbar \tag{2.21}$$

where $\hbar = h/2\pi$, and h is the Planck's constant. The profile of the energy distribution would be observed as a distribution on a graph within a finite range, while the lifetime τ of the ground state has zero uncertainty in energy. All possible energies

within the range of ΔE are involved [27] for nuclear transitions from an excited state (e) to the ground state (g). The transition intensity as a function of the transition energy I (E), produces a spectral line centered on the most probable transition energy E_0 as shown in Figure 2.10. Weisskopf and Wigner [40] have shown that

$$\Gamma\tau = \hbar \tag{2.22}$$

where $\Gamma = \Delta E$ is the full width of the transition spectral line at half maximum. The spectral line has been found to be Lorentzian or Breit-Wigner form [27, 40] which is expressed as

$$\omega(E) = \frac{\Gamma/2\Pi}{\left(E - E_\gamma^0\right) + (\Gamma/2)^2} \tag{2.23}$$

where ω (E) is the probability function, and E_γ^0 is the mean value of the emitted gamma ray.

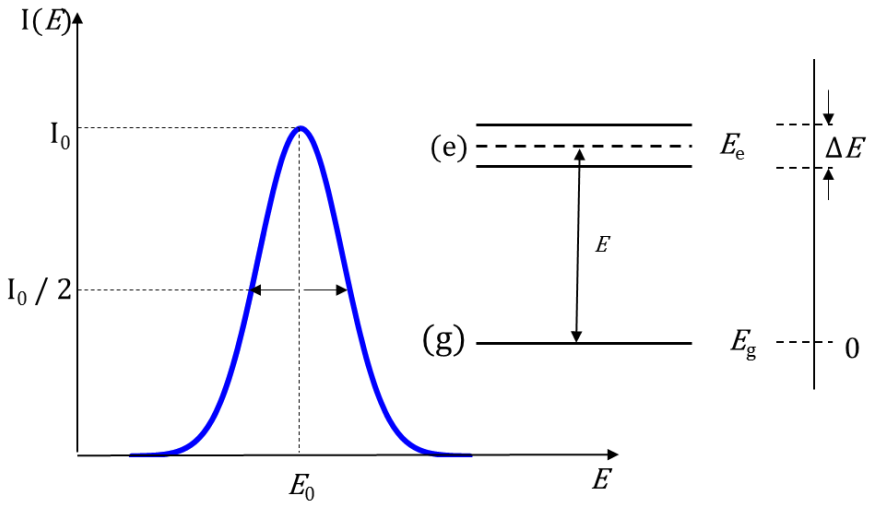

Figure 2.10: Intensity I (E) as a function of the transition energy E.

The mean lifetime τ of the excited state determines the width of the transition line [27]. Lifetimes of excited nuclear states ranging from ~ 10^{-6} s to ~ 10^{-11} s are suitable for Mössbauer Spectroscopy. Too narrow transition lines are obtained for longer lifetimes and the emission and absorption lines would not overlap sufficiently. Very small Doppler velocities of < μm.s^{-1} are necessary for the longer lifetimes. The

transition lines for lifetimes shorter than 10^{-11} s are too broad and the resonance overlap between them will be smeared and no longer be distinguishable from the baseline of the spectrum.

Maximum absorption only takes place when the spectral line for the emission and absorption processes appear at the same energy position, E_0. The resonance absorption cross section is given by another form of the Breit-Wigner formula

$$\sigma(E) = \frac{\sigma_0 \, \Gamma^2}{\Gamma^2 + 4(E - E_0)^2} \tag{2.24}$$

where

$$\sigma_0 = \frac{\lambda^2}{2\pi} \cdot \frac{2I_e + 1}{2I_g + 1} \cdot \frac{1}{\alpha + 1} \tag{2.25}$$

is the maximum absorption cross section, I_e and I_g are the nuclear spin quantum numbers of the excited and ground states, respectively, λ is the wavelength of the γ-ray and α is the internal conversion coefficient which for ^{57}Fe, α = 8.21. After resonant γ-ray absorption, the nucleus remains in the excited state for the mean lifetime τ. The nucleus then undergoes a transition back to the ground state by the emission of a γ-ray or conversion electrons due to internal conversion which is the transfer of energy from the nucleus to the electron shell. This process is known as nuclear resonance fluorescence.

2.4.4 Doppler Shift

A Doppler shift [41] in photon energy occurs when there is relative motion between the emitter and absorber. The energy of a photon is given by the Lorentz transformation

$$E'_\gamma = \frac{1}{\sqrt{1 - \beta^2}} \left(E_\gamma + v p_\gamma \right) = E_\gamma \frac{1 + \beta}{\sqrt{1 + \beta^2}} \tag{2.26}$$

where $\beta = v/c$, c is the speed of light, E_γ is the energy of the emitted photon, p_γ is the momentum, v is the relative velocity between the emitter and absorber and E'_γ is the resulting Doppler shifted photon energy. The change in photon energy due to motion is given by the first order binomial expression, for $\beta \ll 1$ as

$$\Delta E = E'_\gamma - E_\gamma = \beta E_\gamma = \frac{v}{c} E_\gamma \ . \quad (2.27)$$

By varying the relative velocity between the emitter and absorber, a range of photon energies can be scanned. The absorption rate as a function of velocity is measured and can be converted to energy shift.

2.5 Hyperfine Interactions

A nucleus interacts with its surrounding environment [40] through electric and magnetic fields which perturb the nuclear energy levels. These interactions [20, 42] are minute and are in the order of $10^{-7} – 10^{-8}$ eV, in comparison to the energy levels of the nucleus. The limiting resolution is the natural linewidth which is the average lifetime of the excited state before it decays by emitting a gamma-ray. The most common Mössbauer isotope, ^{57}Fe, has a linewidth of $\approx 5\times10^{-9}$ eV and an energy ratio given by $E\gamma/\Gamma = 3.1 \times 10^{12}$, which together with the Mössbauer gamma-ray energy of 14.4 keV, provides an exceptional resolution of 1 in 10^{12}. This is the necessary requirement to detect hyperfine interactions in the nucleus. A hyperfine interaction either shift or lift the degeneracy of the energy levels. The shifts in the nuclear energy levels are observed in electric monopole interactions ($e0$) [27]. The degenerate nuclear levels are split into sublevels without shifting the centroid of the multiplet and is observed in the electric quadrupole interaction ($e2$) and magnetic dipole interaction ($m1$). Electric dipole interactions ($e1$) do not exist because of symmetry arguments, and interactions of a higher order ($m3$, $e4$, etc.) are negligible. The energy of the nucleus is described by the Hamiltonian

$$\hat{H} = \hat{H}_0 + E_0 + M_1 + E_2 + \ldots \quad (2.28)$$

where $\widehat{H}_0$ refers to all the terms of the Hamiltonian except the hyperfine interactions, E_0 represents the electric monopole interaction, M_1 is the magnetic dipole interaction and E_2 is the electric quadrupole interaction.

2.5.1 Electric Hyperfine Interactions

The electrostatic interaction [27, 43] between a nucleus with charge *Ze* and its surroundings has a total Coulomb interaction energy

$$E_e = \int \rho_n(\mathbf{r})\, V(\mathbf{r})\, d\tau \tag{2.29}$$

where $\rho_n(r)$ is the nuclear charge density at a point with coordinates $\mathbf{r} = (x_1, x_2, x_3)$ and $V(\mathbf{r})$ is the electrical potential at a point $\mathbf{r} = (x_1, x_2, x_3)$. As the nuclear diameter is small in comparison with the distance of the outside electric charge producing $V(\mathbf{r})$, the Taylor expansion can be used to approximate the potential near the origin. At a point $\mathbf{r} = 0$,

$$V(r) = V_0 + \sum_{i=0}^{3} \left(\frac{\partial V}{\partial x_i}\right)_0 x_i + \frac{1}{2} \sum_{i,j=1}^{3} \left(\frac{\partial^2 V}{\partial x_i\, \partial x_j}\right)_0 x_i x_j + \ldots \tag{2.30}$$

By substituting Equation (2.29) into Equation (2.28) gives

$$E_3 = V_0 \int \rho_n(\mathbf{r}) d\tau + \sum_{i=1}^{3} \left(\frac{\partial V}{\partial x_i}\right)_0 \cdot \int \rho_n(\mathbf{r}) x_i d\tau$$

$$+ \frac{1}{2} \sum_{ij=1}^{3} \left(\frac{\partial^2 V}{\partial x_i \partial x_j}\right)_0 \cdot \int \rho_n(\mathbf{r}) x_i x_j d\tau + \ldots \tag{2.31}$$

The first term in Equation (2.31) is the interaction energy with the potential if the nucleus is considered as a point charge. The second term describes the electric dipole moment which is zero due to symmetry arguments. The terms higher than the third order are negligible, thus only this term (E_3) is of interest and can be expressed as a sum of the two contributions,

$$E_3 = \frac{1}{2}\left[\sum_{i=1}^{3} V_{ii}\right] \int \frac{1}{3}\mathbf{r}^2 \rho_n(\mathbf{r}) d\tau + \frac{1}{6}\sum_{i,j=1}^{3} V_{ij} Q_{ij} \quad (2.32)$$

where,

$$Q_{ij} = \int \left(3x_i x_j - \delta_{ij}\mathbf{r}^2\right) \rho_n(\mathbf{r}) d\tau \quad (2.33)$$

is the nuclear quadrupole moment tensor, and

$$V_{ij} = \left(\frac{\partial^2 V}{\partial x_i \, \partial x_j}\right)_0 \quad (2.34)$$

is the electric field gradient (EFG) tensor at the nucleus. The first contribution in Equation (2.32) is the electric monopole interaction energy caused by the finite volume of the nucleus. The quadrupole interaction energy is the second contribution.

2.5.1.1 Electric Monopole Interaction: Isomer Shift

The electric monopole interaction [44] is the Coulomb interaction between protons and electrons (mainly *s*-electrons) penetrating the nuclear field. The source (S) material (e.g. ^{57}Co) is usually different to the absorber (A) material (e.g. ^{57}Fe) under study. Due to these differences, the electron densities set up by all *s*-electrons (1*s*, 2*s*, 3*s*, etc.) of the electronic shells are different at the nuclei of the source and the absorber. Therefore the electric monopole interactions are different in the source and the absorber, hence the nuclear ground and excited state levels are affected to different extents.

The simplest coordinate system arises where the coordinate axes point along the principal direction of the EFG tensor. In such a system [43] with *x, y, z* as the EFG tensor principle axes where V_{ij} is diagonal, its trace is given by Poisson's equation

$$V_{xx} + V_{yy} + V_{zz} = -4\pi\rho_e(0) \quad (2.35)$$

where $\rho_e(0) = -e|\psi(0)|^2$, is the electron charge density at the origin. If δE represents the first term in Equation (2.32), and when added to Equation (2.35), it becomes

$$\delta E = \frac{2\pi}{3} Ze^2 |\psi(0)|^2 \langle \mathbf{r}^2 \rangle \tag{2.36}$$

where $\langle \mathbf{r}^2 \rangle$ is the mean square radius of the nuclear charge distribution given by

$$\langle \mathbf{r}^2 \rangle = \frac{\int \mathbf{r}^2 \rho_n(\mathbf{r}) d\tau}{\int \rho_n(\mathbf{r}) d\tau} = \frac{\int \mathbf{r}^2 \rho_n(\mathbf{r}) d\tau}{Ze} . \tag{2.37}$$

The nuclear volume [27] and quantity $\langle \mathbf{r}^2 \rangle$ are different for each excitation state resulting in different electrostatic shifts δE for each nuclear state as shown in Figure 2.11, where the excited and ground states are shifted to different levels.

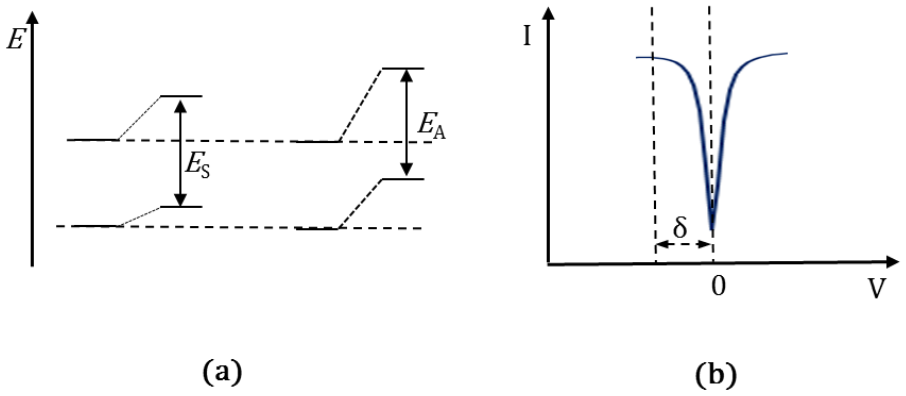

Figure 2.11: (a) Shifts in nuclear energy due to electric monopole interaction, and (b) Schematic of the resultant Mössbauer spectrum.

The energy [43] of the emitted γ-ray by a source is

$$E_S = E_0 + \delta E_S^e - \delta E_S^g \tag{2.38}$$

and resonant absorption can only occur if the γ-ray energy is

$$E_A = E_0 + \delta E_A^e - \delta E_A^g . \tag{2.39}$$

The shift δ in the peak position in the Mössbauer spectrum (Figure 2.11b) is known as the isomer shift, which is the difference between Equations (2.38) and (2.39),

$$\delta_{\mathrm{IS}} = E_{\mathrm{A}} - E_{\mathrm{S}} = \frac{2}{3}\pi Z\mathrm{e}^2[|\psi(0)|_{\mathrm{A}}^2 - |\psi(0)|_{\mathrm{S}}^2] \cdot \left[\langle \mathbf{r}^2\rangle_{\mathrm{e}} - \langle \mathbf{r}^2\rangle_{\mathrm{g}}\right] \qquad (2.40)$$

where $\langle \mathbf{r}^2\rangle_i$ are the mean square radii. If the atomic nuclei are considered to be uniformly charged spheres in the ground state with radius R_g, or with radius R_e in the excited state, then the charge densities are given by

$$\rho_{\mathrm{n}}^{\mathrm{g}} = \frac{Z\mathrm{e}}{4/3\pi \mathrm{R}_{\mathrm{g}}^3} \quad \text{and} \quad \rho_{\mathrm{n}}^{\mathrm{e}} = \frac{Z\mathrm{e}}{4/3\pi \mathrm{R}_{\mathrm{e}}^3} .$$

The mean squares of the radii, $\langle \mathbf{r}^2\rangle_{\mathrm{e}}$ and $\langle \mathbf{r}^2\rangle_{\mathrm{g}}$ can be evaluated using Equation (2.37), hence Equation (2.40) becomes

$$\delta = \frac{4}{5}\pi \mathrm{ZS`(Z)eR}^2 \left(\frac{\Delta \mathrm{R}}{\mathrm{R}}\right) \Delta\rho(0) = \alpha\Delta\rho(0) \qquad (2.41)$$

where $\Delta \mathrm{R} = \mathrm{R_e} - \mathrm{R_g}$, $\mathrm{R} = (\mathrm{R_e} + \mathrm{R_g})/2$. This indicates that the isomer shift, δ is directly proportional to $\Delta\rho(0)$ with α as the calibration constant. Equation (2.40) demonstrates that the isomer shift is basically a measure of the difference in the *s*-electron charge densities at the nuclei in the source and absorber. The calibration constant α may be positive or negative [43], and for ^{57}Fe, α is negative. The isomer shift, δ is very small for Fe (0.3 mm/s) which corresponds to an energy shift of $\approx 10^{-8}$ eV. This small amount of energy can only be detected by the Mössbauer effect.

The information [27] obtained from the isomer shift includes the oxidation state, spin states (high spin or low spin), electronegativity of ligands and character of bonds. The isomer shift depends on the *s*-electron densities (as a sum of contributions from all *s*-electron shells), however, it is often influenced by shielding effects from the *p*-, *d*- and *f*-electrons [45], which are unable to penetrate the nuclear field. The 3*d* electrons [34] partially shield the nuclear charge from the 4*s* electrons in the case of Fe. Increasing the number of 3*d* electrons at the ^{57}Fe atom will

therefore increase the shielding, thereby reducing the *s*-electron density at the ^{57}Fe nucleus and causing a positive isomer shift.

2.5.1.2 Electric Quadrupole Interaction: Quadrupole Splitting

Electric quadrupole interaction [40] arises when there is a detectible nuclear quadrupole moment and a nonzero EFG at the nucleus. This is the extent of deviation of the charge distribution from spherical symmetry and the non-uniformity of the electric field. The quadrupole moment is given in the *z*-axis of symmetry as

$$\mathrm{Q} = \frac{1}{\mathrm{e}} \int \rho_{\mathrm{n}}(\mathbf{r})\,(3z^2 - \mathbf{r}^2)\mathrm{d}\mathbf{r}. \tag{2.42}$$

Only nuclear states [27] with spin $I > ½$ have non-spherical charge distributions and can thus interact with an inhomogeneous electric field. The interaction splits the energy level of a nucleus state with spin $I > ½$ into $(2I + 1)$ sublevels. The Eigen values of these sublevels are given as the first order perturbation matrix from the Hamiltonian,

$$E_{\mathrm{Q}} = \frac{\mathrm{eQV_{zz}}}{4I(2I-1)}\,[3\mathrm{m}_I^2 - I(I+1)]\left(1 + \frac{\eta^2}{3}\right)^{\frac{1}{2}} \tag{2.43}$$

where $\mathrm{m}_I = -I, -I+1, \ldots I-1$ and I is the nuclear spin quantum number and η is the asymmetry parameter of the electric field given by

$$\eta = \frac{\mathrm{V_{xx}} - \mathrm{V_{yy}}}{\mathrm{V_{zz}}}.$$

In the case of ^{57}Fe with $I = ⅜$, a pure electric quadrupole interaction splits the excited 14.4 keV state into sublevels of Eigen values,

$$E_{\mathrm{Q}} = \pm\frac{1}{4}\,\mathrm{eQV}_{zz}\left(1 - \frac{\eta^2}{3}\right)^{\frac{1}{2}}. \tag{2.44}$$

The electric quadrupole interaction of ^{57}Fe with I = ⅜ in the 14.4 keV state and I = ½ in the ground state is shown in Figure 2.12.

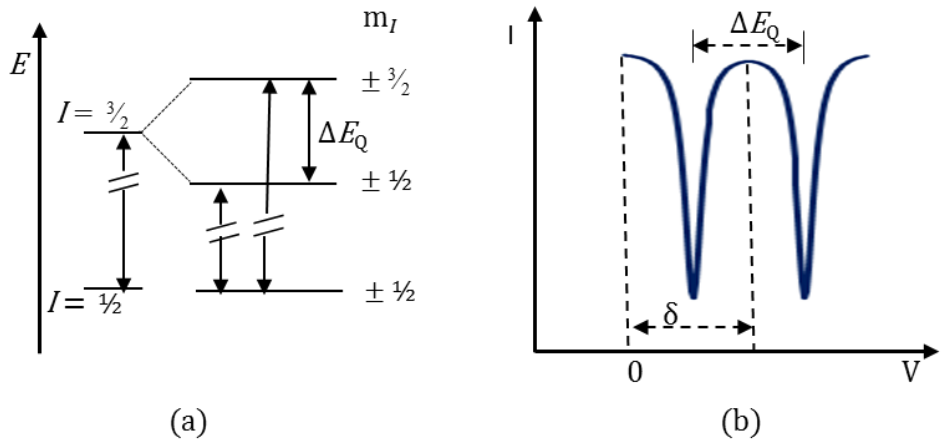

Figure 2.12: Effects of the electric quadrupole splitting in the energy levels (a), and (b) the resultant Mössbauer spectrum.

Quadrupole splitting is the energy difference ΔE_Q corresponding to Δ between the two resonant lines. This is important in the chemical applications of the Mössbauer effect as it provides information associated with bond properties, molecular and electronic structure.

2.5.2 Magnetic Hyperfine Interaction: Magnetic Splitting

The magnetic dipole interaction or Zeeman effect is the interaction [27] between a nonzero magnetic dipole moment $\vec{\mu}$ with a magnetic field $\vec{H}$ at the nucleus in the energy state E, and having a quantum spin number $I > 0$. This effect is described by the Hamiltonian

$$\hat{H}_m = \hat{\vec{\mu}} \cdot \hat{\vec{H}} = -g_N \beta_N \hat{\vec{I}} \cdot \hat{\vec{H}} \qquad (2.45)$$

where g_N is the nuclear Landé factor, $\beta_N = e\hbar/2Mc$ is the nuclear magneton (where M is the mass of the nucleus). The Eigen values E_M to $\hat{H}_M$ are obtained by diagonalising the first order perturbation matrix,

$$E_{\mathrm{M}}(\mathrm{m}_I) = \frac{-\mu \mathrm{H} \mathrm{m}_I}{I} = \mathrm{g}_{\mathrm{N}} \beta_{\mathrm{N}} \mathrm{H} \mathrm{m}_I. \qquad (2.46)$$

The nuclear Zeeman effect splits the nuclear state with spin number I into $2I + 1$ substates characterised by the magnitude of the nuclear magnetic spin quantum number m_I. The influence of the magnetic dipole interaction in ^{57}Fe is shown in Figure 2.13, where I = ³⁄₂ level splits into four substates, and the ground state with I = ½ into two substates. The selection rules for magnetic dipole transition are $\Delta I = 1$ and $\Delta m = 0, \pm 1$, resulting in six allowed transitions for ^{57}Fe (Figure 2.13b).

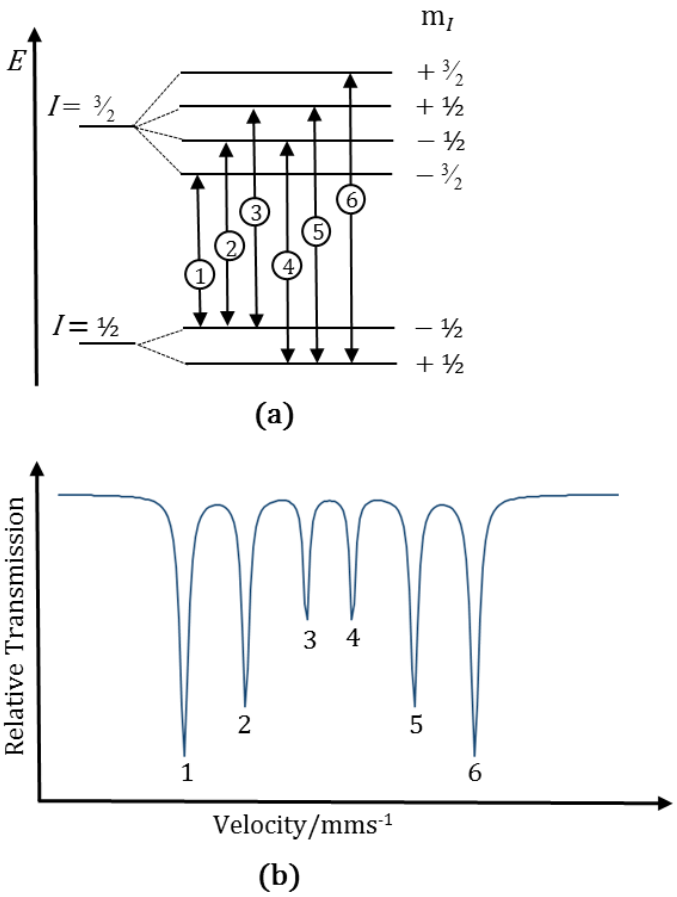

Figure 2.13: (a) Magnetic dipole interaction leads to splitting of nuclear energy levels into 2I + 1 substates. (b) Example of a ^{57}Fe magnetically split Mössbauer spectrum.

The effective magnetic field acting on the nucleus is determined from the magnetic hyperfine splitting. The most important sources contributing to the effective magnetic field are the Fermi contact field (H^c) arising from a net spin-up or spin-down *s*-electron density, an anisotropic contribution (H^L) from the orbital motion of valence electrons with quantum number *L*, and a spin dipolar contribution (H^d) due to the non-spherical distribution of the electron spin density.

Magnetic dipole splitting [40] gives information on the spin interaction processes. This information relates to electron configuration, magnetic relaxation, magnetic moment, spin value, magnetic transition temperature and spin flop processes.

Chapter 3

Experimental Details

3.1 Introduction

Tungsten carbide (WC) and metal binder powders are ball milled to achieve a homogeneous mixture. The milled powders are pressed into compacts and vacuum sintered to achieve the hardmetal composite. The powder processing stages, which include milling, drying and pressing are described, as well as the sintering cycle. After sintering, the densities of the materials were measured, and the stoichiometry of the sintered materials were assessed using magnetic saturation, X-ray diffraction and microstructural examination. Coercivity and hardness measurements were carried out to monitor structural changes in materials resulting from the different sintering temperatures. The microstructures were examined using optical and HRSEM (High Resolution Scanning Electron Microscopy), and the elemental compositions were determined using energy dispersive X-ray analysis (EDS). Transmission Mössbauer Spectroscopy (TMS) was used to investigate the milled powders, whilst the sintered materials were analysed using Conversion electron Mössbauer Spectroscopy (CEMS). The powder processing, sintering and the routine quality control testing of the sintered hardmetals was carried out using the facilities at Pilot Tools (Pty) Ltd, Johannesburg.

3.2 Powder Preparation

3.2.1 Starting powder and material compositions

The WC powder was obtained from Pilot Tools (Pty) Ltd, and the metal powders (Fe, Ni and Mn) were obtained from Sigma Aldrich. The purity and grain size of the starting powders are given in Table 3.1.

Table 3.1: Starting powder purity and grain size.

Powder	Purity (%)	Grain Size (µm)
WC	99.9	2 - 4
Fe	99.5	1
Ni	99.9	2
Mn	99.9	1

The compositions of the tungsten carbide hardmetals selected for this work are summarised in Table 3.2. The mass of WC was kept constant at 90 wt% for all the grades, whilst the balance was made up of one or a combination of the binder metals listed in Table 3.1.

Table 3.2: Compositions of the tungsten carbide hardmetals.

Powder Batch number	WC Weight%	Fe Weight%	Ni Weight%	Mn Weight%
1	90	10	-	-
2	90	7	3	-
3	90	8.5	-	1.5
4	90	-	10	-

The metal binder ratios of Fe/Ni and Fe/Mn were selected to retain austenitic structures [1] of the binder at room temperature after sintering.

3.2.2 Milling Procedure

Powder batches of 100 g each were ball milled in a laboratory scale ball mill as shown in Figure 3.1. The purpose of ball milling is to achieve a homogeneous mixture of the powders [46] and to break up particle agglomerates. The steel pot used in the ball milling process is 70 mm in diameter and 80 mm in length. Sintered WC-Co balls, approximately 10 mm in diameter, was used as the milling media and the ball-to-powder mass ratio used was 3:1. As the energy of the milling process is considerably high, a protective liquid is used to minimise temperature rise and prevent oxidation. Hence, the powders were wet milled using ethanol to prevent heat generation and oxidation of the powders [46]. The quantity of ethanol that is added to the mix is 18 wt% of the powder mass. A wax lubricant, polyethylene

glycol (PEG), was also added to the mixture to facilitate compaction of the milled and dried powders. The mass of PEG added to the slurry is 2 wt% of the powder mass.

The slurry consisting of the powders, solvent and lubricant was milled using sintered WC-Co balls for 20 hours at a speed of 140 rpm.

Figure 3.1: Laboratory scale ball mill.

3.2.1 Drying and pressing of the powders

After milling, the slurry was dried using a Rotary Vapour Dryer, model IKA HB 10. The apparatus is shown in Figure 3.2. The solvent was dried off at a temperature of 40 °C using a rotation speed of 60 rpm for 30 minutes. The drying temperature (40 °C) is lower than the boiling point of ethanol (78 °C) to prevent oxidation of the powders [47]. The dried powder was then screened through a 150 µm sieve, and pressed into green compacts at a pressure of 140 MPa. The size of the pressed compacts were approximately 12×12 mm by 6 mm thick.

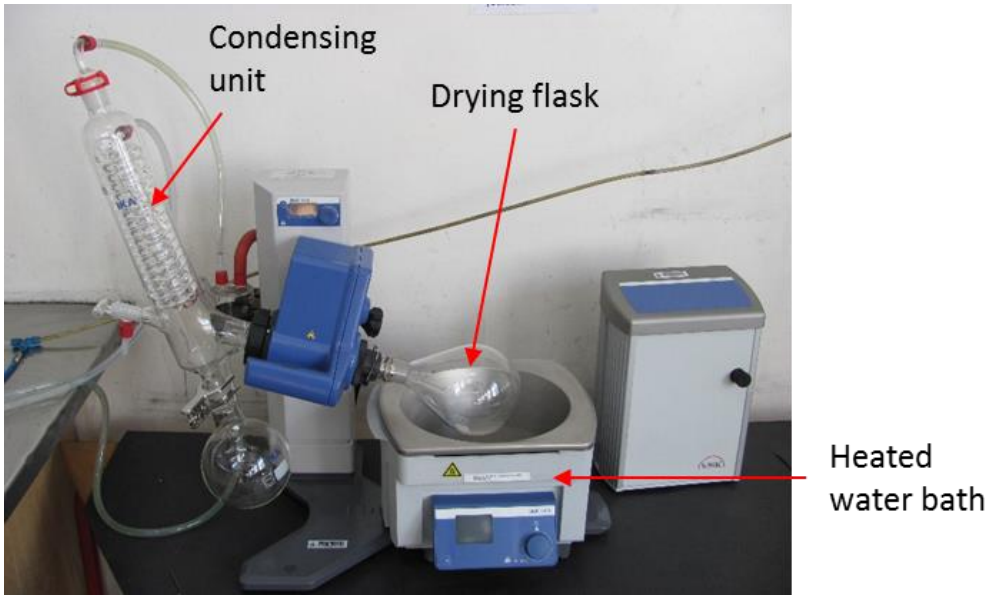

Figure 3.2: Rotary Vapour Dryer used for drying the slurries after ball milling.

3.3 Sintering

The green compacts were vacuum sintered at three different temperatures, 1340 °C, 1430 °C and 1510 °C, using an ULTAR-TEMP Sinter-Hip furnace at Pilot Tools (Pty) Ltd. Standard production sintering cycles were employed to sinter the materials, and an example of a typical sintering cycle is shown in Figure 3.3. The first stage of the sintering cycle is dewaxing or removal of the PEG. In this initial stage, the furnace is heated under vacuum to 270 °C and dwelled for 65 minutes. Hydrogen gas is introduced to allow the dewaxing process to occur. The dewaxing process is achieved in four steps at a series of temperatures (from 270 °C to 450 °C) and dwell times to allow complete removal of the PEG.

The next stage of the cycle is carbon control. The furnace is heated under vacuum from 450 °C to 1000 °C. At 1000 °C the vacuum pumps are switched off and a combination of methane and hydrogen gasses are allowed to flow through for 2 hours for carbon correction. Thereafter, the furnace is once again heated under vacuum to the required sintering temperature, and dwelled for 90 minutes at the sintering temperature. The last stage in the sintering cycle is hot isostatic pressing

(HIP) for a further 20 minutes at the sintering temperature under argon atmosphere, at a pressure of 640 psi to eliminate all surface porosity [48].

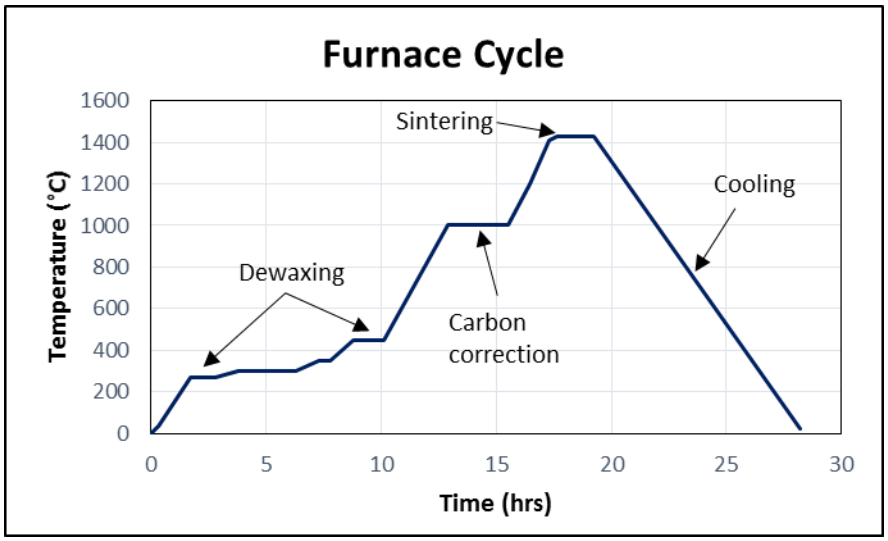

Figure 3.3: Example of a typical sintering cycle.

3.4 Characterisation of the sintered materials

3.4.1 Density measurements

The densities of cemented carbides [49] were measured to determine the levels of porosity in the sintered material. As density is sensitive to composition [4], it varies due to levels of porosity for a fixed composition. Density is an important parameter used to ascertain the effectiveness of the sintering temperature. The ideal situation is to achieve a 100% dense material after sintering, however in cemented carbides, densities of 99.5% are acceptable. Density measurements were carried out using a SHIMADZU AY120 density balance. The apparatus is shown in Figure 3.4.

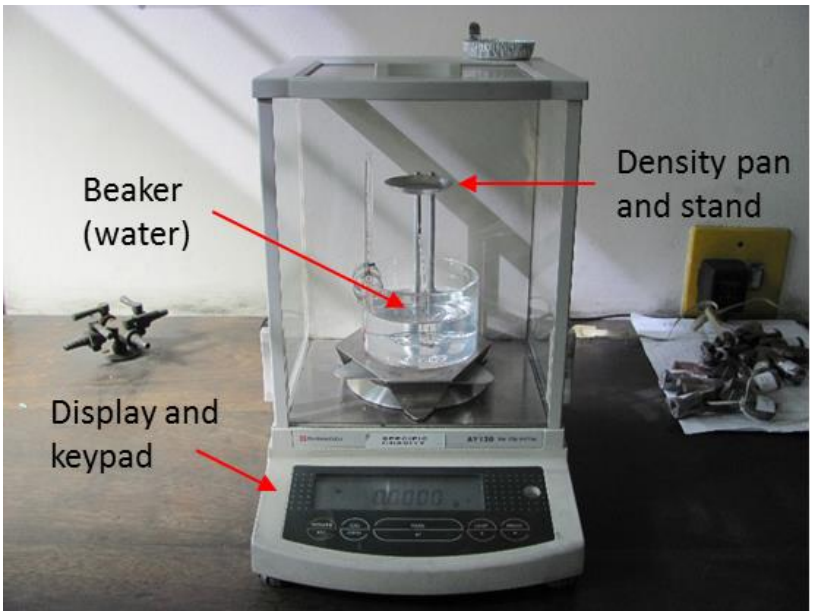

Figure 3.4: SHIMADZU AY120 density balance.

Density is measured using the Archimedes principle and is covered by an ISO standard, ISO 3369 [50]. The real density ρ_r is calculated from the equation

$$\rho_r = \frac{m_1 \rho_w}{m_1 - m_2} \tag{3.1}$$

where ρ_w is the density of distilled water, m_1 is the weight of the sample in air and m_2 is the weight of the sample in distilled water. The theoretical density is calculated from the mass and density of the individual components. The theoretical density ρ_t of the individual material constituents used for this work is given in Table 3.3.

Table 3.3: Theoretical densities of the individual components.

Constituent	WC	Fe	Ni	Mn
Density (g/cm^3)	15.7	7.9	8.9	7.2

The theoretical density of the sintered hardmetal can therefore be calculated by the following equation

$$\rho_t = 100\ \text{wt\%} \left(\sum \frac{\text{constituent wt\%}}{\text{constituent } \rho} \right)^{-1} . \quad (3.2)$$

As an example, the theoretical density for WC-7Fe/3Ni can be calculated as follows

$$\rho_t = 100\ \text{wt\%} \left(\frac{90\ \text{wt\%}}{15.7\ \text{g/cm}^3} + \frac{7\ \text{wt\%}}{7.9\ \text{g/cm}^3} + \frac{3\ \text{wt\%}}{8.9\ \text{g/cm}^3} \right)^{-1} . \quad (3.3)$$

3.4.2 Magnetic properties

3.4.2.1 Magnetic Saturation

Magnetic saturation or specific saturation magnetisation σ_s provides information on the composition of the ferromagnetic binder phase of the cemented carbide. It gives an indication of the amount of tungsten dissolved in the binder [49], and an indirect indication of the carbon levels [4]. When a ferromagnetic material encounters a magnetic field [14], it is magnetised and the level of magnetisation increases with the field until it reaches a maximum. The specific saturation magnetisation σ_s is a ratio of the maximum magnetic moment and mass of the material. The magnetic moment is determined by moving the sample out of a magnetic field and measuring the induced e.m.f. in a coil. The integral is proportional to the σ_s value of the sample, given that it was saturated in the field. The microprocessor of the reading unit integrates the emf and does the required data processing. It calculates the value of either the σ_s or the content of the ferromagnetic phase.

The sintered materials were measured using a SETARAM Sigmameter 3035 (Figure 3.5) at Pilot Tools (Pty) Ltd. A pure Ni standard was used to check the calibration of the instrument. The magnetic saturation of Ni is 54.5 G.cm^3/g, therefore, samples produced with 10 wt% Ni (WC-10Ni) should return values of 5.4 G.cm^3/g if there is no tungsten in solution during the sintering process.

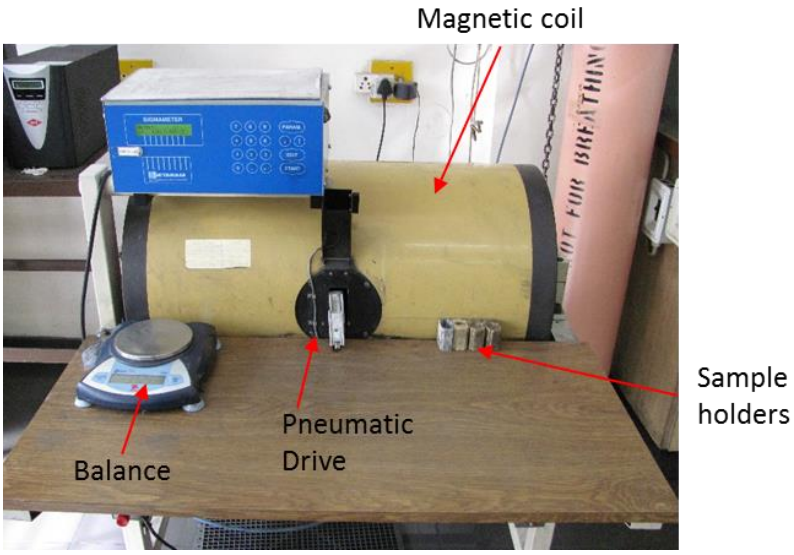

Figure 3.5: SETARAM Sigmameter 3035 used for measuring the magnetic saturation of the sintered samples.

3.4.2.2 Coercivity

Coercivity measurements [4] provide information on the degree of sintering, binder distribution and WC grain size in sintered carbides. The coercive field strength H_C is measured in a magnetic coil [51], in an open magnetisation circuit. The sample is magnetised to saturation in the H_C coil, and the polarisation is measured by fluxgates (probes). An opposing field is built up until the polarisation is zero, and the strength of the opposing field at which the sample polarisation is zero is the coercive field strength H_C.

The samples were measured using a Dr Foerster KOERZIMAT 1.095 apparatus as shown in Figure 3.6. Internal sintered carbide standards were used to check the calibration of the instrument, and the coercivity values are an average of the positive and negative H_C values.

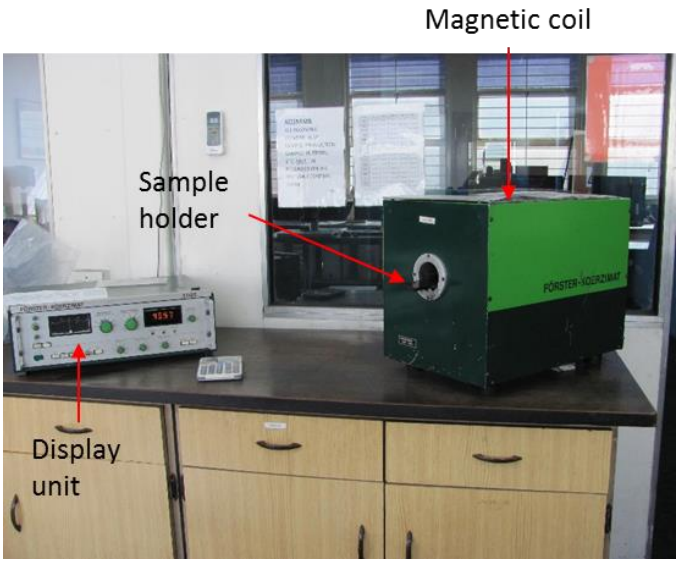

Figure 3.6 Dr. Foerster KOERZIMAT 1.095 apparatus used for measuring the coercivity of the sintered samples.

3.4.3 Sample preparation of the sintered carbides

The samples were cut using electro-discharge machining (EDM cutting). A 1 mm thick slice was cut from each sample and polished for CEMS investigations. The opposite sections were also polished for microstructural examination and further structural analysis. The cut sections were first hot mounted in Bakelite using a Leco PR-32 hot mounting press (Figure 3.7).

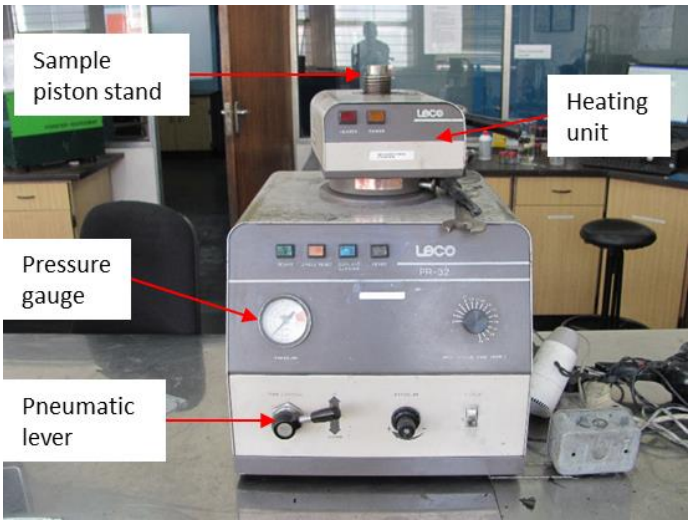

Figure 3.7: Leco PR-32 hot mounting press.

The mounted samples were ground and polished to remove the surface damage from EDM cutting, and to obtain a smooth surface finish necessary for microstructural examination. The grinding and polishing operations were performed using a Struers Labo-Pol 5 polishing machine. The apparatus is shown in Figure 3.8. Grinding was performed using metal-bonded diamond discs, Struers Piatto 220 and 1200 grit sizes. The samples were polished using AKASEL (Plaran, Daran and Napal) polishing cloths using Diamaxx diamond slurries, 9 µm, 3 µm and 1 µm. The grinding and polishing parameters are given in Table 3.4.

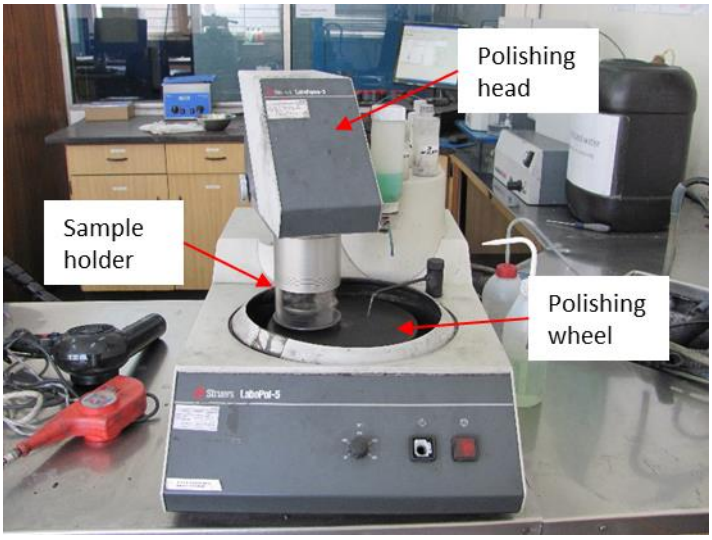

Figure 3.8: Struers Labo-Pol 5 polishing machine.

Table 3.4: Grinding and polishing parameters.

Process	Stage	Grinding wheel / Polishing Cloth	Lubricant	Speed (rpm)	Load (N)	Time (min)
Grinding	rough	Piatto 220	water	300	30	10
	fine	Piatto 1200	water	300	30	10
Polishing	rough	Plaran	Diamaxx - 9µm	300	30	10
	medium	Daran	Diamaxx - 6µm	200	20	5
	fine	Napal	Diamaxx - 3µm	200	20	3

3.4.4 Hardness

Hardness is defined as the resistance of a material to plastic deformation by penetration [52]. Hardness is not an intrinsic property of a material but rather a characteristic property. It is an important property of cemented carbides that provides information on the composition and structure of the material [4]. Vickers hardness (HV) was measured using a 30 kg load on sintered and polished surfaces of the samples, using a Mitutoyo AVK-CO hardness tester (Figure 3.9). The test procedure is covered by ISO3878 [53].

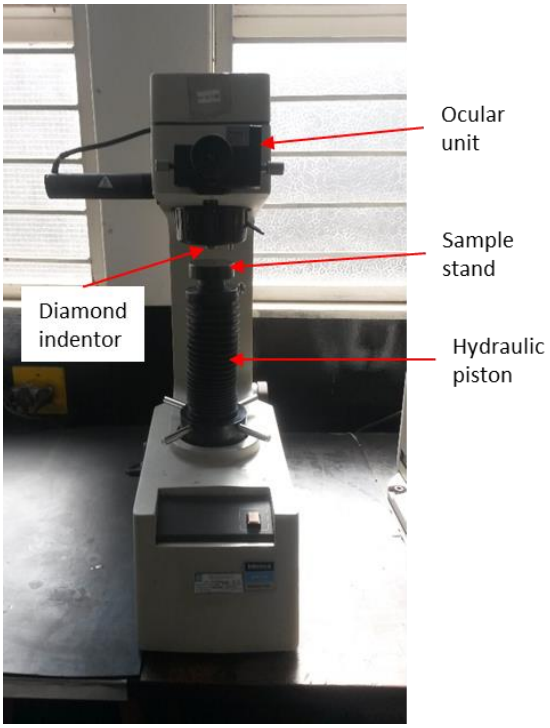

Figure 3.9: Mitutoyo AVK-CO (Vickers) hardness tester.

The Vickers hardness involves indenting the material under study with diamond pyramid indenter which has an angle of 136° between the opposite faces [52]. A load is applied for 15 seconds and the diagonals are measured as shown in the schematic diagram in Figure 3.10. The Vickers hardness number is obtained by dividing the load by the area of the indentation as given by

$$\mathrm{HV} = \frac{2F\sin\left(136^\circ/_2\right)}{d^2} \tag{3.4}$$

where F is the load in kgf, and d is the mean of the diagonals.

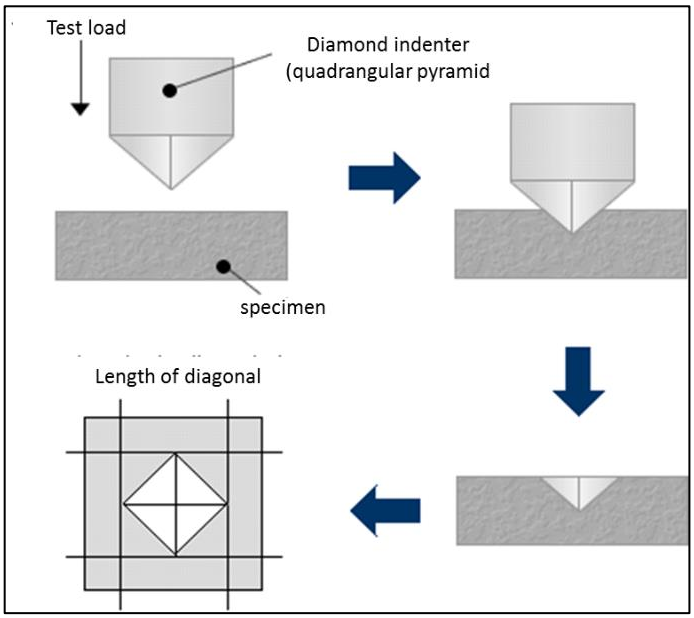

Figure 3.10: Schematic of the Vickers hardness test [53].

3.4.5 Microstructural examination

3.4.5.1 Optical Microscopy

The macro structural features were assessed on the polished specimens using a light or optical microscope to determine whether there are defects such as porosity, eta-phase or graphite present in the sintered materials. The samples were examined using a Zeiss AX10 metallurgical microscope (Figure 3.11) at magnifications ranging from 100x to 500x. To evaluate whether there is eta-phase present, the samples were lightly etched for 5 to 10 seconds in Murakami's reagent (1:1 mixture of 10% $KCNO_3$ and 10% NaOH), cleaned with distilled water and dried with ethanol.

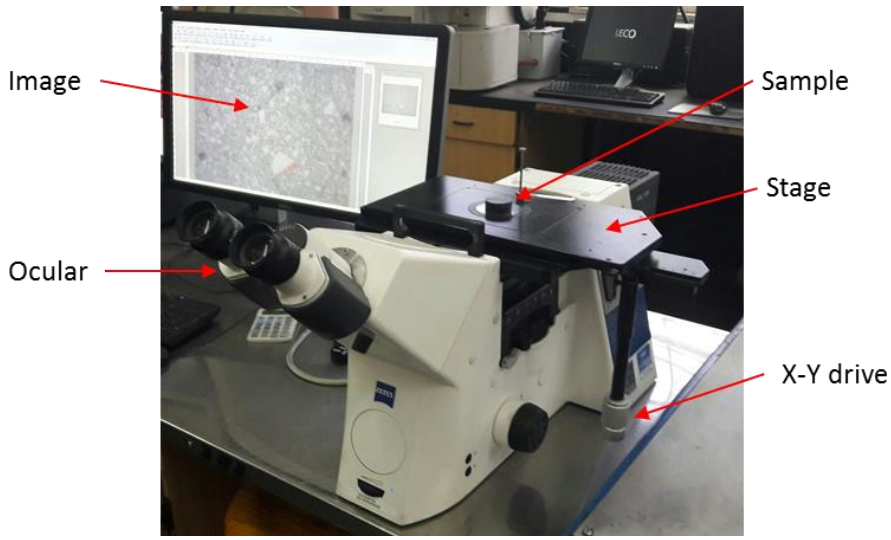

Figure 3.11: Zeiss AX10 metallurgical microscope.

3.4.5.2 Scanning Electron Microscopy

The microstructures were examined using a Zeiss Sigma high resolution scanning electron microscope (HRSEM) at the School of Chemical and Metallurgical Engineering, University of the Witwatersrand. A photograph of the HRSEM is shown in Figure 3.12. The samples were examined at an accelerating voltage 10 kV using both secondary and backscattered imaging modes. The microstructures were examined at various magnifications ranging from 500x to 20 000x to assess the quality of the sintered materials. The microstructural assessment includes homogeneity of the structure, WC contiguity, binder pool size and distribution, and morphology of the WC grains. Energy dispersive X-ray spectroscopy (EDS) was also utilised for determining the elemental compositions of the materials. This technique was also used to determine whether there were any contaminants in the sintered materials.

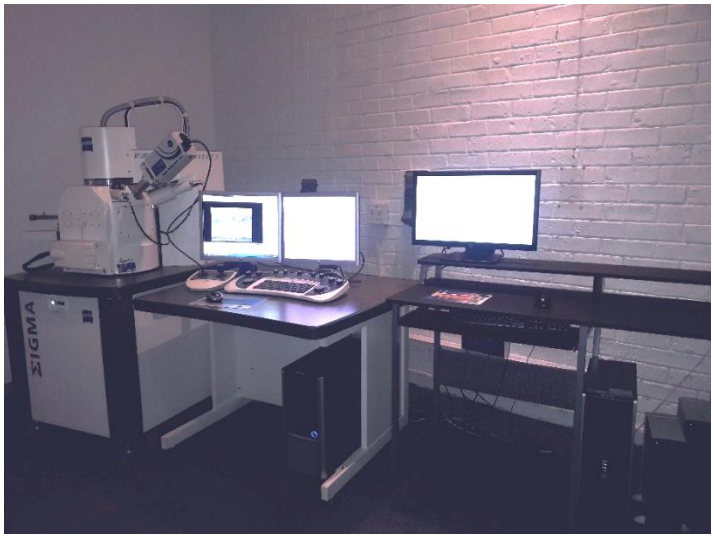

Figure 3.12: Zeiss Sigma high resolution scanning electron microscope.

3.4.6 X-ray Diffraction

X-ray diffraction (XRD) measurements were carried to determine the phase compositions of the milled powders, and the sintered components using a Bruker D2 Phaser desktop system (Figure 3.13) at the X-ray Diffraction Unit at Wits University. The basic principles of the technique were discussed in Chapter 2. Measurements were performed on the polished sections of the sintered samples at 30 kV using a cobalt source. The samples were scanned from 20° to 100° 2θ angles at a 0.026° step size.

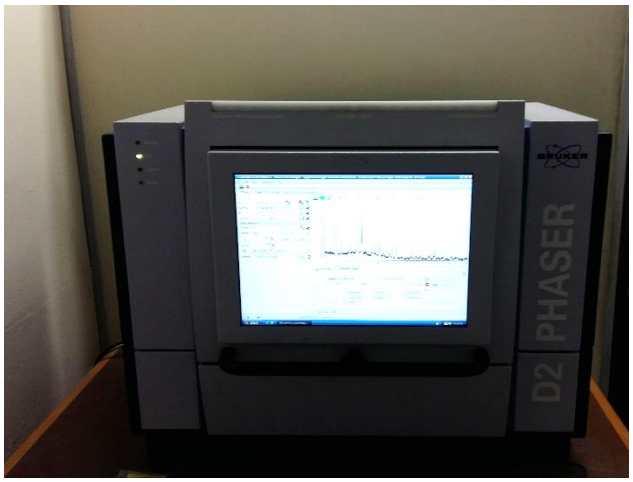

Figure 3.13: D2 Phaser desktop X-ray diffractomer.

3.4.7 Mössbauer Spectroscopy

The milled powder samples were investigated using Transmission Mössbauer Spectroscopy, whilst the sintered materials were investigated using Conversion electron Mössbauer Spectroscopy (CEMS) at the WITS Mössbauer Laboratory at the School of Physics. In both approaches, ^{57}Fe Mössbauer was used.

3.4.7.1 Decay scheme of ^{57}Co

In Mössbauer spectroscopy, the source and absorber are isotopes of the same atom as discussed in Chapter 2. The source used for the measurements within this project is radioactive ^{57}Co, embedded in a rhodium (Rh) matrix [54] with a half-life ($t_{½}$) of 270 days and an activity of 50 mCi. Figure 3.14 shows how ^{57}Co undergoes spontaneous electron capture transition to give a metastable state of ^{57}Fe which in turn decays to the ground state through the emission of gamma rays with an energy of 14.4 keV. This is the radiation energy required for ^{57}Fe Mössbauer spectroscopy. The spin and parity for the first excited state is $-$ ³⁄₂, and $-$ ½ for the ground state [45, 55].

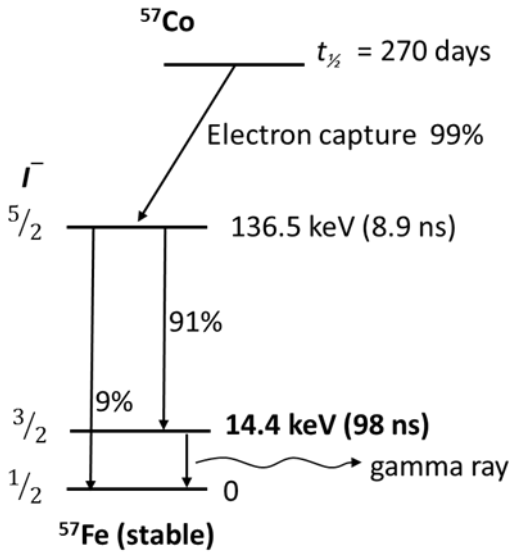

Figure 3.14: Illustration of the decay scheme for ^{57}Co [54].

3.4.7.2 Transmission Mössbauer Spectroscopy (TMS)

The basic elements for the Mössbauer spectrometer [27] consists of a source, absorber (sample), detector and a motorised drive to impart the Doppler velocity to the source as depicted in Figure 3.15.

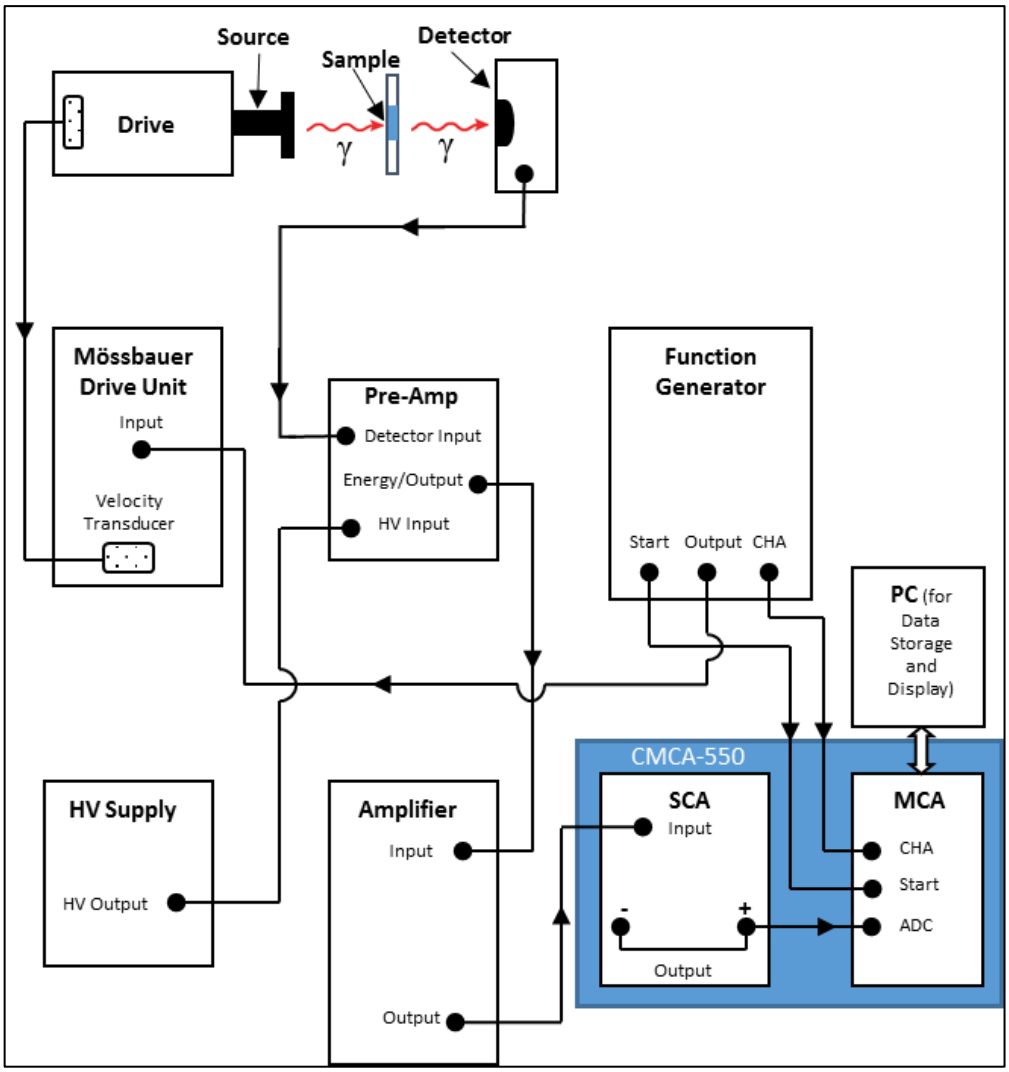

Figure 3.15: Schematic layout of the experimental set-up for Transmission Mössbauer Spectroscopy [57].

The system is connected to a pre-amplifier, amplifier, single channel analyser, multichannel channel analyser and a computer for visuals and data storage. The function [56] of the components for ^{57}Fe Mössbauer are as follows:

a) Source – radioactive ^{57}Co embedded in a Rh matrix.
b) Absorber – sample containing ^{57}Fe in powder form, thin foil or transparent solid.
c) Detector – a gas proportional counter filled with Xe, Kr or Ar gas used to detect gamma rays. The detector generates pulses of a size proportional to the energy of the incident gamma ray.
d) Pre-Amplifier – conditions the pulses from the proportional counter so that they can be applied to the input of the amplifier.
e) Amplifier – enhances the amplitude of the pulses as required for input into the Pulse-Height Analyser, and shapes the pulses to improve the signal-to-noise ratio.
f) Multi-Channel Analyser (MCA) – an electronic board in the desktop computer that receives the analog pulses from the proportional counter and amplifier. The board contains a Pulse-Height Analyser (PHA) for producing a gamma ray histogram. The board also contains a Single-Channel Analyser (SCA) with upper and lower discriminators, and a Multi-Channel Scaler (MCS) that generates a histogram of counts versus time.
g) Pulse-Height Analyser (PHA) – a unit which produces an energy spectrum by quantifying the height of the pulses from a particle detector by counting the number of pulses at each height, and recording each number in a bin or channel that corresponds to the pulse height. The Y-axis of the resulting histogram represents the number of counts, and the X-axis is proportional to the energy.
h) Discriminators – pulse height comparators on the MCA card with upper and lower threshold adjustments to select pulses with amplitudes either above or below the pre-set limits.
i) Single-Channel Analyser (SCA) – produces a logic pulse whenever the gamma energy falls within the energy window defined by the PHA discriminator thresholds.
j) Linear Motor (Drive) – an air bearing motor that translates the axial position of a shaft with a mount for the ^{57}Co source. The motor is programmed to

reciprocate in a triangular velocity profile and generates a pulse once each cycle in order to trigger a sweep of the Multi-Channel Scaler.

The set-up of the Transmission Mössbauer system used for the analysis of the milled carbide-metal powders is shown in Figures 3.16a and b.

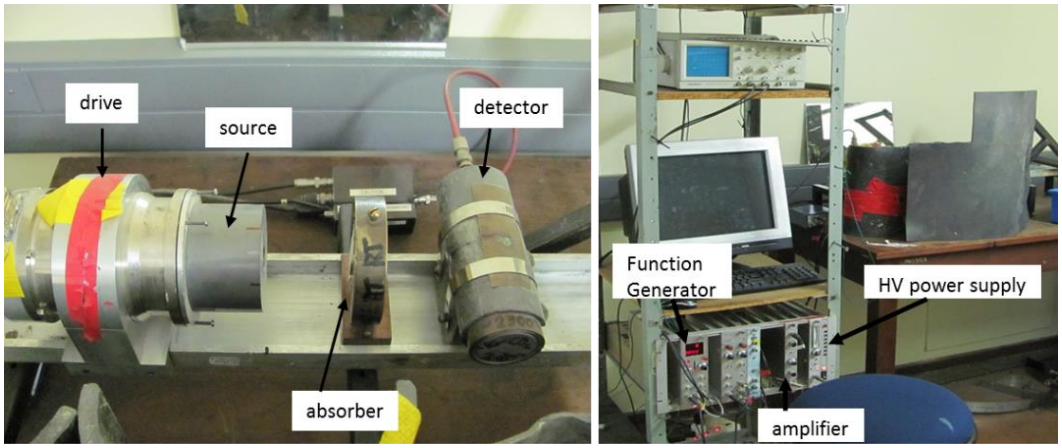

Figure 3.16: Arrangement of the source, sample (absorber) and detector in transmission mode (a), and the electronics (b).

A high voltage of 2100 kV is used for TMS. Pulses from the detector are first pre-amplified, then amplified through an amplifier, and passed through a multi-channel analyser. The data acquisition module used is a CMCA-550, and is controlled using Wissoft 2003 software [57]. Data is first acquired in Pulse-Height (PHA) mode which analyses the analog pulses. A spectrum representing the stochastic frequency of each pulse height is collected between 0 and 10 volts. When an input pulse is detected, its height is digitally determined and the pulse is allocated to a certain channel number corresponding to its height. A data acquisition window can be set in Wissoft 2003 which results in the data acquisition module CMCA-550 discarding all input pulses outside of this window. Only input pulses with amplitudes within the set window range of Lower Level (LL) and Upper Level (UL) are stored. A full pulse-height spectrum for ^{57}Fe Mössbauer shows peaks at 6 keV, 14.4 keV and 21 keV as shown in Figure 3.17. Only the 14.4 keV line is selected in PHA mode for Mössbauer spectroscopy.

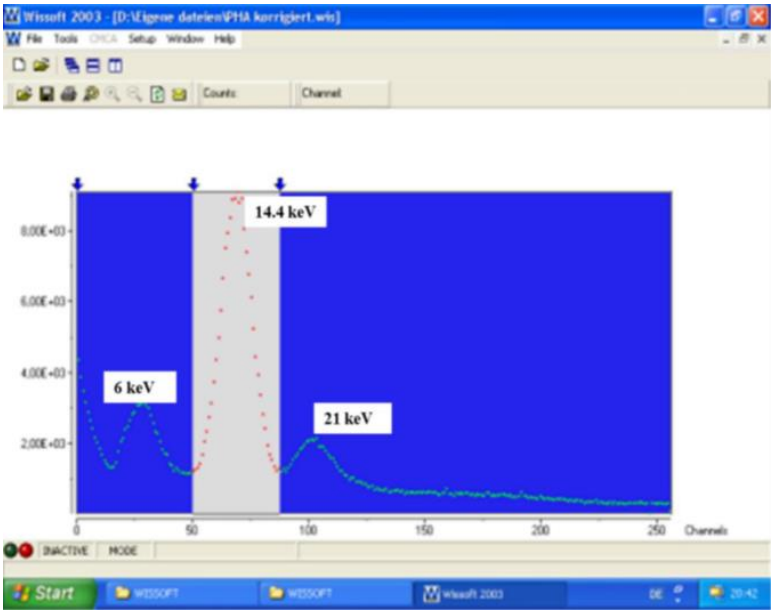

Figure 3.17: PHA spectrum of ^{57}Co showing the different energy lines, and the selection of the 14.4 keV line [58].

The mode is then switched to Multi-Channel Scaling (MCS) where the analog pulses which are fed from the main amplifier to the "ADC" (analogue digital converter) of the CMCA-550 are then converted to digital values. In the MCS mode only pulses that have heights in the selected voltage range are counted. Each velocity value appears twice during a channel sweep and hence during a cycle of source motion. The spectrum is doubled as a result and thus, the spectrum is folded around its symmetry point at about half of the total number of channels giving the final Mössbauer spectrum.

3.4.7.3 Conversion Electron Mössbauer Spectroscopy (CEMS)

Mössbauer investigation of the sintered cemented carbides were carried out using the CEMS technique. The conversion electron or backscattering technique is used in the surface characterisation of solid materials [58]. It is a surface sensitive technique as conversion electrons used in CEMS have a small range, 200 to 300 nm with the ^{57}Fe isotope [59]. In this technique, it is not γ-rays but conversion electrons that are detected.

The absorbing nucleus will be in an excited state after resonant absorption of the 14.4 keV Mössbauer γ-rays emitted from the source [59]. The energy that the absorber gains can be discharged either in the form of a photon or by transfer to an outer electron. Those electrons which are ejected from the outer shell in this manner are known as *conversion electrons*. As these electrons are predominantly ejected from the K-shell, the conversion electrons are known as K-conversion electrons. The isotope ^{57}Fe is particularly suitable for use in CEMS as the process of inner-electron conversion occurs far more frequently than the decaying nucleus through the emission of a γ-quantum [59].

The process of inner-electron conversion could be followed by the emission of an Auger electron. The resulting energies of these electrons are 5.3 keV and 6.3 keV for KLL and KLM-Auger electrons, respectively. The term KLM represents those electrons emitted from the M-shell and whose energy is transferred to them by electrons from the L-shell. In addition to primary electrons (Auger and conversion electrons), secondary electrons may also be emitted. The Compton and photo-electrons that are produced by the electronic absorption of γ-radiation with energies of 14.4 keV, 122 keV and 136 keV, lead to the presence of additional background when using the CEMS technique. A schematic of the CEMS processes are shown in Figure 3.18.

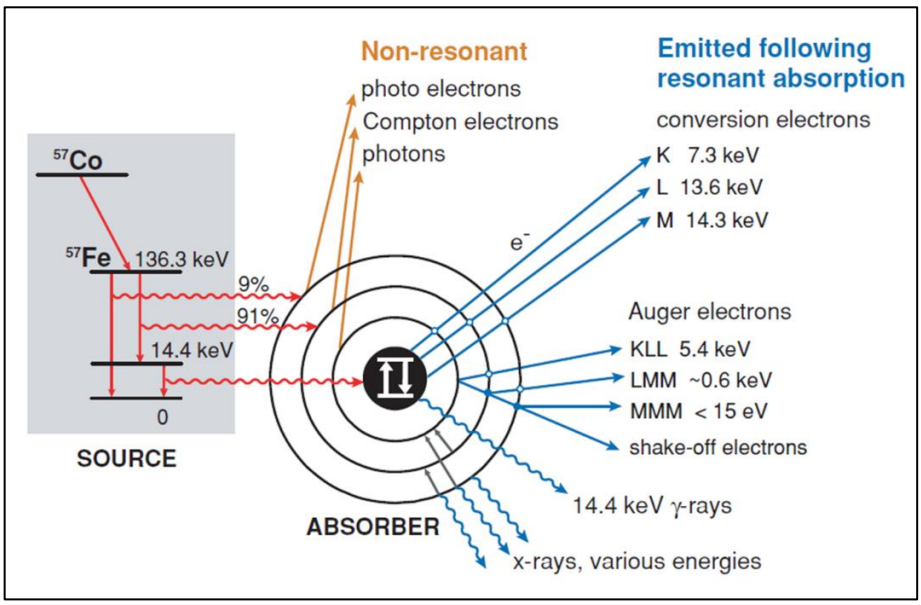

Figure 3.18: A schematic diagram showing the decay scheme for ^{57}Co and the various back-scattering processes for ^{57}Fe [61].

The efficiency of electron detection as well as good signal-to-noise ratio are crucial to improve the count rate in the CEMS technique, which depends on the design of the detector. A parallel-plate avalanche detector (PPAD) is used which consists of flat-plate electrodes coated with graphite. The sample is mounted onto the electrode as shown in Figure 3.19. The counting gas that is used can be any organic polyatomic gas, however acetone gas is preferred. In the detector, the sample and the emitted electrons are in an electric field [60]. When conversion electrons are emitted, they accelerate towards an anode with an electric potential on it. As electrons move towards the anode, they strike other atoms, ionising them which results in further electron emission. This process continues until an electron avalanche eventually strikes the anode causing a measurable spike in voltage. This small spike is amplified and measured to proportionally calculate the energy of the original conversion electron.

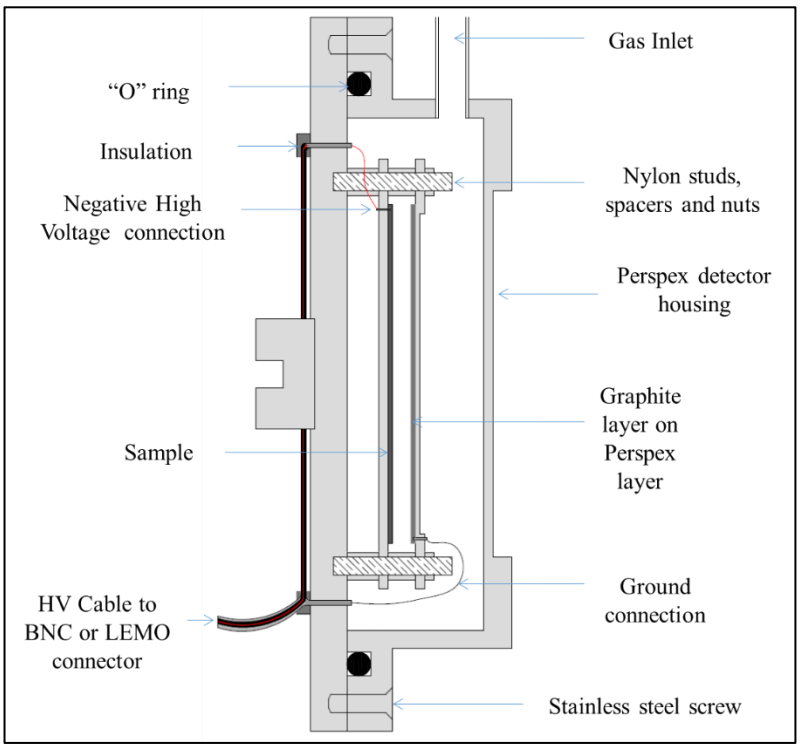

Figure 3.19: Schematic diagram of a typical PPAD [57].

The PPAD used for the CEMS investigation of the sintered carbide materials is shown in Figure 3.20. The housing of the detector and parallel plates are manufactured from Perspex. The parallel plates are coated with conductive graphite paint, and the sample is mounted to the cathode using carbon tape. The whole detection system (PPAD) is covered with aluminium foil and connected to a tank (gas reservoir), which is pumped to achieve a vacuum in the tank and the detector. The system is then pressurised with acetone gas to a pressure of 20 to 25 mBar. The detector is then connected to the pre-amplifier of the Mössbauer spectrometer using a lemo connection as shown in Figure 3.21. The electronics for the CEMS system is similar to the transmission system described in Section 3.4.7.2.

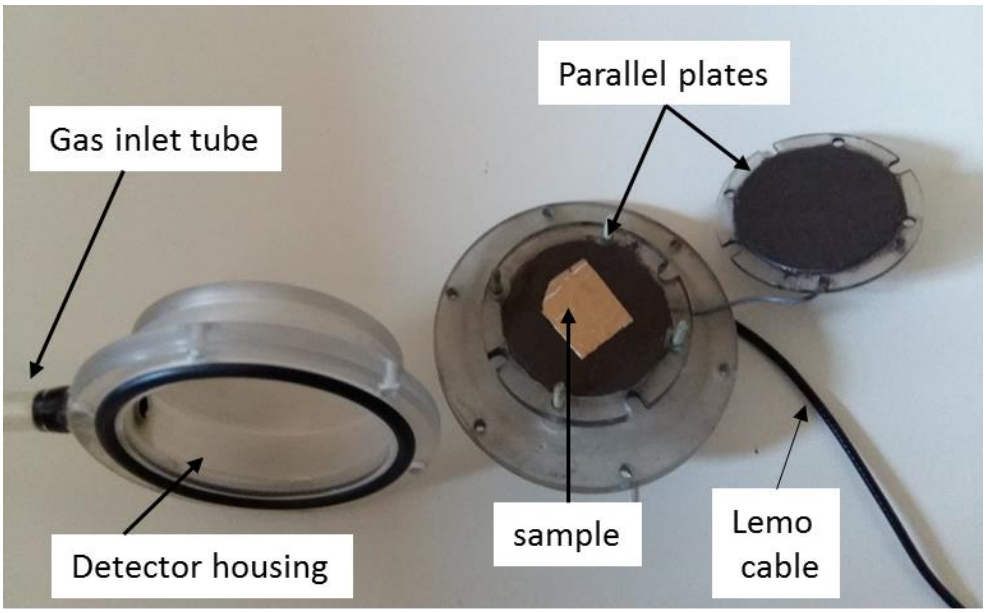

Figure 3.20: PPAD used for CEMS measurements of the sintered materials.

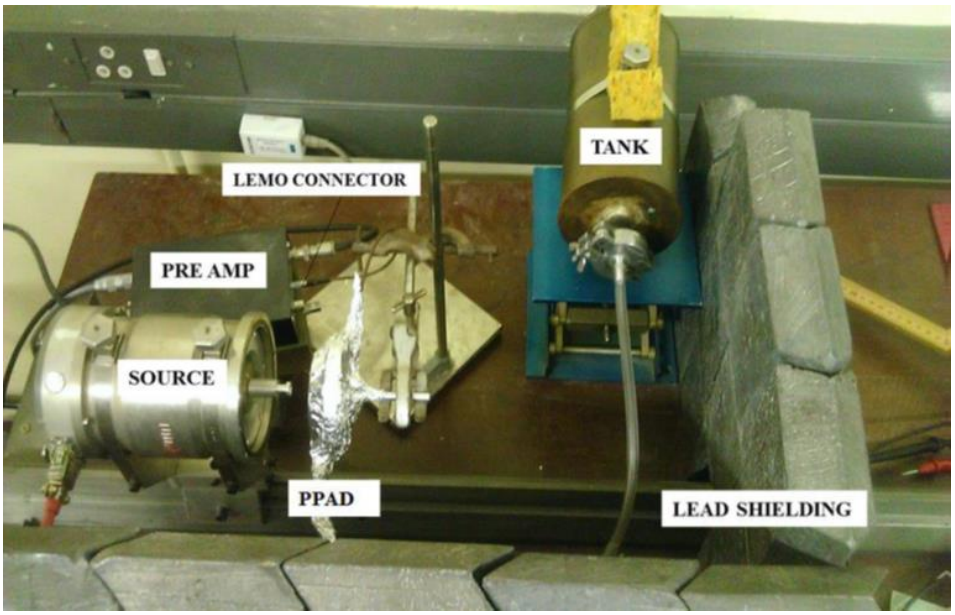

Figure 3.21: Set-up of the PPAD for CEMS.

3.4.8 Summary of techniques

The experimental techniques described in this chapter were utilised to manufacture and characterise the different carbide grades. A summary of the analytical techniques used for the milled powders and sintered materials are presented in Table 3.5.

In Table 3.5, "x" indicates the analytical techniques carried out for the different material grades. Note that the WC-Ni material does not contain Fe, hence there are no Mössbauer investigations for this material. The results derived from each technique are presented and discussed in Chapter 4.

Table 3.5: Summary of analytical techniques used for characterising the milled powders and sintered materials.

Material Grade	Material Condition	Density	Mag. Prop.	HV_{30}	OM / SEM/ EDS	XRD	Mössbauer	
							TMS	CEMS
1. WC-10Fe	Powder	-	-	-	-	x	x	-
	Sintered 1340 °C	x	x	x	x	x	-	x
	Sintered 1430 °C	x	x	x	x	x	-	x
	Sintered 1510 °C	x	x	x	x	x	-	x
2. WC-FeNi	Powder	-	-	-	-	x	x	-
	Sintered 1340 °C	x	x	x	x	x	-	x
	Sintered 1430 °C	x	x	x	x	x	-	x
	Sintered 1510 °C	x	x	x	x	x	-	x
3.WC-FeMn	Powder	-	-	-	-	x	x	-
	Sintered 1340 °C	x	x	x	x	x	-	x
	Sintered 1430 °C	x	x	x	x	x	-	x
	Sintered 1510 °C	x	x	x	x	x	-	x
4. WC-10Ni	Powder	-	-	-	-	x	-	-
	Sintered 1340 °C	x	x	x	x	x	-	-
	Sintered 1430 °C	x	x	x	x	x	-	-
	Sintered 1510 °C	x	x	x	x	x	-	-

Chapter 4

Results and Discussion

4.1 Introduction

The results obtained for the milled powders and sintered cemented carbides are presented and discussed in this chapter. The milled powders were assessed using X-ray diffraction and transmission Mössbauer spectroscopy techniques. The standard cemented carbide quality control tests are reported for the sintered materials. These tests include density, magnetic property (magnetic saturation and coercivity) and Vickers hardness measurements. The measurements provide an indication on the quality of powder preparation (milling) and sintering of the materials. The microstructures of the materials were assessed using optical microscopy and high resolution scanning electron microscopy (HRSEM). Phase identification (XRD results) of the powders and sintered materials are discussed, followed by the results of the ^{57}Fe Mössbauer investigations. All the findings, where applicable, are compared with results from literature for the different material compositions and the various sintering temperatures.

4.2 Sintered carbide quality control tests

4.2.1 Density measurements

The densities of sintered components were determined using a density balance and the results are presented in Table 4.1. The reported values are an average of three measurements, and the calculated theoretical densities are given for comparison against the measured values. An example of the theoretical density calculation is given in Chapter 3, Section 3.4.1.

Table 4.1: Density results for the various carbide grades at the different sintering temperatures.

Material grade	Density g/cm^3 1340°C	Density g/cm^3 1430°C	Density g/cm^3 1510°C	Theoretical Density g/cm^3
1. WC-10Fe	14.19 ± 0.01	14.19 ± 0.07	14.25 ± 0.03	14.27
2. WC-7Fe/3Ni	14.24 ± 0.03	14.26 ± 0.01	14.28 ± 0.01	14.37
3. WC-8.5Fe/1.5Mn	14.26 ± 0.07	14.43 ± 0.05	14.33 ± 0.05	14.24
4. WC-10Ni	13.58 ± 0.10	14.54 ± 0.01	14.53 ± 0.06	14.58

The ratio between the actual (measured) and the theoretical density gives the % densification of the material after sintering as expressed by

$$\%\text{Densification} = \frac{\text{theoretical density}}{\text{actual density}} \times 100\,. \qquad (4.1)$$

The % densification for the sintered materials at the different sintering temperatures are presented in Table 4.2.

Table 4.2: Variation of densification for the different sintering temperatures.

Material grade	%Densification 1340°C	%Densification 1430°C	%Densification 1510°C
1. WC-10Fe	99.40	99.42	99.78
2. WC-7Fe/3Ni	99.11	99.25	99.36
3. WC-8.5Fe/1.5Mn	100.14	101.30	100.59
4. WC-10Ni	93.07	99.69	99.60

The densification results show that the Fe/Mn binder grades have densifications higher than 100%. This is likely due to losses in manganese (Mn) during vacuum sintering resulting in changes to the material composition as indicated by EDS analysis which will be discussed later. Manganese volatilises during vacuum sintering and is usually sintered under an argon pressure of 8 mbar, and in a Mn vapour-saturated environment [1, 2]. The loss of Mn would result in compositional differences in the sintered components compared to the nominal starting composition, hence the theoretical density calculations would vary.

The WC-Ni material sintered at 1340 °C is only 93% dense which is indicative of the presence of open porosity. The temperature (1340 °C) is too low to achieve maximum density for a nickel binder [12], which is usually sintered at temperatures between 1450 °C and 1500 °C. The density values for the WC-Ni grades sintered at 1430 °C and 1510 °C are acceptable. Maximum densities of 99.36% and 99.78% are obtained for the WC-Fe/Ni and WC-Fe grades, respectively, at the highest sintering temperature of 1510 °C. These values are similar to the results obtained by Chang *et al*. [17], who achieved a maximum density of 99.68% for a WC-15FeNi alloy vacuum sintered at 1400 °C. The sintering temperature of 1400 °C would be

consistent for sintering a higher binder content (15 wt%) carbide compared to the higher temperatures used in the current study for 10 wt% binder contents.

4.2.2 Magnetic Saturation

Magnetic saturation data provide information on the stoichiometry of the sintered carbides. In cemented carbides, the stoichiometry [49] is determined by the carbon level which affects the dissolved tungsten in the metal binder as discussed in Chapters 1 and 3. The magnetic saturation results for the sintered materials are shown in Table 4.3. The different binder grades are compared individually for the different temperatures as the magnetic saturation limits differ for each metal, and the solubility of tungsten in each metal varies as well.

Table 4.3: Magnetic saturation results for the sintered carbides.

Material grade	Mag. Sat. Gauss.cm^3/g 1340°C	Mag. Sat. Gauss.cm^3/g 1430°C	Mag. Sat. Gauss.cm^3/g 1510°C
1. WC-10Fe	19.5 ± 0.10	19.1 ± 0.11	17.1 ± 0.05
2. WC-7Fe/3Ni	11.7 ± 0.07	13.6 ± 0.05	11.9 ± 0.45
3. WC-8.5Fe/1.5Mn	15.1 ± 0.05	15.9 ± 0.20	15.3 ± 0.05
4. WC-10Ni	4.0 ± 0.20	4.4 ± 0.05	4.5 ± 0.05

The results are shown graphically in Figure 4.1. The magnetic saturation values for the WC-10Fe materials decrease with increasing temperature, suggesting possible increasing tungsten levels in the Fe binder. This is similar to WC-Co alloys where the magnetic saturation decreases linearly with increasing tungsten in solution [49]. The highest magnetic saturation values for the WC-FeNi and WC-FeMn materials are obtained at 1430 °C, indicating that this could potentially be the optimum sintering temperature for these binder alloys. The WC-Ni grade has a maximum magnetic saturation value of 4.5 Gauss.cm^3/g at 1510 °C, which is consistent with the literature [12] where Ni binders are sintered at 1500 °C.

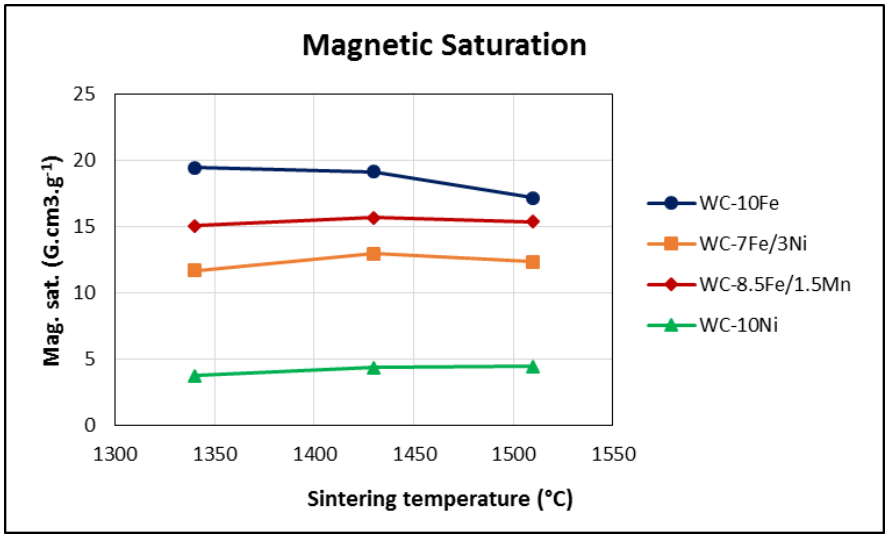

Figure 4.1: Graph of magnetic saturation results for the different sintering temperatures.

4.2.3 Coercivity (H_C)

As the same starting WC grain size (2–4 µm) was used with a constant binder content (10 wt%) for all the grades, the coercivity values provide information on the sintering quality. The structural parameters that would influence the H_C results are WC grain size distribution, binder pool size and structural defects (porosity, inclusions and η-phase). The coercivity results are shown in Table 4.4. The H_C values are an average of the positive and negative fields for the sintered samples.

Table 4.4: Coercivity (H_C) results for the sintered samples.

Material grade	H_C (Oe) 1340 °C	H_C (Oe) 1430 °C	H_C (Oe) 1510 °C
1. WC-10Fe	80 ± 3	86 ± 2	69 ± 2
2. WC-7Fe/3Ni	40 ± 4	49 ± 1	45 ± 5
3. WC-8.5Fe/1.5Mn	108 ± 1	77 ± 2	78 ± 1
4. WC-10Ni	47 ± 12	38 ± 4	37 ± 1

The H_C results are also shown graphically in Figure 4.2. In general, there is a distinct difference in H_C values between the Ni-binder materials (WC-Ni and WC-FeNi) and the binders without Ni (WC-Fe and WC-FeMn). The materials containing Ni binders have much lower coercivity values. This variation is explained by the low Curie temperature of Ni (378 °C) compared to Co which is 1123 °C [12]. The Curie

temperature of Ni binders is further suppressed to 200 °C by tungsten in solution which result in a decrease in magnetic saturation. Daoush *et al*. [61] found similar trends for Co and Ni binders in (WTi) C materials. These authors reported H_C values of 74 Oe and 38 Oe for 10 wt% Co and Ni binders, respectively, which are similar to the results obtained in this work.

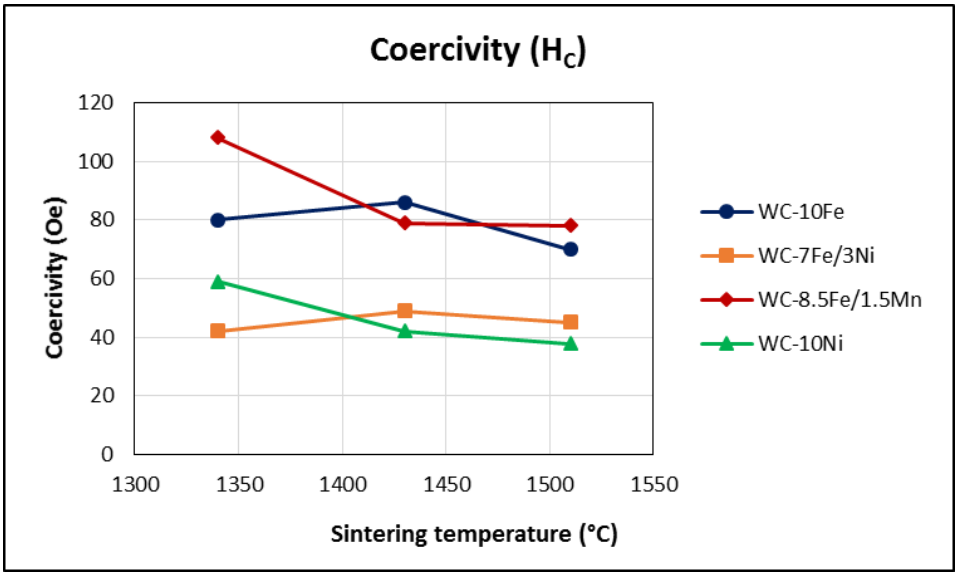

Figure 4.2: Graph of Coercivity (H_C) results for the sintered carbide grades.

At the lowest sintering temperature of 1340 °C, there are anomalies in the H_C results for the WC-FeMn and WC-Ni grades. The higher than expected H_C values obtained for these grades are due to structural imperfections in the materials as verified by microstructural examination given in Sections 4.3.1 and 4.3.2. The unusually high H_C value for the WC-FeMn grade sintered at 1340 °C is due to the presence of η-phase in the material. The coercive field strength [62] is affected by obstacles that impede the movement of Bloch walls between the magnetic domains. In cemented carbides, the WC grains and mixed carbide phases including η-phase are regarded as these obstacles. The high H_C value for the WC-Ni grade sintered at 1340 °C can be attributed to the presence of porosity in this material as indicated by the density results (Section 4.2.1) and confirmed by the microstructural observations (Section

4.3.2). The other grades (WC-Fe and WC-FeNi) sintered at 1340 °C have slightly lower H_C values than at 1430 °C which is likely due to the large binder pools present in the structure which will be discussed in Section 4.3.2.

In the WC-10Fe grade, the highest H_C value (86 Oe) is obtained at 1430 °C, and a significant decrease in H_C is observed for the highest sintering temperature of 1510 °C, which is indicative of WC grain growth in the structure at the higher temperature. Reports in the literature [4] show that coercivity decreases with increasing WC grain size. The WC-FeNi and WC-Ni grades also show a small decrease in H_C as the temperature is increased from 1430 °C to 1510 °C, resulting from WC grain coarsening.

4.2.4 Hardness

Hardness measurement [4] is a critical and sensitive quality control parameter in the production of tungsten carbide hardmetals. The hardness property in hardmetals is affected by the WC grain size, porosity and structural variations in a material having a constant composition.

Vickers hardness (HV) measurements were determined on the polished sections of the sintered materials using a 30 kg load as per the ISO3878 procedure [53]. The hardness results are summarised in Table 4.5. A reference cobalt binder grade, WC-10Co, was measured for comparison against alternate binder grades. The cobalt grade was sintered 1430 °C, which is the optimum sintering temperature for this grade. A comparative hardness graph for the various materials is shown in Figure 4.3.

Table 4.5: Vickers hardness results for the various binder grades.

Material grade	HV_{30} 1340 °C	HV_{30} 1430 °C	HV_{30} 1510 °C
1. WC-10Fe	1282 ± 14	1311 ± 9	1320 ± 6
2. WC-7Fe/3Ni	1230 ± 13	1250 ± 4	1139 ± 14
3. WC-8.5Fe/1.5Mn	1525 ± 4	1337 ± 9	1257 ± 5
4. WC-10Ni	534 ± 20	1132 ± 4	1132 ± 4
5. WC-10Co	-	1250 ± 4	-

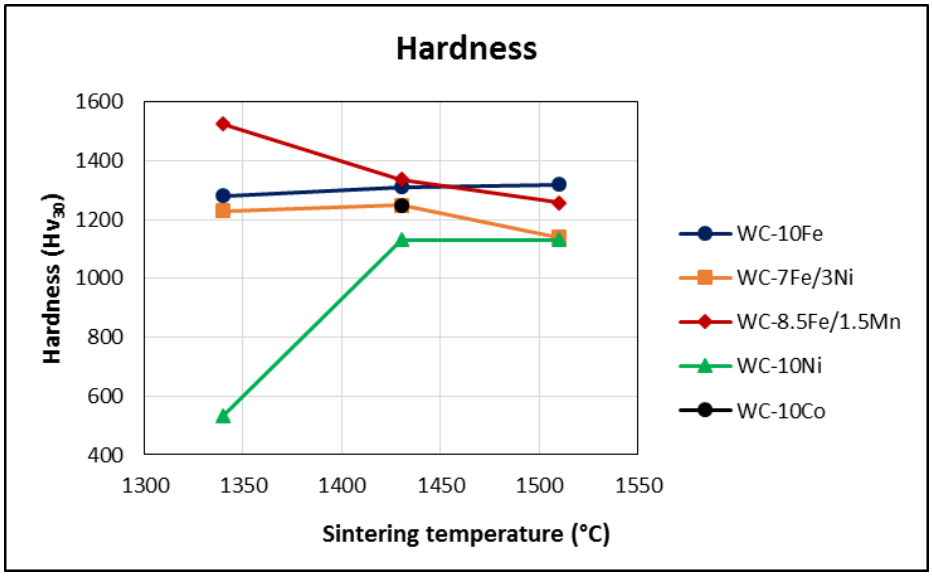

Figure 4.3: Graph of hardness (HV30) for the various binder carbide grades.

The hardness results for the materials sintered at the lowest temperature of 1340 °C show anomalies for the WC-FeMn and WC-Ni grades. This is due to the same microstructural defects responsible for the anomalies in the coercivity data for these grades. The unusually high hardness value for WC-FeMn grade is due to the presence of the brittle η-phase in the material, whilst the presence of porosity in the WC-Ni grade would result in the very low hardness value as the material is not fully dense.

The hardness values for the WC-Fe grade is consistent throughout the temperature range. Generally, the WC-10Fe grade has the highest hardness values compared to the other metal binder grades, including the reference WC-Co material. Similar trends were shown in a review of WC-based hardmetals bonded with Fe alloys by Ojo-Kupolusi *et al*. [11]. Vickers hardness values of 1814, 1776 and 1750 are reported for WC-10Fe, WC-10Co and WC-10Ni, respectively with an average WC grain size of 0.45 µm. The higher hardness values that were reported are due to the fine WC grain size in these materials compared to 2-4 µm grain size used for this work.

The WC-Fe/Ni grade has an optimum hardness at 1430 °C, followed by a significant decrease at the highest temperature of 1510 °C. This suggests slight WC grain coarsening. The hardness value of the WC-Fe/Ni grade (1250 HV_{30}) is similar to the reference WC-10Co grade at 1430 °C. This is consistent with work conducted by Prakash *et al*. [63] where hardness values of 980 HV for WC-16Fe4Ni, and 1000 HV for WC-20Co were reported. The lower hardness values of ~1000 HV compared to the current study (1250 HV), is due to the higher binder content used (20 wt%). Chang *et al*. [17], measured Rockwell hardness (HRA) on WC-15Fe/Ni (50/50) and WC-15Co grades with a WC grain size of 1-2 µm. A slightly higher hardness value of 85.3 HRA (920 HV) was reported for the WC-15Fe/Ni grade, compared to 84.3 HRA (860 HV) for the WC-15Co grade. Gonzalez *et al*. [18], performed studies on WC-10Fe/Ni (90/10) alloys with various WC grain sizes and reported hardness values (HV_{30}) of 1603, 1380 and 1200 for 1, 4 and 6 µm, respectively. The higher ratio of Fe in the 90/10 Fe/Ni binders would result in higher hardness values compared to the current work where the Fe/Ni ratio is 70/30. Results in literature suggest that WC-Fe/Ni hardmetals have similar or slightly higher hardness values compared to WC-Co alloys.

The hardness of the WC-FeMn grade at 1430 °C decreases from 1337 HV_{30} to 1257 HV_{30} as the sintering temperature is increased to 1510 °C. This is likely due to WC grain coarsening at 1510 °C. Hanyaloglu *et al*. [1], conducted hardness measurements on WC-15FeMn and WC-20FeMn grades having a WC grain size of 1-3 µm and reported improved hardness values of 1529 HV_{50} and 1429 HV_{50}, respectively, compared to WC-Co alloys. These results were found to be higher than literature values reported for WC-15Co and WC-20Co, which are 1130 HV and 800 HV, respectively, for a similar grain size.

The WC-10Ni grade has the lowest hardness compared to the other binder grades. An optimum hardness of 1132 HV_{30} is achieved at sintering temperatures between 1430 and 1510 °C. In general, WC-Ni alloys have appreciably lower hardness and lower strength than WC-Co alloys for similar compositions [64]. A hardness value of 87.5 HRA (1150 HV) was reported by Miranda [65] for a WC-10Ni hardmetal

having a grain size of 3 – 4 µm. This is consistent with the value obtained in this work (1132 HV_{30}), which has a similar composition and grain size.

4.3 Microstructural Examination

4.3.1 Optical microscopy

The macro structures were examined using a light microscope on the polished section of the samples at magnifications ranging from 100 to 500x to access any porosity present in the materials. The optical images at 500x magnification are shown in Figures 4.4 to 4.7.

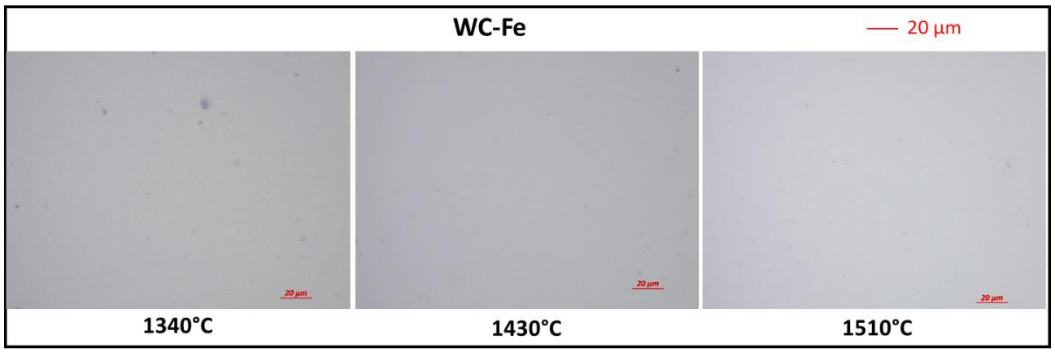

Figure 4.4: Optical micrographs of the WC-Fe sintered structures at 500x.

There is no porosity observed in the WC-Fe and WC-Fe/Ni grades for all the temperature ranges (Figures 4.4 and 4.5). The features observed in the sample sintered at 1510 °C appears to be Fe-Ni binder lakes surrounding large WC grains associated with abnormal WC grain growth occurring at the highest sintering temperature (Figure 4.5). This is only observed in isolated areas of the structure.

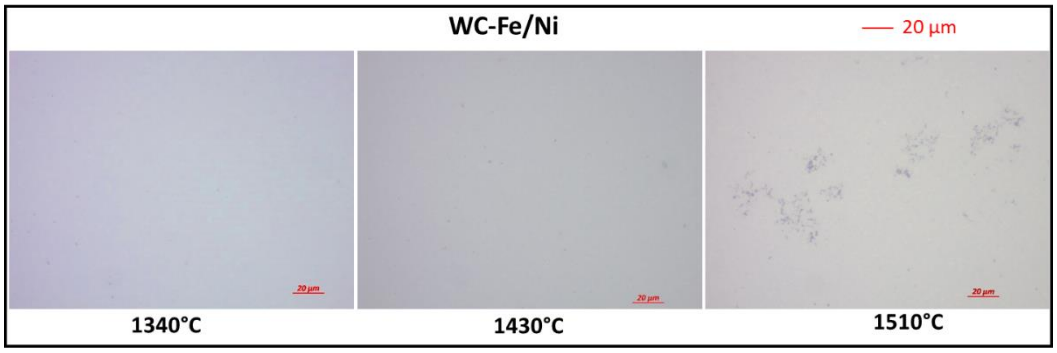

Figure 4.5: Optical micrographs of the WC-Fe/Ni sintered structures at 500x.

A combination of porosity and a darker phase, possibly η-phase, is observed for the WC-Fe/Mn grade at the lowest sintering temperature of 1340 °C as shown in Figure 4.6. The microstructure at 1430 °C appears to be homogeneous, and at the highest sintering temperature (1510 °C), slight in-homogeneities were observed.

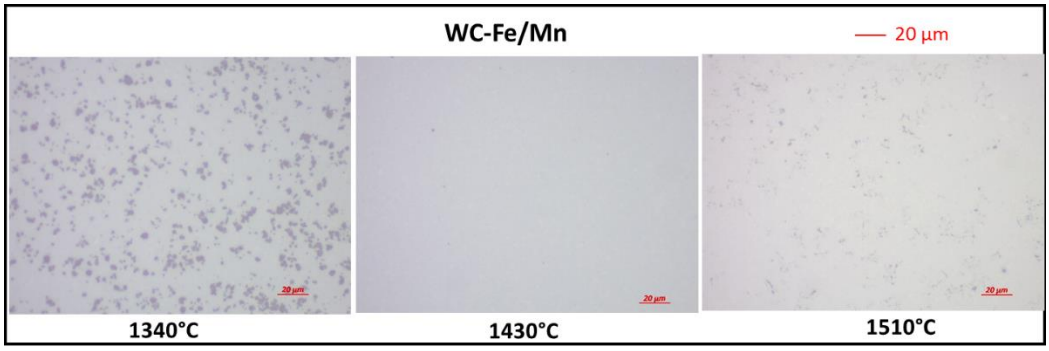

Figure 4.6: Optical micrographs of the WC-Fe/Mn sintered structures at 500x.

A high volume of open porosity is observed for the WC-Ni grade at the lowest sintering of 1340 °C (Figure 4.7), which is consistent with low densification for this temperature. The sample sintered at the higher temperature ranges do not contain porosity.

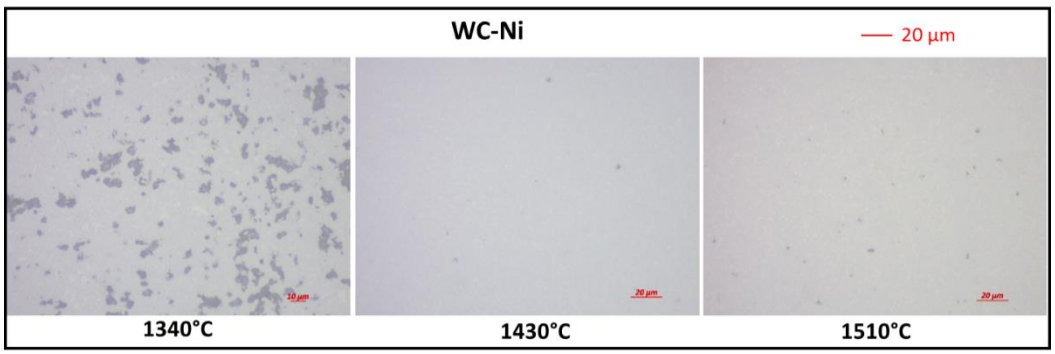

Figure 4.7: Optical micrographs of the WC-Ni sintered structures at 500x.

The samples were lightly etched for 30 seconds in Murakami's reagent and re-examined to determine the presence of any minor sub-stoichiometric phases. The etching process did not reveal any new phases other than the structures observed in the un-etched samples.

4.3.2 Scanning Electron Microscopy

A more detailed examination of the microstructures was carried out using a High Resolution Scanning Electron Microscope (HRSEM). Energy Dispersive X-ray analysis (EDS) was employed to give an indication of the elemental ratios of the material compositions.

The microstructures of the various grades are typical of cemented carbide structures. The grey angular and blocky grains are the WC grains, and the darker (black) phase surrounding or cementing the WC grains is the binder matrix as shown in Figure 4.8 for a WC-Fe sample. The microstructural evolution of the different carbide grades over the various sintering temperatures are given in Figure 4.9 at 5000x magnification using backscattered imaging (BSE).

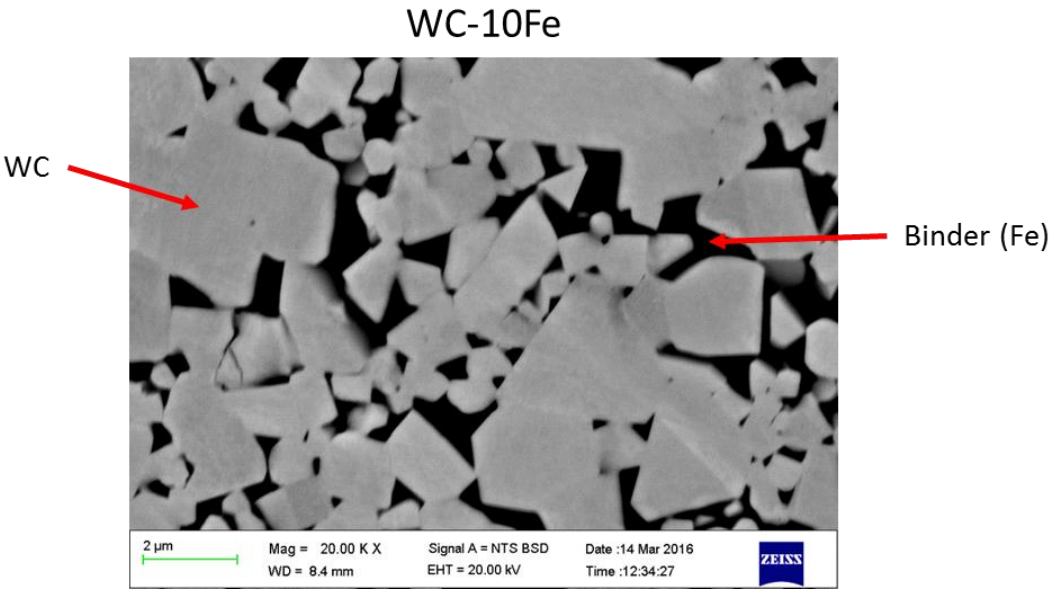

Figure 4.8: Typical microstructure of a sintered sample (WC-Fe) at 20000x magnification.

The microstructures of the WC-Fe alloys sintered at the different temperatures are shown at 5 000x magnification in Figure 4.9. At the lowest sintering temperature of 1340 °C, the microstructure of the WC-Fe grade has binder pools, 2 to 5 µm in size, and clustering of fine WC grains as shown in Figures 4.9 and 4.10. A more homogeneous structure is observed as the temperatures increases to 1430 °C (Figure 4.9), both with the distribution of the metal binder and WC grain size. At the highest sintering temperature (1510 °C), there is a general coarsening of the WC grain size due to the dissolution of the fine WC particles into the metal binder, and re-precipitation on existing WC grains through the process of Oswald's ripening [66]. The evolution of the microstructures (homogeneity and WC grain morphology) with increasing temperature are shown at different magnifications (2000 x and 10000 x) in Appendix A. There is no abnormal grain growth in the materials sintered at the highest temperature (1510 °C), rather a uniform coarsening of the WC grain structure.

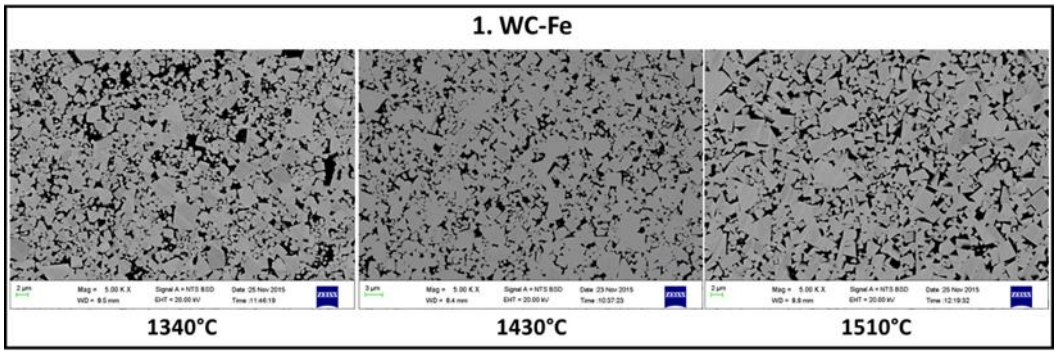

Figure 4.10: SEM micrographs of the WC-Fe sintered structures at 5000x.

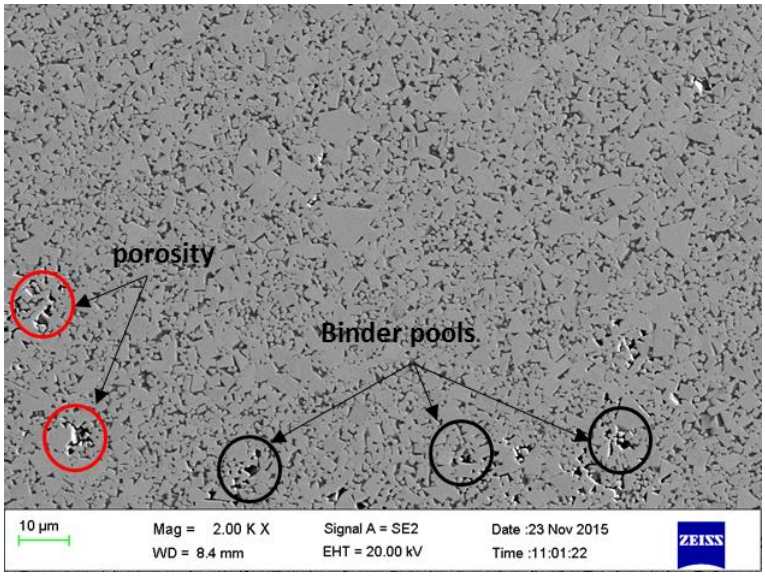

Figure 4.9: Secondary electron image of the WC-Fe sintered at 1340 °C showing some of the porosity (red circles) and binder pools (black circles) at 2000x.

The microstructures of the WC-Fe/Ni materials show similar trends to the WC-Fe materials for the different temperatures. The size of the metal binder pools are however larger, up to 10 µm in size, than those observed in the WC-Fe materials, with slightly more WC grain coarsening at 1510 °C (Figure 4.11). The distribution of the phases (WC and metal binder) appears to be more homogeneous at the highest temperature.

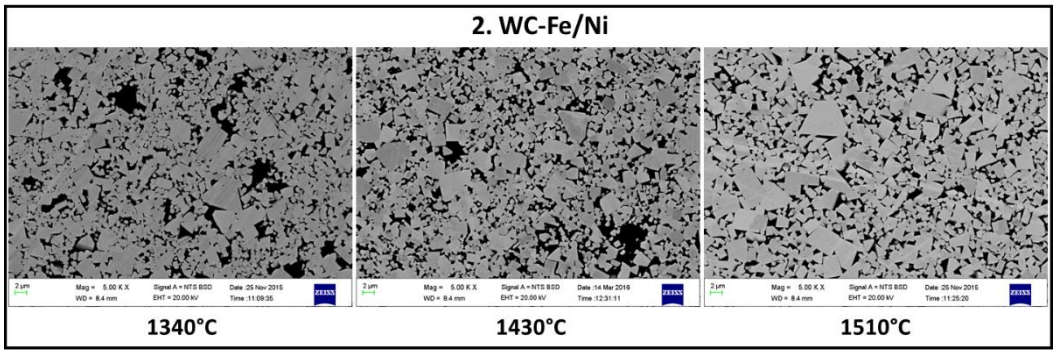

Figure 4.11: SEM micrographs of the WC-Fe/Ni sintered structures at 5000x.

The WC-Fe/Mn microstructures at the different sintering temperatures are shown in Figure 4.12. The microstructure at 1340 °C contains a combination of metal binder pools and porosity (Figure 4.13), as well as a possible sub-stoichiometric phase (η-phase) shown in Figure 4.14. The microstructures are more homogeneously distributed at the higher sintering temperature of 1430 °C (Figure 4.12). The presence of η-phase in the WC-Fe/Mn material sintered at 1340 °C could be the reason for the very high coercivity and hardness values obtained for this grade. The η-phase is a hard, brittle phase [4] and is usually associated with carbon deficiency in the material. The morphology of the WC grains is more rounded which is usually associated with the presence of η-phase as shown in Figure 4.14.

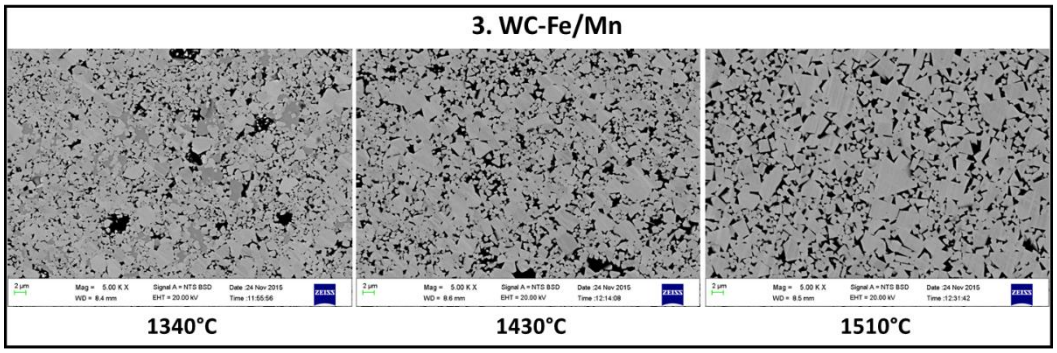

Figure 4.12: SEM micrographs of the WC-Fe/Mn sintered structures at 5000x.

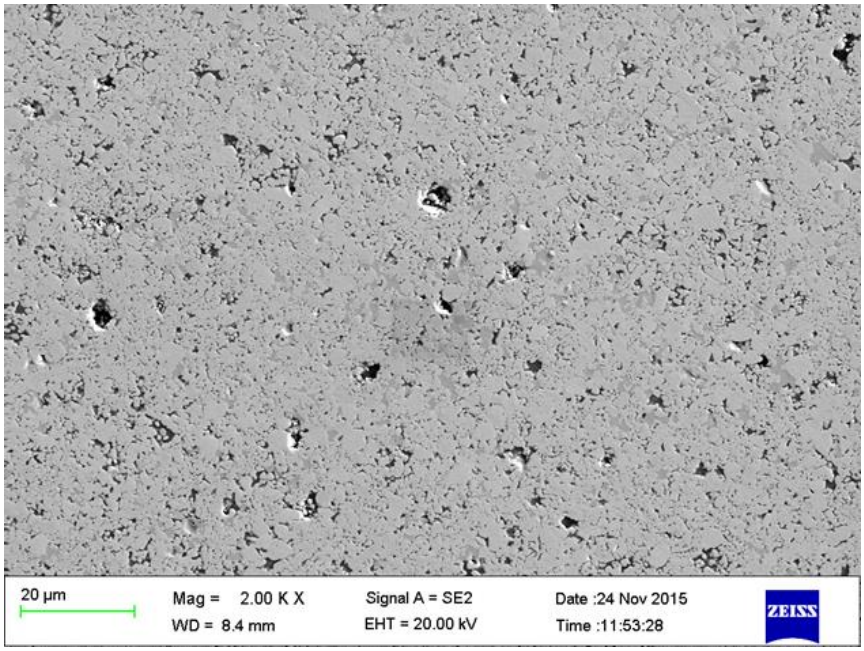

Figure 4.13: Secondary electron image of the WC-Fe/Mn sintered at 1340 °C showing porosity and binder pools at 2000x.

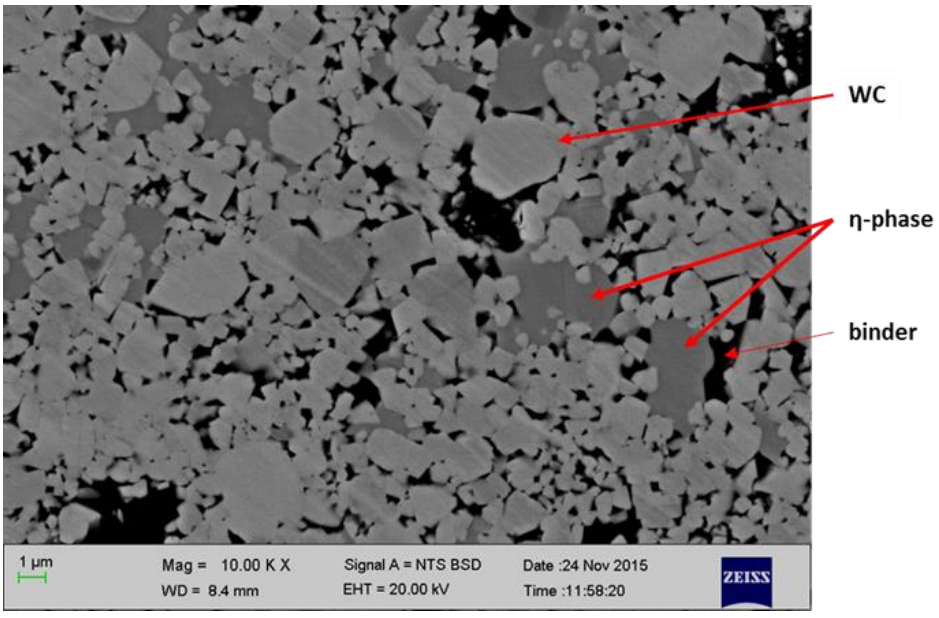

Figure 4.14: Microstructure of the WC-FeMn sample sintered at 1340 °C showing the presence of η-phase (darker grey phase) in a matrix of WC (light grey phase) and metal binder (dark phase) at 10000x.

As the carbon levels were consistent in all the materials, and the different grades were sintered in the same furnace run at 1350 °C, the likely reason for the presence of η-phase in the WC-Fe/Mn grade is given by Shubert *et al*. [2] as oxidation of the FeMn binder in the pressed powders. The authors [2] found η-phase in the WC-FeMn alloys when the pressed powders were sintered a few days later. In this work, the low temperature (1350 °C) sintering run only occurred 3 weeks after pressing the powders as a full furnace load had to be built up for the production run. The typical sintering temperatures used at Pilot Tools for production is 1430 °C and 1510 °C, so the WC-FeMn grades sintered at these temperatures were not affected. The increased oxidation of the WC-FeMn pressed powders sintered at 1340 °C would result in a carbon deficiency during sintering leading to the formation of η-phase.

The WC-Ni sample sintered at the lowest temperature of 1340 °C is not fully dense and contains a high volume of open porosity as shown in Figure 4.15. The samples sintered at the higher temperatures (1430 °C and 1510 °C) are fully dense with uniform microstructures as shown in Figure 4.16.

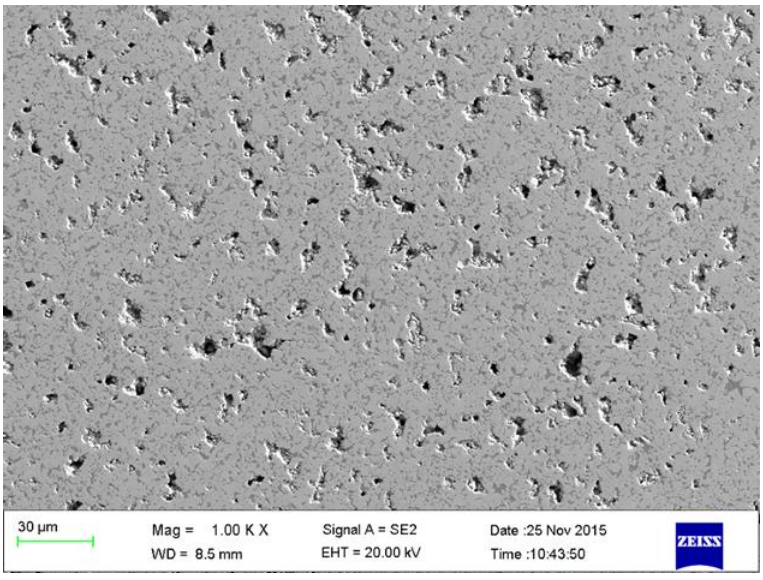

Figure 4.15: Secondary electron image of the WC-Ni sintered at 1340 °C showing the presence of porosity in the sample at 1000x.

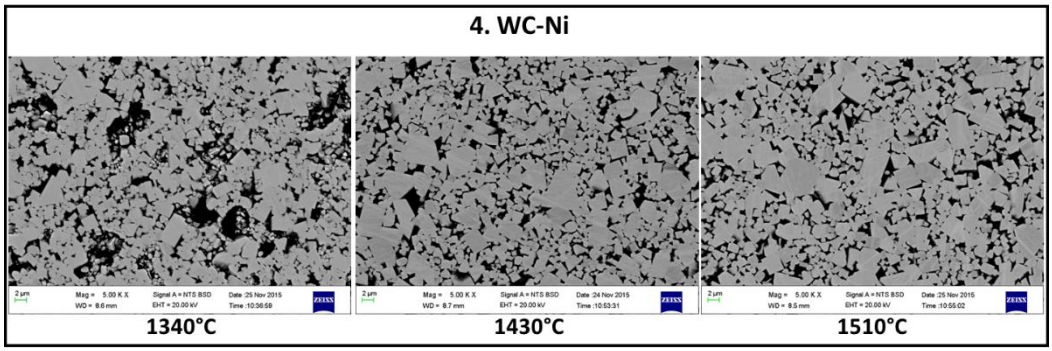

Figure 4.16: SEM micrographs of the WC-Ni sintered structures at 5000x.

The elemental compositions of the samples were determined using EDS to ascertain the presence of contaminants in the sintered materials. Analysis was performed over an area of 500 x 600 µm on each sample, and the semi-quantitative analysis results are presented in Table 4.6.

Table 4.6: EDS results showing the elemental compositions for the various grades.

Material Grade	Temp. °C	W wt%	C wt%	Fe wt%	Ni wt%	Mn wt%	Other wt%
1. WC-10Fe	1340	82.4	7.0	10.6	-	-	-
	1430	82.4	7.8	9.8	-	-	-
	1510	82.8	7.5	9.1	-	-	0.6 Co
2.WC-7Fe/3Ni	1340	81.5	8.1	7.4	3.1	-	-
	1430	82.2	7.0	7.1	3.2	-	0.5 Co
	1510						
3.WC-8.5Fe/1.5Mn	1340	85.1	6.9	7.4	-	0.6	-
	1430	84.1	7.1	8.7	-	0.1	-
	1510	84.0	8.3	6.9	-	0.2	0.6 Co
4. WC-10Ni	1340	79.3	8.8	-	10.8	-	1.1 O_2
	1430	83.0	7.0	-	10.0	-	-
	1510	82.0	7.5	0.5	9.3	-	0.7 Co

Generally, the EDS results reflect the nominal metal binder compositions for the various grades, except for the WC-Fe/Mn grades, where the Mn appears to have volatilised during sintering resulting in much lower concentrations than the nominal composition. The vapour pressure of manganese [1, 2] is very high at temperatures above 1000 °C and volatilises during the vacuum sintering of WC-Fe/Mn

hardmetals. Manganese losses can be minimised by sintering in a manganese vapour environment.

The nominal composition for WC-FeMn grade contains 1.5 wt% Mn, and only 0.6 wt% Mn as detected by EDS in the material sintered at 1340 °C. The materials sintered at the higher sintering temperatures contain 0.1 to 0.2 wt% Mn. Evidence of Co contamination are observed in some materials which is probably due to cross-contamination during milling and/or sieving procedures. The presence of oxygen in the WC-Ni sample sintered at the low temperature of 1340 °C can be attributed to contamination due to the high levels of porosity in the material.

4.4 X-ray Diffraction (XRD)

The phase compositions of the milled powders and sintered materials were determined using XRD analysis. The XRD results are summarised in Table 4.7 and the corresponding XRD patterns are shown in Figures 4.17 to 4.20. The results for the milled powders reflect the nominal compositions of the different grades, which are WC (hcp) and the metal binder phase. Both metal binder constituents are detected in the mixed binder grades which are α-Fe and γ-Ni in the WC-FeNi grade and, α-Fe and α-Mn in the WC-FeMn grade. The mixed metal binders form solid solutions after sintering which are Fe_3Ni_2 and $Fe_{0.95}Mn_{0.05}$ for the WC-FeNi and WC-FeMn grades, respectively.

Evidence of a sub-stoichiometric η-phase, Fe_2W_2C, is observed in the WC-Fe/Mn grade sintered at 1340 °C as shown in Table 4.7 and Figure 4.19. This confirms the microstructural observations (Section 4.3), and explains the high hardness and coercivity values obtained for this sample (Sections 4.2.3 and 4.2.4). The WC-Fe/Mn grades sintered at 1430 °C and 1510 °C are stoichiometric, consisting of WC and the liquid binder phase. Similar phase observations for WC-Fe and WC-Fe/Ni alloys were found by Fernandes *et al*. [67], where the binder phases were identified as α-Fe and γ-FeNi, respectively.

Table 4.7: Summary of the phase compositions determined using XRD for the various grades.

Material Grade	Material Condition	Phases
1. WC-10Fe	Powder	WC ; α-Fe
	Sintered 1340 °C	WC ; α-Fe
	Sintered 1430 °C	WC ; α-Fe
	Sintered 1510 °C	WC ; α-Fe
2. WC-7Fe/3Ni	Powder	WC ; α-Fe ; Ni
	Sintered 1340 °C	WC ; Fe_3Ni_2
	Sintered 1430 °C	WC ; Fe_3Ni_2
	Sintered 1510 °C	WC ; Fe_3Ni_2
3.WC-8.5Fe/1.5Mn	Powder	WC ; α-Fe ; Mn
	Sintered 1340 °C	WC ; $Fe_{0.95}Mn_{0.05}$; Fe_2W_2C
	Sintered 1430 °C	WC ; $Fe_{0.95}Mn_{0.05}$
	Sintered 1510 °C	WC ; $Fe_{0.95}Mn_{0.05}$
4. WC-10Ni	Powder	WC ; Ni
	Sintered 1340 °C	WC ; Ni
	Sintered 1430 °C	WC ; Ni
	Sintered 1510 °C	WC ; Ni

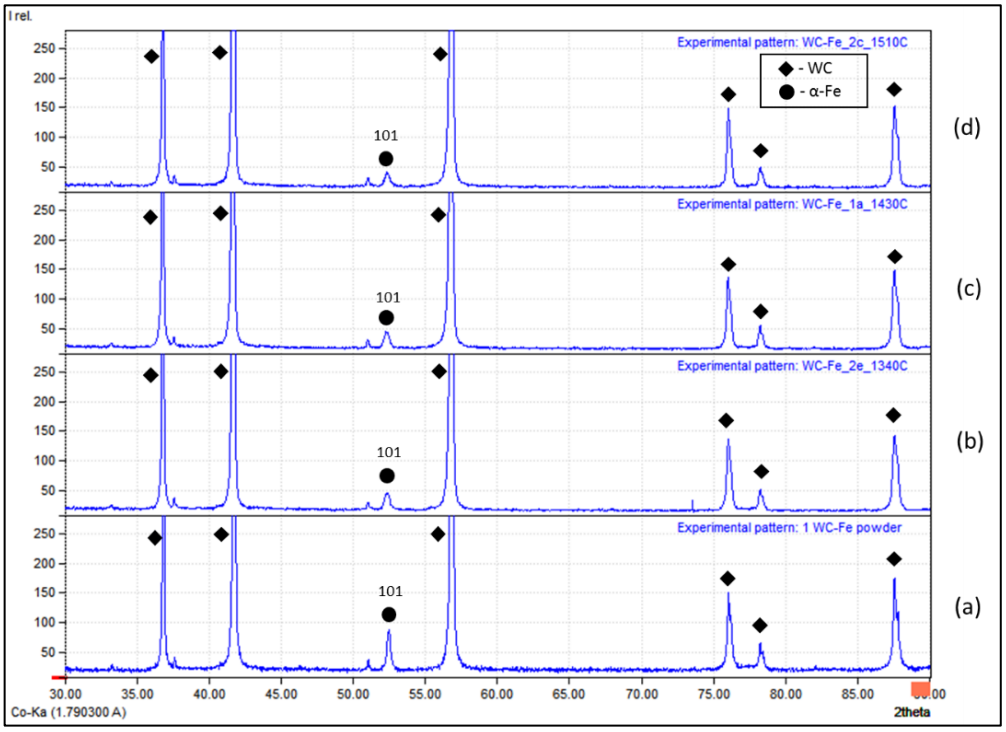

Figure 4.17: XRD patterns for the WC-10Fe milled powder (a), and sintered materials, (b) 1350 °C, (c) 1430 °C and (d) 1510 °C.

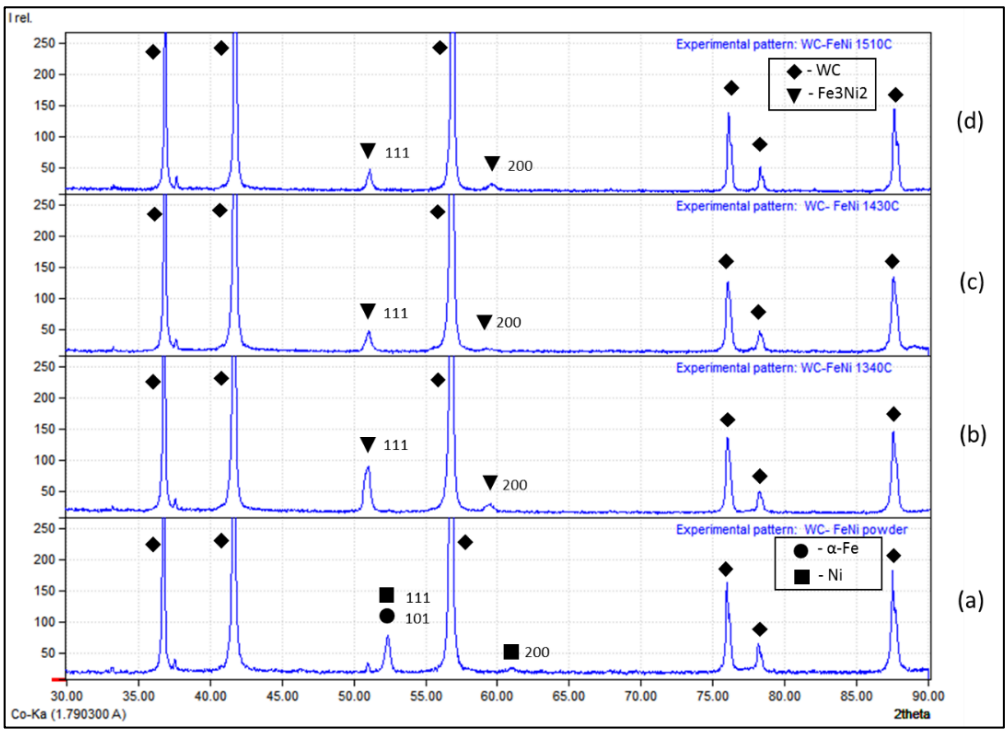

Figure 4.19: XRD patterns for the WC-10Fe/Ni milled powder (a), and sintered materials, (b) 1350 °C, (c) 1430 °C and (d) 1510 °C.

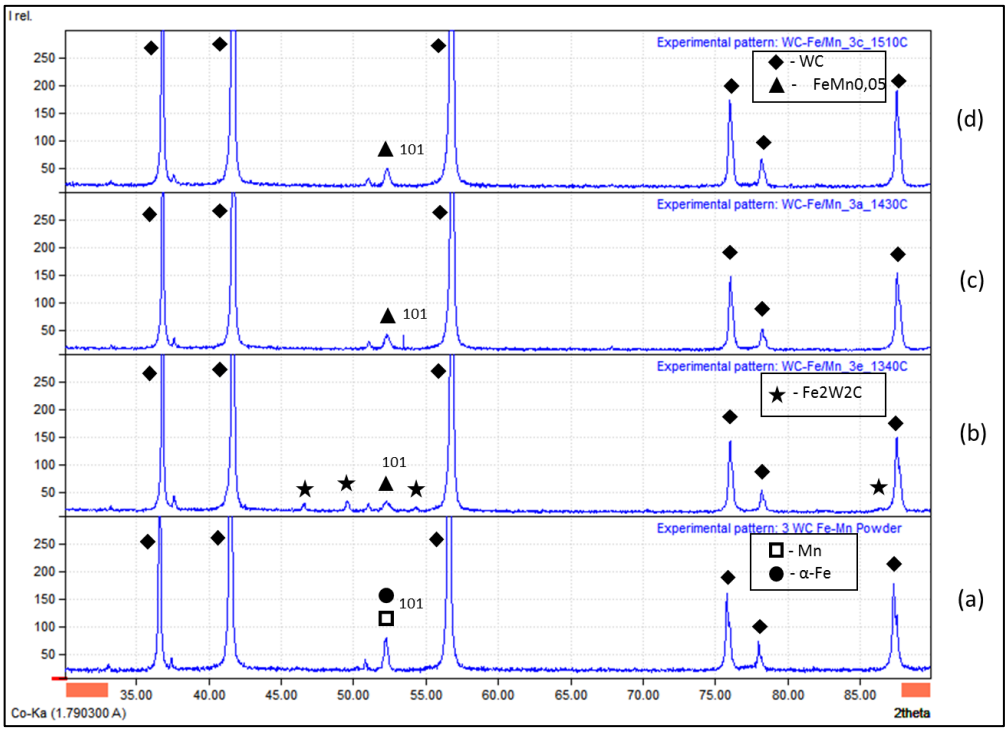

Figure 4.18: XRD patterns for the WC-10Fe/Mn milled powder (a), and sintered materials, (b) 1350 °C, (c) 1430 °C and (d) 1510 °C.

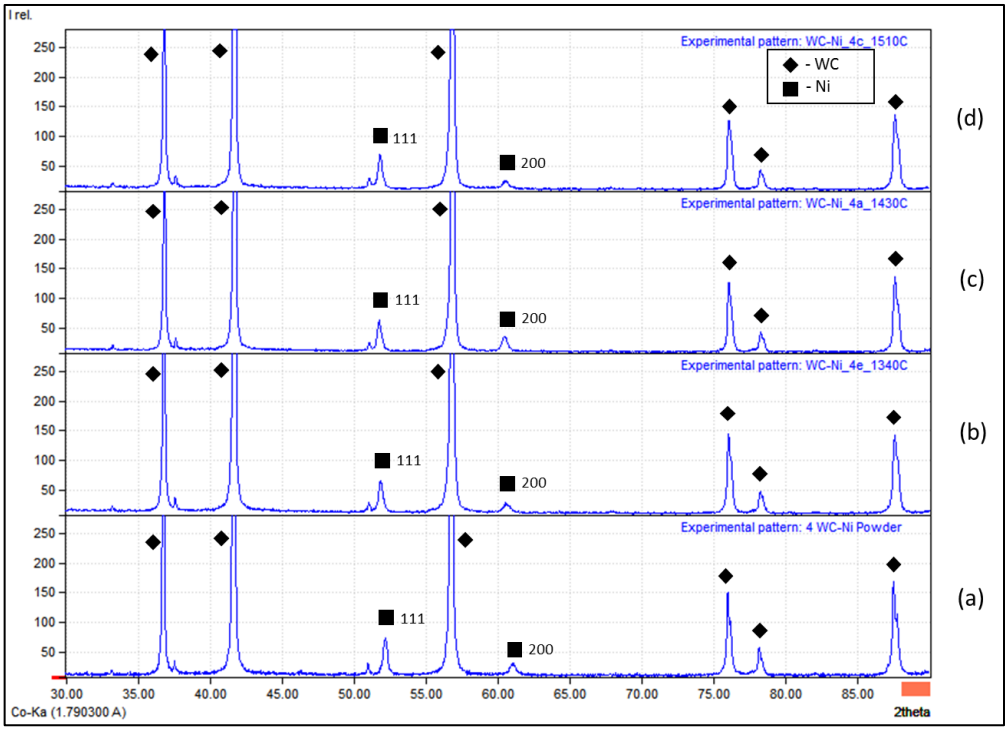

Figure 4.20: XRD patterns for the WC-10Ni milled powder (a), and sintered materials, (b) 1350 °C, (c) 1430 °C and (d) 1510 °C.

Some minor unidentified peaks are observed in all the XRD patterns at 37° and 51.9° 2Θ angles. These minor peaks appear to be part of the WC phase as the same peaks were detected in the starting WC powder as shown in Figure 4.21. As these unidentified peaks are still present in the sintered materials, it is unlikely to be the normal contaminants (Co, Fe, Zn, Si, Al, Na, K, O, Cr, or Ti) found in WC powders at ppm levels. These contaminants would alloy with the metal binder during sintering, and not be present as a single component thereafter. The supplier specification for WC powder is given as 99.9% (Table 3.1). It could be therefore related to the structure of the WC powder.

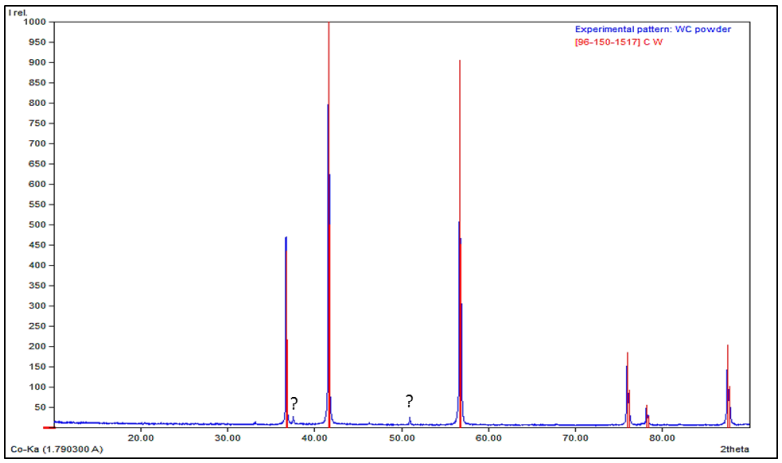

Figure 4.21: XRD pattern of WC starting powder.

4.5 Mössbauer Spectroscopy

4.5.1 Calibration of ^{57}Fe Mössbauer spectra

Calibration of the Mössbauer spectra was carried out using α-Fe foil having a purity of 99.99% and a thickness of 12 µm in order to determine the zero velocity and calibration constant in the Mössbauer spectrum [68]. This is achieved by determining the constants *C* and *z* so that

$$v_i = C\,(i - z) \tag{4.2}$$

where C is the calibration constant, z is the zero velocity and i is the channel number. A reasonable spectrum is obtained for the Fe foil after a few hours. The spectrum is recorded twice in the 512 channels of the MCA as the source velocity sweeps through the positive and negative velocity. The total set of data [57] of the Mössbauer spectrum has a symmetry point around the middle. Folding the data around the symmetry point reduces the number of channels in half (256 channels), thus improving the statistics of the measurement. A six-line pattern is obtained for α-Fe, with the peak positions as supplied by the Mössbauer Effect Data Center (MEDC) are given as -5.31, -3.08, -0.84, 0.84, 3.08 and 5.31 mm/s as shown in Figure 4.22.

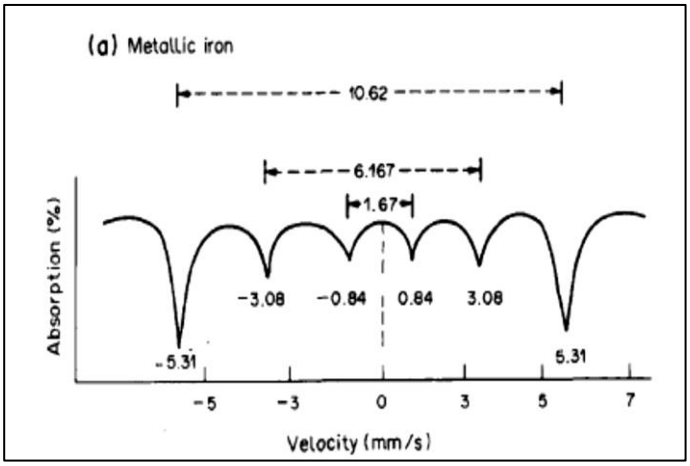

Figure 4.22: Mössbauer spectrum of α-Fe showing the peak positions of the six lines [70].

A ^{57}Fe Mössbauer calibration spectrum with good statistics is generated after ~3 hours in transmission mode (TMS), and about 24 hours using the CEMS technique. The data analysis and fitting of the spectra is carried out using Vinda software developed by H.P. Gunnlaugsson [69]. Vinda is an Add-In for Microsoft Excel and contains a summary of various models to give reasonable results. A summary of the fitting procedure and data analysis is given in Appendix B.

The calibration spectrum for the Fe foil using TMS is shown in Figure 4.23, and the CEMS calibration is shown in Figure 4.24. In the transmission mode, the Zeeman splitting has a 3:2:1:1:2:3 peak ratio, whilst the backscatter mode has a 3:4:1:1:4:3 peak ratio. The data obtained for the Fe foil is fitted to a theoretical spectrum of α-Fe having a magnetic hyperfine field (B_{hf}) of 32.9 T, a quadrupole splitting (ΔE_Q) of zero mm/s and an isomer shift (δ) of zero mm/s. The hyperfine parameters for Fe foil are in good agreement with previous studies [54, 70] where values of B_{hf} = ~33.0 T, δ = zero and ΔE_Q = zero were cited.

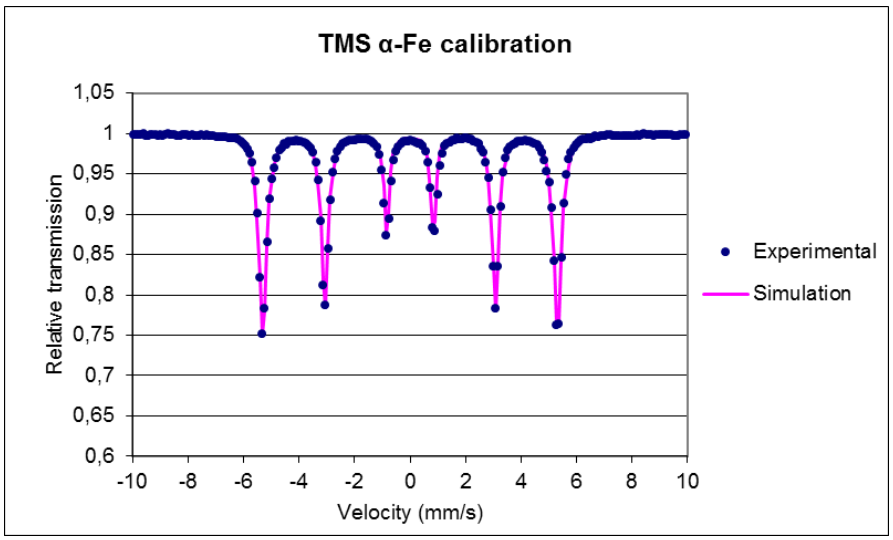

Figure 4.23: TMS spectrum for Fe foil.

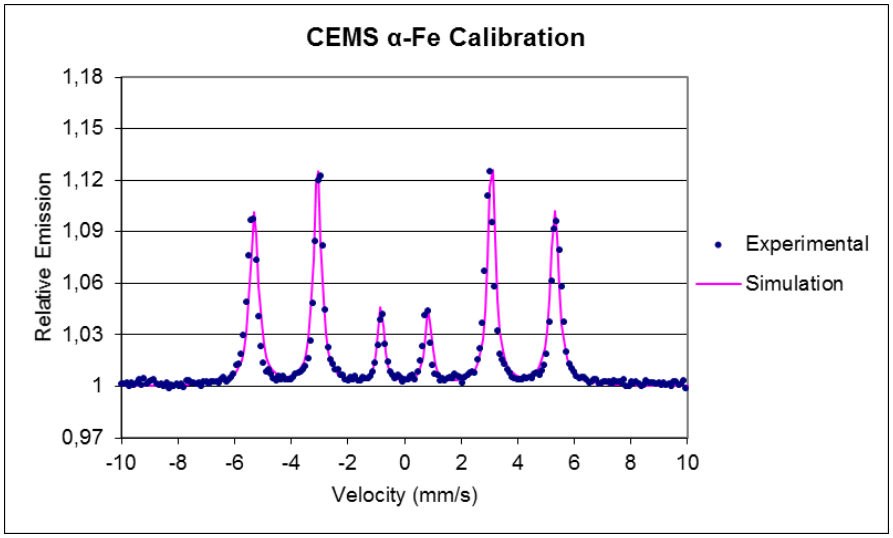

Figure 4.24: CEMS spectrum for Fe foil.

4.5.2 TMS results for the milled powders

Transmission Mössbauer Spectroscopy (TMS) measurements were performed on the milled powders containing Fe in the binder composition, namely, WC-10Fe, WC-7Fe3Ni and WC-8.5Fe1.5Mn alloys. For each powder sample, measurements were carried out over a period of 72 hours, and the corresponding Mössbauer spectra are shown in Figure 4.25.

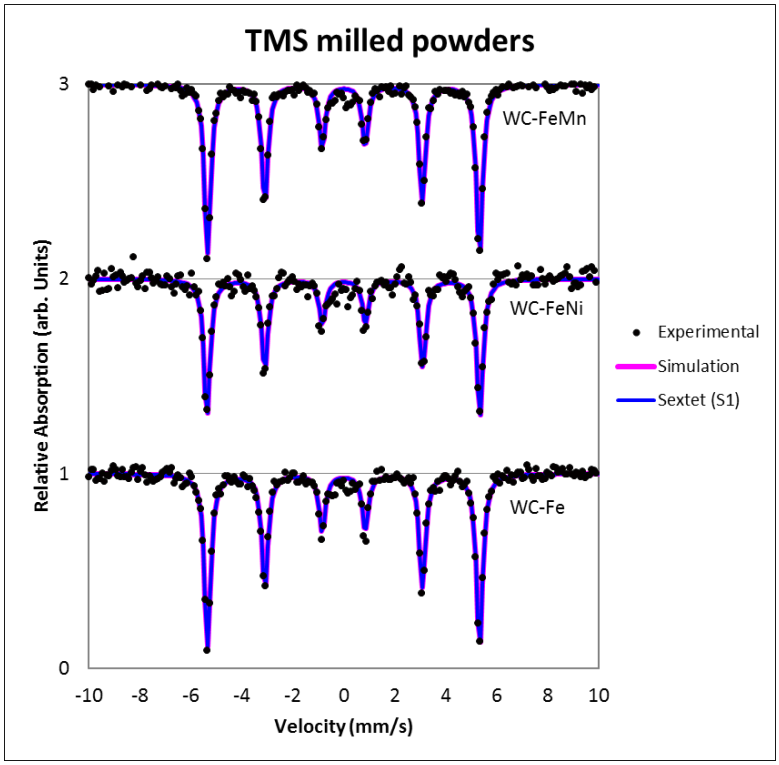

Figure 4.25: TMS spectra for the WC-Fe, WC-FeNi and WC-FeMn milled powders.

Best fits to the Mössbauer data for each spectrum were achieved with one Lorentzian sextet (S1) component with a linewidth, Γ = 0.27 mm/s. The hyperfine parameters are summarised in Table 4.8. The spectral components fitted to the data will be identified in terms of the binder composition due to the different binder metals investigated e.g. $S1_{Fe}$ refers to a six-line pattern for WC-Fe.

Table 4.8: Hyperfine parameters for the milled powders.

Sample	Component	δ mm/s	ΔE_Q mm/s	B_{hf} T
1. WC-Fe	$S1_{Fe}$	0.00(2)	0.00(4)	33.0(1)
2. WC-FeNi	$S1_{FeNi}$	0.00(4)	0.00(4)	33.1(2)
3. WC-FeMn	$S1_{FeMn}$	0.00(2)	0.00(3)	33.0(1)

The hyperfine interaction parameters determined from the fits to the data for all milled powder samples are: B_{hf} = ~33.0 T and δ = 0 mm/s and ΔE_Q = 0 mm/s,

similar to the values determined for α-Fe from the calibration spectra. The Mössbauer results are consistent with the XRD data for the milled powders which show the presence of the Fe-phase in the powders as α-Fe (Table 4.7 and Figures 4.18 to 4.20). This suggests that the laboratory scale ball milling procedure described in Section 3.2.2 is a gentle process mainly used to homogenise the powder mixtures with no mechanical alloying taking place. In contrast, the high energy ball milling process which is a solid state processing technique results in mechanical alloying or mechanosynthesis [23, 24] of the powders where phase transformations occur in the powders during extended milling times. Wang *et al.* [23] achieved the formation of WC by high energy ball milling tungsten metal and activated carbon with stainless steel balls using milling times up to 310 hours. The authors observed two sextets with magnetic fields of 33.0 T and 20.5 T, which were correlated to α-Fe and Fe_3C, respectively.

4.5.3 CEMS results on sintered carbides

CEMS measurements were performed on ~1 mm thick, cut and polished sections of the WC-Fe, WC-FeNi and WC-FeMn materials sintered at temperatures of 1340 °C, 1430 °C and 1510 °C. For each sample, data was collected over a period of ~12 days. All spectra were characterised by broadened six-line patterns. Several models utilising different spectral components were initially fitted using the Vinda package however best fits to the data were achieved with a distribution of Lorentzian sextets with varying magnetic fields, as well as quadrupole-split doublets and single lines where applicable.

4.5.3.1 WC-10Fe

The Mössbauer spectra for the WC-10Fe materials sintered at different temperatures are shown in Figure 4.26. The CEMS spectra were fitted with two magnetic fields ($S1_{Fe}$ and $S2_{Fe}$) and their hyperfine parameters are given in Table 4.9.

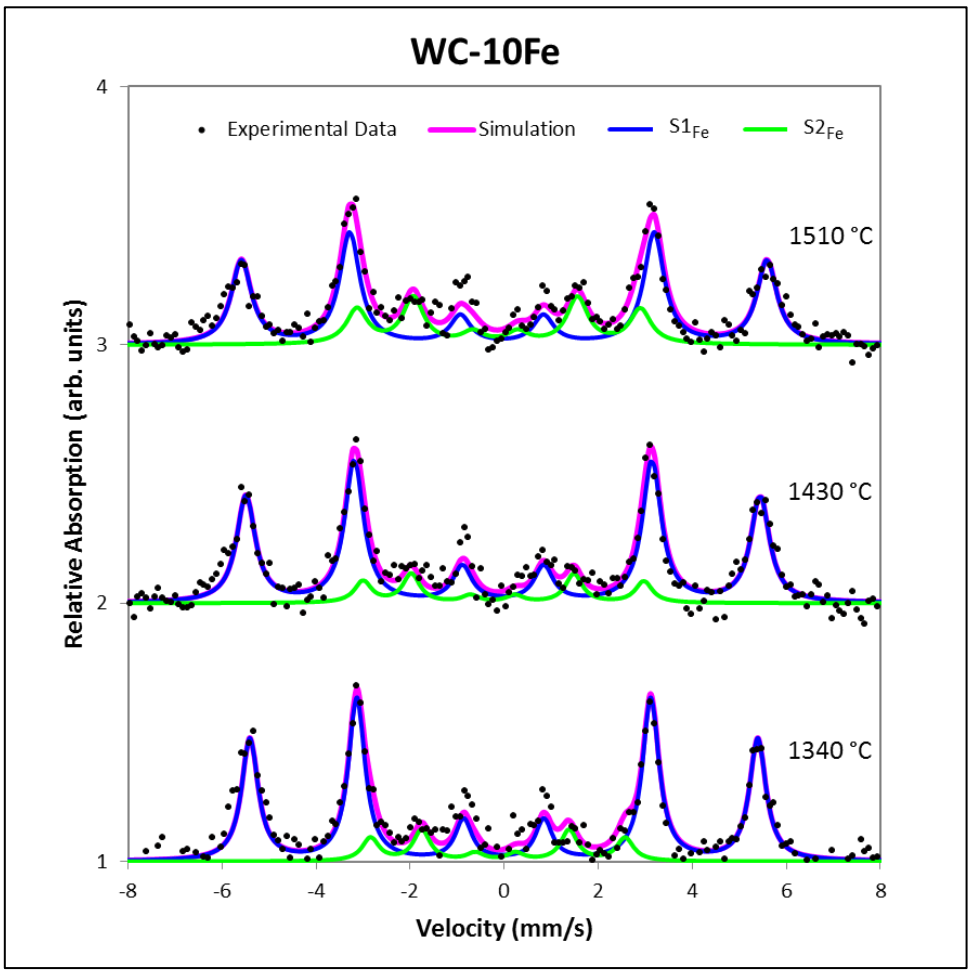

Figure 4.26: CEMS spectra for the WC-10Fe material sintered at 1340 °C, 1430 °C and 1510 °C.

Table 4.9: Hyperfine parameters for WC-10Fe materials sintered at different temperatures.

Temp. (°C)	Component	B_{hf} (T)	δ (mm/s)	ΔE_Q (mm/s)	Area (%)
1340	$S1_{Fe}$	33.4 (5)	-0.01 (7)	0.00 (2)	84 (3)
	$S2_{Fe}$	16.8 (5)	-0.16 (5)	0.05 (9)	16 (2)
1430	$S1_{Fe}$	33.8 (6)	-0.03 (8)	0.00 (2)	85 (3)
	$S2_{Fe}$	18.5 (3)	-0.13 (3)	0.23 (6)	15 (2)
1510	$S1_{Fe}$	34.6 (8)	-0.02 (1)	0.05 (2)	70 (3)
	$S2_{Fe}$	18.7 (2)	-0.15 (2)	0.07 (5)	30 (2)

The spectral features for all the WC-10Fe samples sintered at the different temperatures are very similar. For the 1340 °C sample, the hyperfine interaction parameters ($S1_{Fe}$) determined from the fits to the data are: B_{hf} = 33.4(5) T, $\delta = -0.01$ (7) mm/s and ΔE_Q = 0.00 (9) mm/s and is assigned to an α-Fe phase which is also indicated by the XRD results shown in Table 4.7. It is likely that the α-Fe phase contains dilute W in solution as a result of liquid phase sintering. Idczak *et al*. [71] reported a similar magnetic field of 32.9 T for a Fe-alloy containing <1% W. Comparable parameters were obtained for the 1430 °C spectrum, however a slightly higher magnetic field of 34.6(8) T was obtained for the 1510 °C spectrum which can be explained in terms of the higher sintering temperature where an increase of W in solution is expected [49] as discussed in Section 4.2.2. In the spectra for the WC-Fe materials sintered at 1340 °C and 1430 °C, the spectral component $S1_{Fe}$ dominates the spectra contributing ~85% of the spectral area with $S2_{Fe}$ having the remaining fraction. For the material sintered at 1510 °C, the area fraction of $S2_{Fe}$ increases to 30% with a corresponding decrease of ~15% for the $S1_{Fe}$ component.

The magnetic component $S2_{Fe}$, present in these samples with magnetic fields ranging from 16.8 T to 18.5 T, can be assigned to the formation of a (FeW)C phase. During sintering some W and C dissolve into the Fe binder, hence lowering the hyperfine magnetic field. A similar magnetic field was observed by Mercado *et al*. [24] after 5 hrs of high energy ball milling of Fe, W, and C powders. These authors fitted the acquired Mössbauer spectrum for the milled powders with a distribution of sextets. One of the sextets had similar hyperfine parameters to $S2_{Fe}$ with values of B_{hf} = 17.3 T, δ = 0.06 mm/s and $\Delta E_Q = -0.27$ mm/s, and the other sextets reported had magnetic fields of 26.9 T and 10.9 T.

4.5.3.2 WC-7Fe3Ni

The Mössbauer spectra for the WC-FeNi materials sintered at different temperatures are shown in Figure 4.27, and the hyperfine parameters are summarised in Table 4.10. The Mössbauer spectrum for the sample sintered at the lowest temperature 1340 °C is fitted with a paramagnetic doublet ($D1_{FeNi}$) and a

weak magnetic field ($S3_{FeNi}$). The hyperfine parameters extracted for $D1_{FeNi}$ are δ = −0.08 mm/s and ΔE_Q = 0.00 mm/s, and for $S3_{FeNi}$ are B_{hf} = 15.7 T, δ = −0.28 mm/s and ΔE_Q = −0.14 mm/s. The spectral component $D1_{FeNi}$ dominates the spectrum with an area fraction of 65%. The XRD results shown in Table 4.7 indicates the formation of a γ-Fe_3Ni_2 phase after sintering. Abdel-Fatah *et al*. [72] investigated Fe-Ni alloys using Mössbauer spectroscopy and reported a single line with, δ = −0.08 mm/s assigned to γ-FeNi for a 70/30 Fe/Ni ratio. At a higher Fe/Ni ratio (65/35), these authors also observed a sextet B_{hf} = 16.3 T, δ = −0.03 mm/s corresponding to high spin γ-FeNi, therefore the spectral component $S3_{FeNi}$ in this work can tentatively be assigned to same phase.

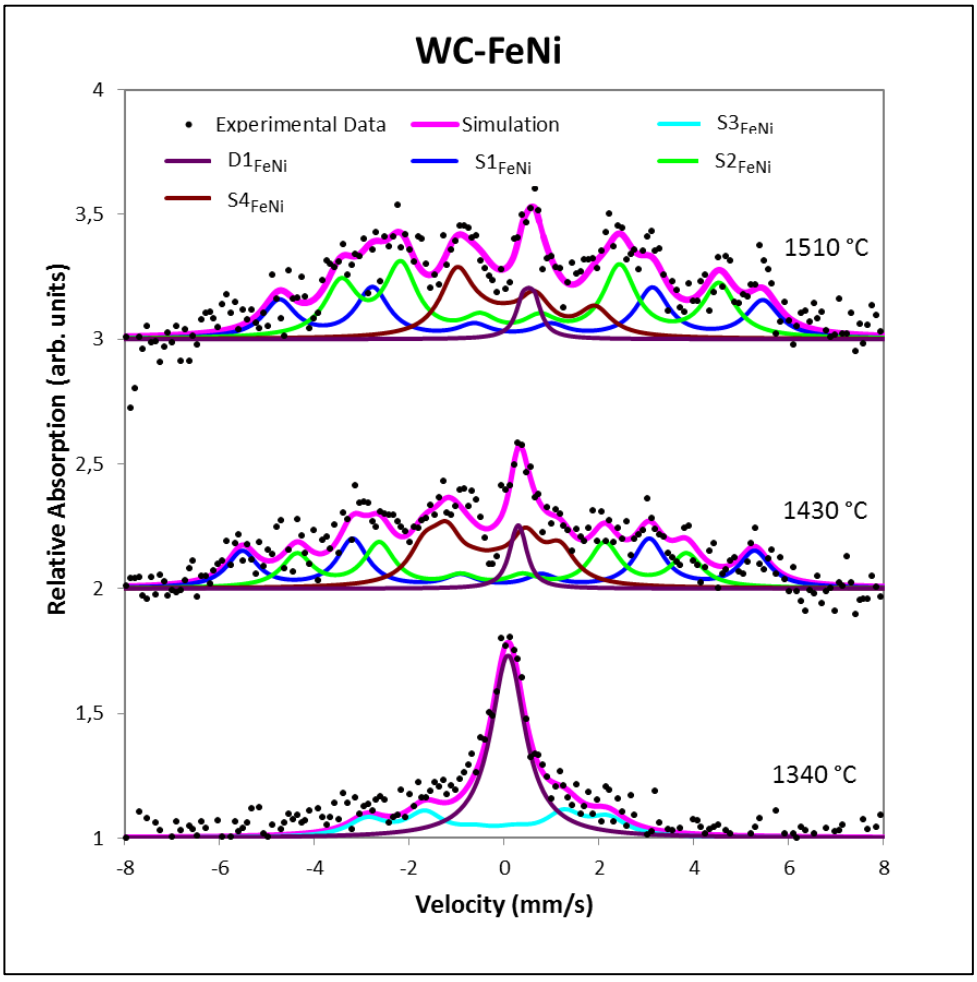

Figure 4.27: CEMS spectra for the WC-FeNi materials sintered at 1340 °C, 1430 °C and 1510 °C.

Table 4.10: Hyperfine parameters for WC-FeNi materials sintered at different temperatures.

Temp. (°C)	Component	B_{hf} (T)	δ (mm/s)	ΔE_Q (mm/s)	Area (%)
1340	$D1_{FeNi}$	-	0.08 (2)	0.00 (3)	65 (2)
	$S3_{FeNi}$	15.7 (7)	-0.28 (10)	-0.14 (15)	35 (1)
1430	$S1_{FeNi}$	33.4 (4)	0.10 (5)	-0.05 (9)	33 (2)
	$S2_{FeNi}$	25.4 (5)	-0.26 (6)	0.00 (10)	30 (2)
	$S4_{FeNi}$	8.8 (5)	-0.32 (7)	0.13 (10)	31 (2)
	$D1_{FeNi}$	-	0.29 (5)	0.00 (3)	6 (1)
1510	$S1_{FeNi}$	31.6 (7)	0.26 (9)	0.18 (12)	30 (2)
	$S2_{FeNi}$	24.7 (4)	0.33 (5)	0.42 (8)	43 (3)
	$S4_{FeNi}$	8.9 (6)	0.14 (8)	0.67 (2)	22 (1)
	$D1_{FeNi}$	-	0.51 (7)	-0.22 (12)	5 (1)

The Mössbauer spectra for the WC-FeNi samples sintered at 1430 °C and 1510 °C were fitted with a distribution of magnetic fields ($S1_{FeNi}$, $S2_{FeNi}$ and $S4_{FeNi}$). For the higher sintering temperature >1340 °C, the magnetic hyperfine field components dominate the spectra occupying ~95% of the spectral area whilst the paramagnetic doublet ($D1_{FeNi}$) decreases from a fraction of 65% to 5%. The magnetic field $S1_{FeNi}$ (33.4 T and 31.6 T) is consistent with α-FeNi phase as observed by Abdel-Fatah *et al*. [72]. The slightly lower magnetic value (31.6 T) for the sample sintered at the highest temperature could be due to increased W in solid solution with FeNi. The magnetic fields for $S2_{FeNi}$ (25.4 T and 24.7 T) are similar to the high spin γ-FeNi phase observed by Abdel-Fatah *et al*. [72], for a $Fe_{0.65}Ni_{0.35}$ alloy. The weak magnetic field of ~8.8 T for $S4_{FeNi}$ is tentatively assigned to the formation of a γ-(FeNiW)C phase with increased levels of W in solution. Positive isomer shifts (0.29 mm/s and 0.51 mm/s) for the paramagnetic doublet increases with increasing temperature which is possibly due to increased electron density caused by *s*-electrons of Ni and W at the Fe nuclei [73].

4.5.3.3 WC-8.5Fe/1.5Mn

The CEMS spectra for the WC-FeMn alloys are shown in Figure 4.28 and the hyperfine parameters are summarised in Table 4.11. The Mössbauer spectra for the

WC-FeMn alloys sintered at different temperatures are characterised by magnetic-split components with the exception of the spectrum at the lowest sintering temperature of 1340 °C where a single line component is also observed. It should be noted that in the initial analysis of the spectra collected at 1430 °C and 1510 °C, an additional quadrupole doublet was included in the central region, however, this component was excluded from the fits due to poor statistics and warrants future investigations. The isomer shift for the singlet, $SL1_{FeMn}$ was determined as 0.23 mm/s and is provisionally assigned to the η-phase (Fe_2W_2C) as indicated by the XRD results in Table 4.7. For this sintering temperature, three sextets ($S1_{FeMn}$, $S2_{FeMn}$ and $S4_{FeMn}$) were fitted to the data. The spectral component, $S1_{FeMn}$ with a hyperfine field of ≈33.0 T corresponding to α-FeMn was observed at all sintering temperatures. The XRD results for these materials indicated that the binder phase is $\alpha\text{-}Fe_{0.95}Mn_{0.05}$.

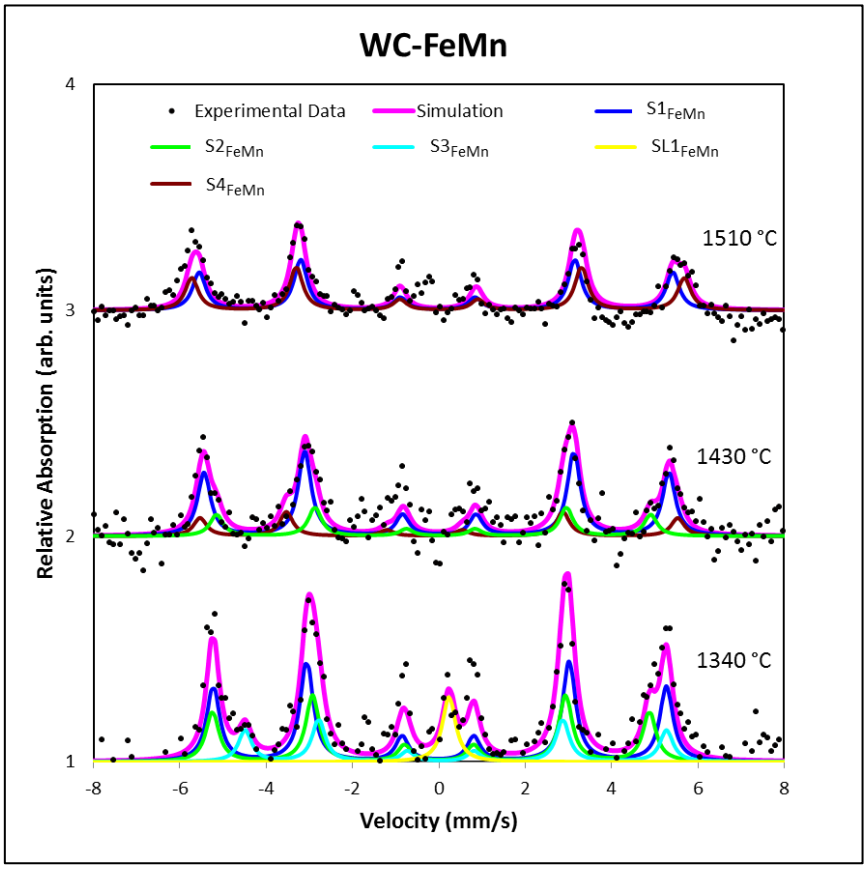

Figure 4.28: CEMS spectra for the WC-FeMn materials sintered at 1340 °C, 1430 °C and 1510 °C.

Table 4.11: Hyperfine parameters for WC-FeMn materials sintered at different temperatures.

Temp. (°C)	Component	B_{hf} (T)	δ (mm/s)	ΔE_Q (mm/s)	Area (%)
1340	$S1_{FeMn}$	32.5 (1)	0.00 (2)	0.04 (4)	44 (7)
	$S2_{FeMn}$	31.3 (2)	-0.09 (2)	-0.19 (5)	30 (4)
	$S3_{FeMn}$	30.2 (3)	0.22 (4)	0.35 (7)	19 (3)
	$SL1_{FeMn}$	-	0.23 (3)	-	7 (1)
1430	$S1_{FeMn}$	33.6 (1)	-0.03 (1)	-0.06 (3)	61 (5)
	$S2_{FeMn}$	31.4 (4)	-0.05 (4)	-0.16 (8)	21 (2)
	$S4_{FeMn}$	34.5 (4)	-0.17 (6)	0.33 (9)	18 (1)
1510	$S1_{FeMn}$	34.0 (1)	-0.05 (1)	-0,.04 (3)	54 (2)
	$S4_{FeMn}$	35.3 (1)	-0.01 (1)	0.02 (3)	46 (2)

The magnetic fields for $S2_{FeMn}$ and $S3_{FeMn}$ were determined to be 31.3 T and 30.2 T, respectively which are most likely due to α-FeMn phases and can be explained in terms of the increasing solid solution of Mn and/or W in the Fe binder. Similar observations were made by Idczak *et al*. [71] for dilute Fe-based alloys. The authors studied the effect of various dilute metals in iron (including Mn and W) using Mössbauer spectroscopy, and reported a magnetic field of 32.8 T for $Fe_{0.99}Mn_{0.01}$ alloy. The authors also cited a decrease in the hyperfine magnetic field with increasing concentration of the alloying element. The magnetic field decreased from 32.8 T for 1%Mn in solution to 31.5 T for 8%Mn.

The spectrum for 1430 °C was also fitted with $S1_{FeMn}$ and $S2_{FeMn}$ but the third sextet component ($S4_{FeMn}$) has been extracted with a hyperfine field of 34.5(4) T. The 1510 °C spectrum was fitted with two sextets, $S1_{FeMn}$ and $S4_{FeMn}$ with a hyperfine value of 35.3 ($S4_{FeMn}$), here $S2_{FeMn}$ is not evident. Idczak *et al*. [71] observed that the magnetic field first decreased when the W content in the Fe-alloy was increased from 1% to 3% concentration, however, the magnetic field increased as the W concentration was further increased to 5%. These observations were explained as the formation of multi-phases at higher concentrations, not just a single solid solution of the two components. This may be a contributing factor to the high magnetic fields >34.5 T obtained for $S4_{FeMn}$ for the WC-FeMn alloy sintered at the two highest temperatures. However, there would be a certain threshold for the

increase in solute atoms, beyond which would result in the decrease in B_{hf} as observed by the presence of the weaker magnetic fields in all the spectra.

At the lowest sintering temperature, the single line ($SL1_{FeMn}$) contributes a small fraction (7%) of the total area, and the remaining fraction is dominated by the magnetic components ($S1_{FeMn}$, $S2_{FeMn}$ and $S3_{FeMn}$). For the other sintering temperatures, the spectra are dominated by the contributions from the magnetic components, however no discernible trends exist for the population of the various magnetic sites.

Chapter 5

Conclusions and Recommendations

5.1 Conclusions

Cemented carbides with Fe-based binders were investigated using Mössbauer spectroscopy. The aim was to determine whether the technique can be used to provide a better understanding of the structural and magnetic properties of the materials, to aid the research and development of new binder grades. The grades selected for this study were WC-10Fe, WC-7Fe3Ni, WC-8.5Fe1.5Mn and WC-10Ni. The Ni grade is a commercialised grade and was selected as a reference material. Powder batches of the various compositions were produced and vacuum sintered at different temperatures (1340 °C, 1430 °C and 1510 °C) in a production furnace at Pilot Tools (Pty) Ltd. The sintered materials were evaluated using the routine cemented carbide quality control testing methods which includes density, magnetic properties, and hardness measurements. The materials were examined using optical and SEM techniques, and investigated using XRD and Mössbauer spectroscopy.

Generally, the carbide quality control results indicate that the optimum sintering temperature for the Fe-based binder materials is 1430 °C. The WC-10Ni grade is known in the literature to have a higher sintering temperature of 1500 °C. The hardness results (1282 HV, 1311 HV and 1320 HV) for the WC-10Fe grade is similar for the different sintering temperatures, indicating a wide sintering temperature window (range), provided the C balance is controlled tightly during the sintering process. This wide sintering window makes the material production friendly. The lower coercivity value (69 Oe) for the WC-Fe grade sintered at the highest temperature (1510 °C) would usually indicate WC grain growth, which is confirmed by the microstructures (Appendix A), and result in a decrease in the hardness property. The hardness however, is maintained at the highest sintering temperature and is possibly due to solid solution strengthening of the binder with increased W and C in solution as indicated by the magnetic saturation results. The

magnetic saturation results drop from 19.1 Gauss.cm^3/g to 17.1 Gauss.cm^3/g as the sintering temperature is increased from 1430 °C to 1510 °C. The Mössbauer spectra for the WC-Fe materials were fitted with two magnetic fields with the dominant magnetic field being α-Fe or more likely α-FeW (≈33 T) and a field assigned to (FeW)C at ≈17 T. At the highest sintering temperature the dominant component has a magnetic field of 35.3 T which could be due to a highly disordered α-Fe lattice and/or the presence of multiple phases of Fe-W-C.

The WC-7Fe3Ni grade has the same hardness value (1250 HV_{30}) as a conventional WC-10Co grade sintered at the optimum temperature of 1430 °C. These results are confirmed by reported literature data for various grades of WC-FeNi and WC-Co hardmetals [17, 18, 63]. The CEMS spectrum for the lowest temperature (1340 °C) FeNi binder sample shows a paramagnetic doublet (δ = −0.08 mm/s and ΔE_Q = 0.00 mm/s) occupying 65% of the total area, and a weak magnetic field (15.7 T). The doublet was assigned to γ-FeNi and the magnetic component to γ-(FeNiW)C. As the sintering temperature is increased, the paramagnetic doublet is reduced to ~5% of the total area and the remainder of the Mössbauer spectrum is characterised by a distribution of magnetic fields (33 T, 25 T and 9 T). These magnetic fields are tentatively assigned to γ-FeNi and multiple phases of FeNiW. The XRD results show a single solid solution phase of Fe_3Ni_2 for all the FeNi binders. The more sensitive Mössbauer results indicate that the FeNi binder may have multiple phases with different concentration levels of W, Ni and C in solution with Fe.

Attempts to produce a WC-8.5Fe1.5Mn were not successful as most of the Mn metal volatilised during the sintering process. The resultant sintered materials contained 0.6 wt%, 0.2 wt% and 0.1 wt% for the samples sintered at 1340 °C, 1430 °C and 1510 °C, respectively as indicated by EDS analysis results (Table 4.6). Also, the sample sintered at 1340 °C contained the undesirable η-phase due to oxidation of the Mn metal in the green compact which was only sintered a few weeks after pressing. The presence of η-phase makes the material hard and brittle, as indicated by the high hardness value (1525 HV_{30}) for this sample compared to a

hardness value of 1337 HV_{30} for the FeMn binder material sintered at 1430 °C. The η-phase is identified by XRD as Fe_2W_2C, and is observed as a paramagnetic single line in the Mössbauer spectrum with a positive isomer shift of 0.23 mm/s. The Mössbauer spectrum also shows a distribution of magnetic components having a range of magnetic fields (32.5 T, 31.3 T and 30.2 T). These magnetic fields occupy 97% of the total area, and are assigned to α-FeMn (32.5 T) and α-FeMnW phases. The magnetic fields for the WC-FeMn sample sintered at the highest temperature are B_{hf} = 35.3 and B_{hf} = 34.0 T could be the result of multi-phases of disordered α-FeMn (W). The combination of issues in the manufacturing the WC-FeMn alloys would not make this material production friendly, as the FeMn binder alloy requires a Mn vapour environment during sintering [1, 2], and has to be sintered immediately after pressing.

5.2 Recommendations

Fe-based binder systems, specifically Fe and FeNi, are regarded as suitable replacements for Co binders in cemented carbide alloys. The findings of this study confirms that Fe and FeNi binders have similar or better hardness properties than Co binders. Mössbauer spectroscopy was used as a new investigative tool for these materials and more work is required to understand some of the Mössbauer hyperfine parameters and collaborate the results. This may include theoretical modelling of the atom arrangement (Ni, W and C) around the ^{57}Fe nuclei to extract hyperfine interaction parameters by investigating the stability of the lattice. High resolution transmission electron microscopy (HRTEM) may be useful in verifying the presence of multi-phases within the metal binder as indicated by the distribution of magnetic fields present in the Mössbauer spectra. The HRTEM technique may also provide a better understanding for the increase in the magnetic hyperfine field (B_{hf} >34.0 T) for the materials sintered at the highest temperature of 1510 °C.

Annealing experiments at different temperatures to relieve residual stresses after sintering would be useful to determine how the hyperfine parameters, specifically

ΔE_Q, will be affected. High temperature annealing (>800 °C) could possibly affect the compositions of some of the complex phases present in the binder.

Appendix A

Microstructures

The microstructures of the carbide alloys sintered at 1340, 1430 and 1510 °C are shown at various magnifications (2000 x and 10000x) in Figures A.1 to A.4. The images at 2000x magnification give an indication of the homogeneity of the phase distributions, whilst the morphology of the WC grains can be observed at the higher magnification (10000 x).

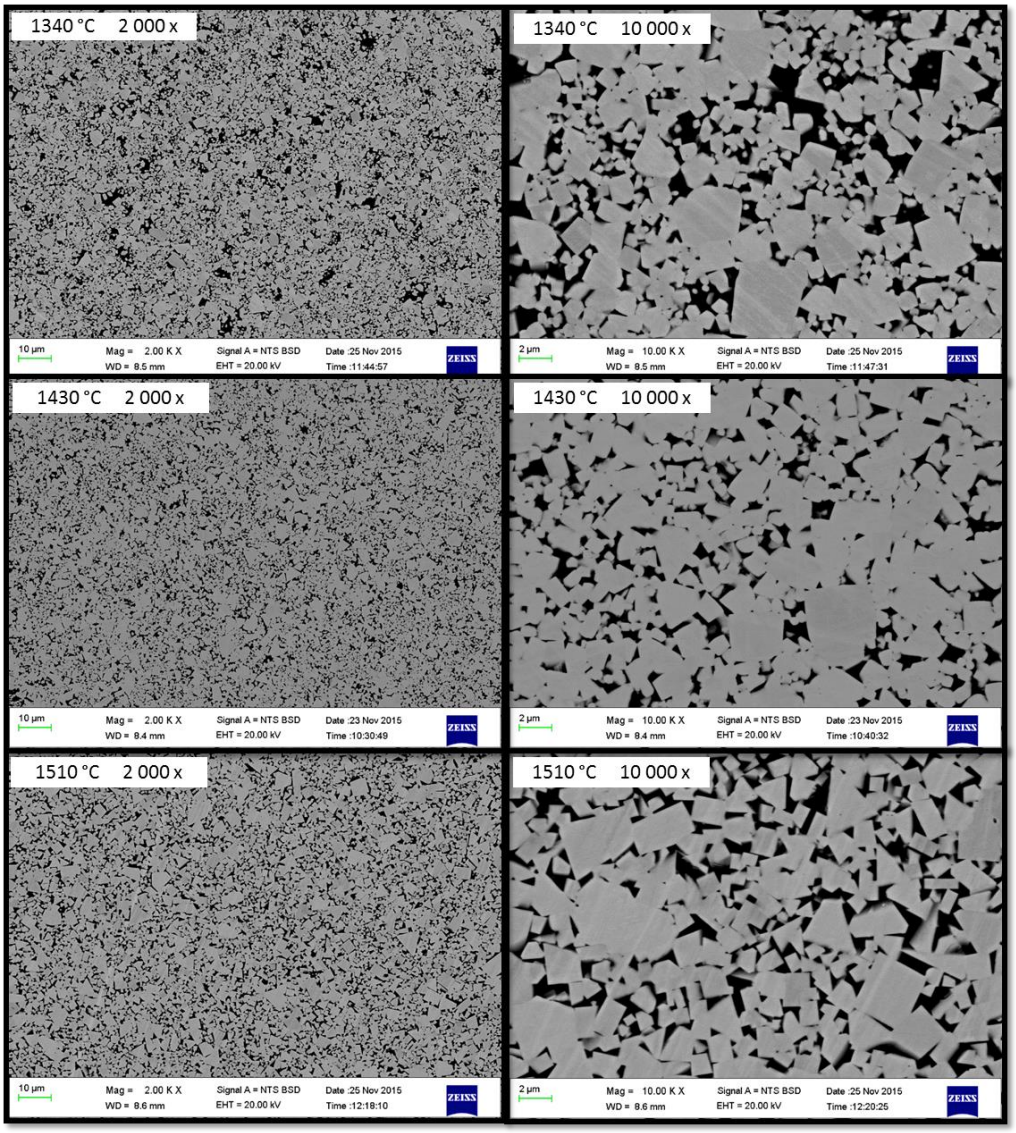

Figure A1: BSE images of WC-Fe alloys sintered at 1340, 1430 and 1510 °C at 2000 x and 10000 x magnifications.

The evolution of the microstructures with increasing sintering temperature cab be observed in Figures A1 to A4 for the different binder grades. There are more large metal binder pools at the low sintering temperature of 1340 °C. The number of large binder pools is significantly reduced at the higher sintering temperatures of 1430 °C and 1510 °C. The metal binder is more uniformly distributed at the higher temperatures. The microstructures show no evidence of abnormal WC grain growth at the highest sintering temperature of 1510 °C, which may be detrimental to the material properties.

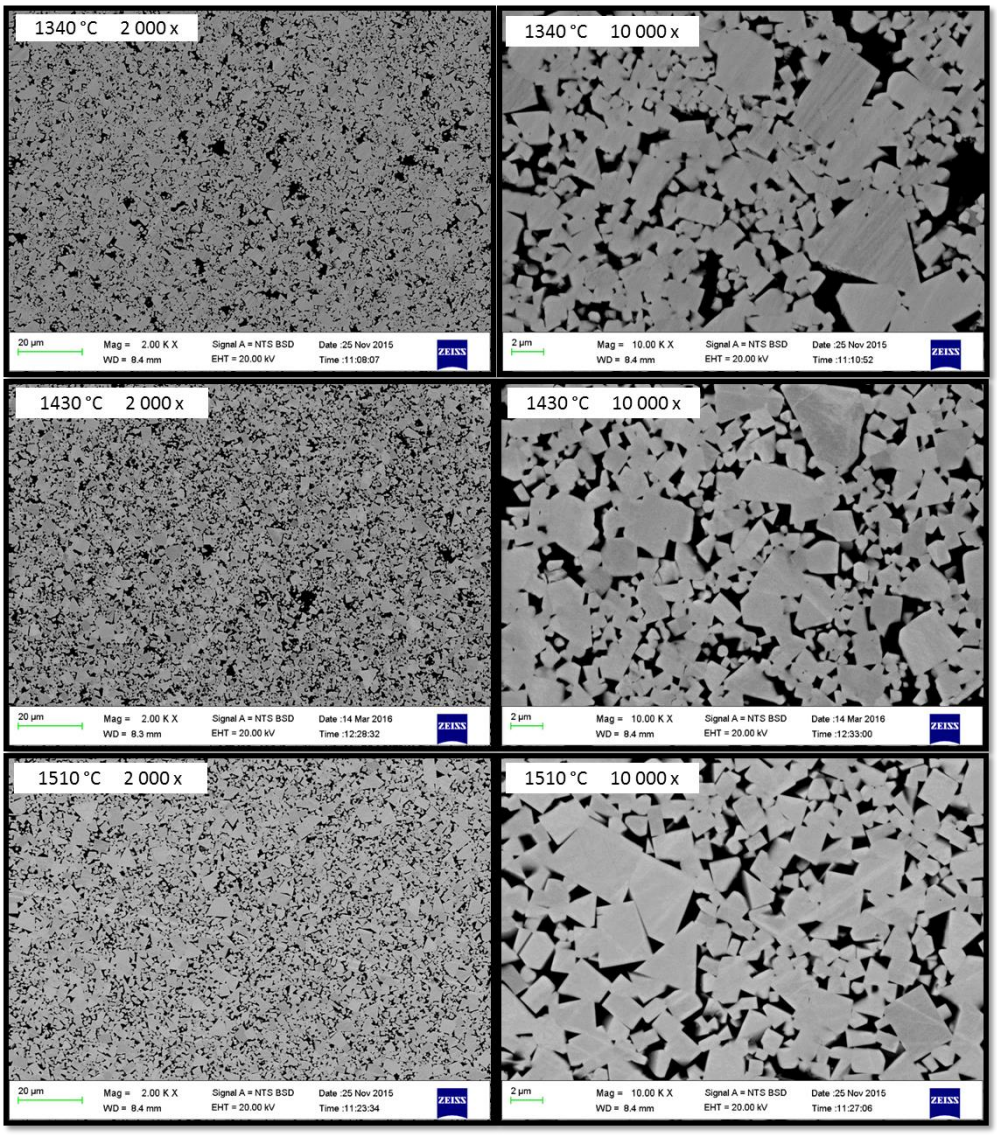

Figure A2: BSE images of WC-FeNi alloys sintered at 1340, 1430 and 1510 °C at 2000 x and 10000 x magnifications.

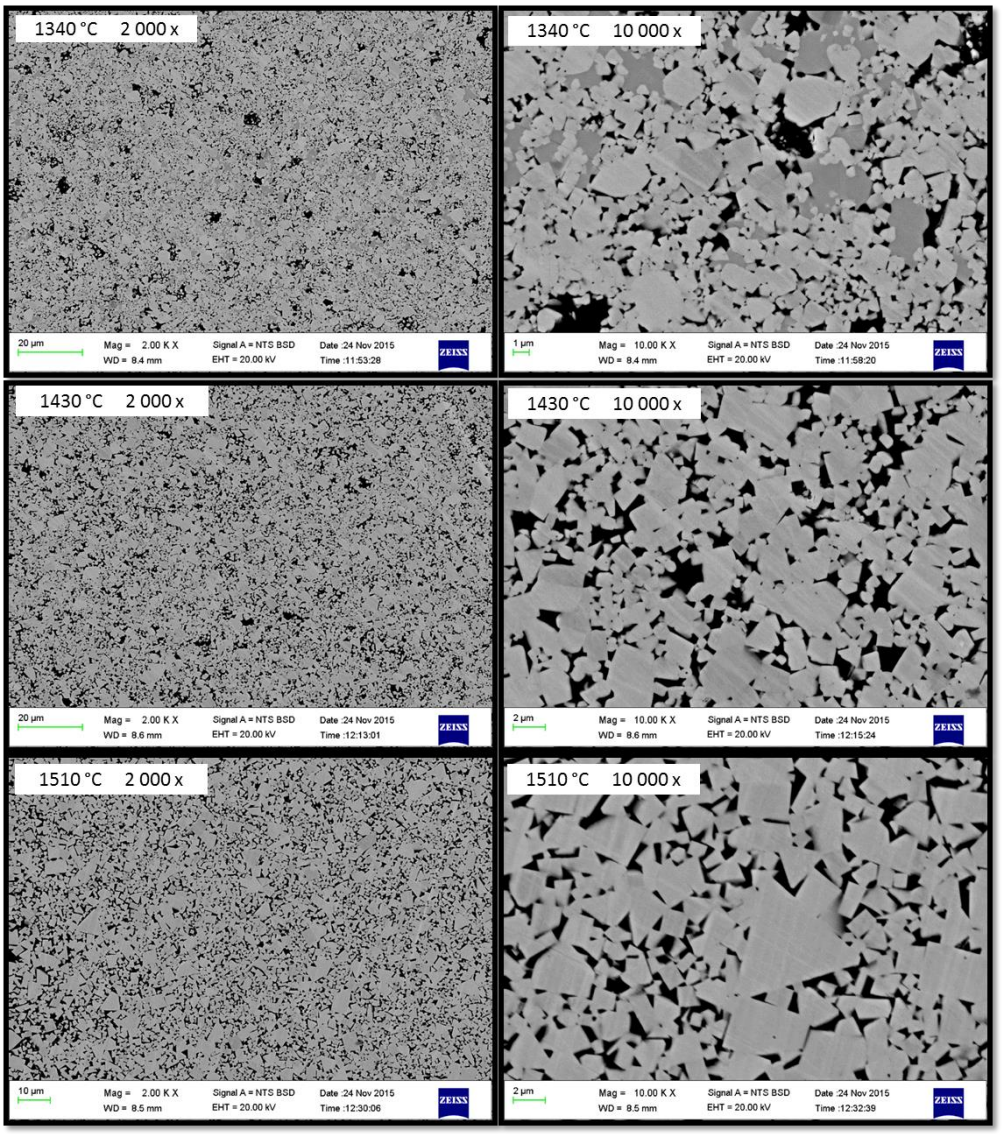

Figure A5: BSE images of WC-FeMn alloys sintered at 1340, 1430 and 1510 °C at 2000 x and 10000 x magnifications.

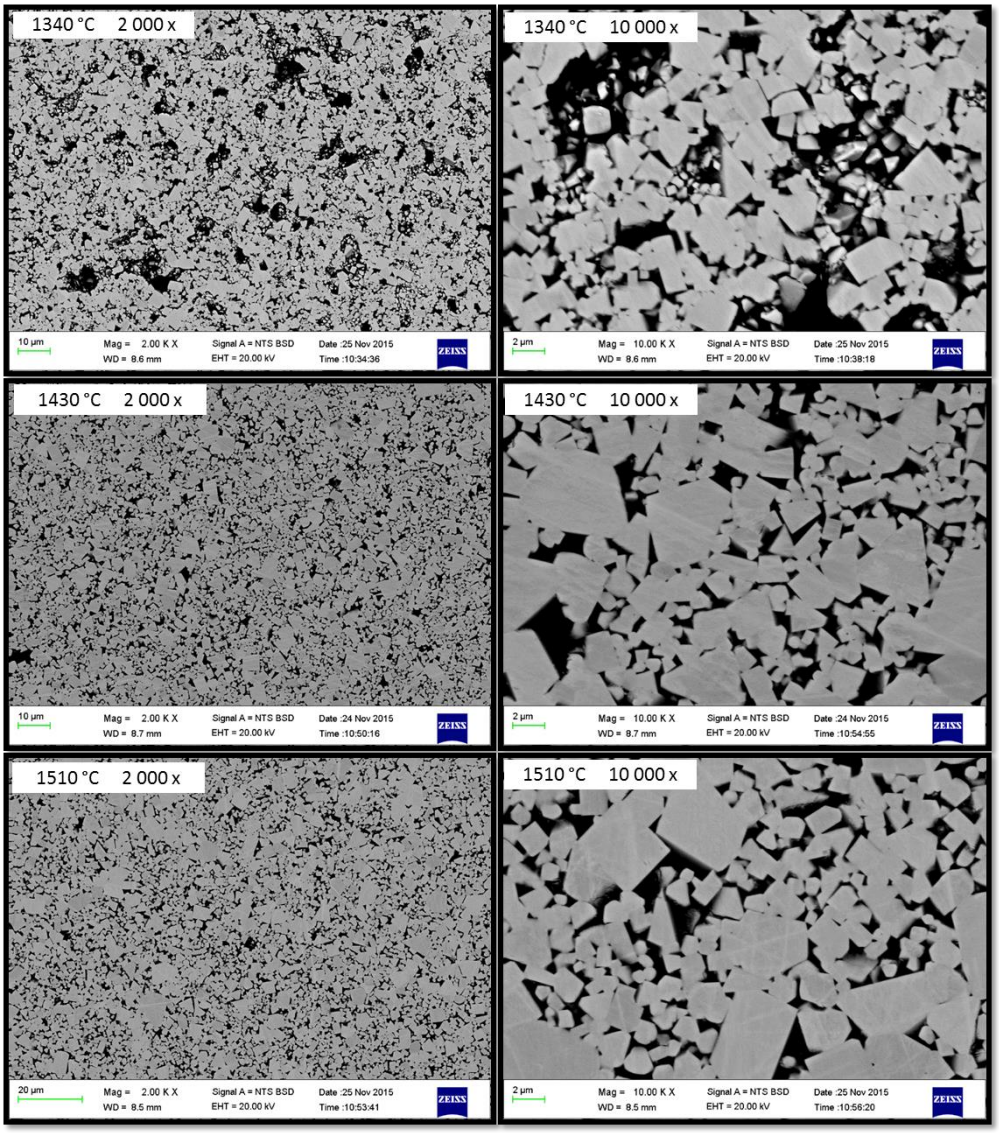

Figure A6: BSE images of WC-Ni alloys sintered at 1340, 1430 and 1510 °C at 2000 x and 10000 x magnifications.

Appendix B

Fitting of Mössbauer spectra

B.1 Single spectrum fitting

The analysis of the Mössbauer spectrum was carried out using Vinda analysis code, which is an Add-In for Microsoft (MS) Excel. After activation of Vinda in MS Excel, an extra tab is added to the ribbon called Vinda D as shown in Figure B1.

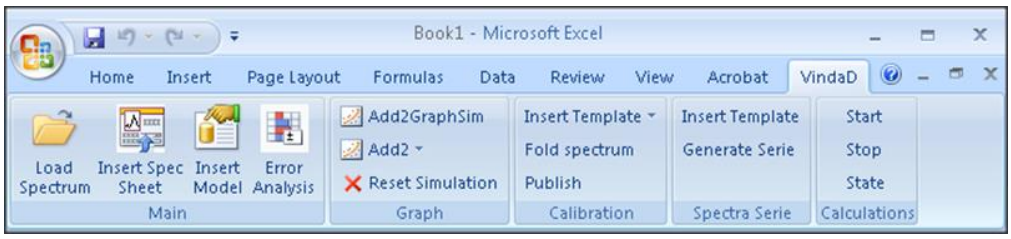

Figure B1: The Vinda D tab in the Excel ribbon.

Analysis of the Mössbauer spectrum takes place in a "Spec-Sheet" as shown in Figure B2.

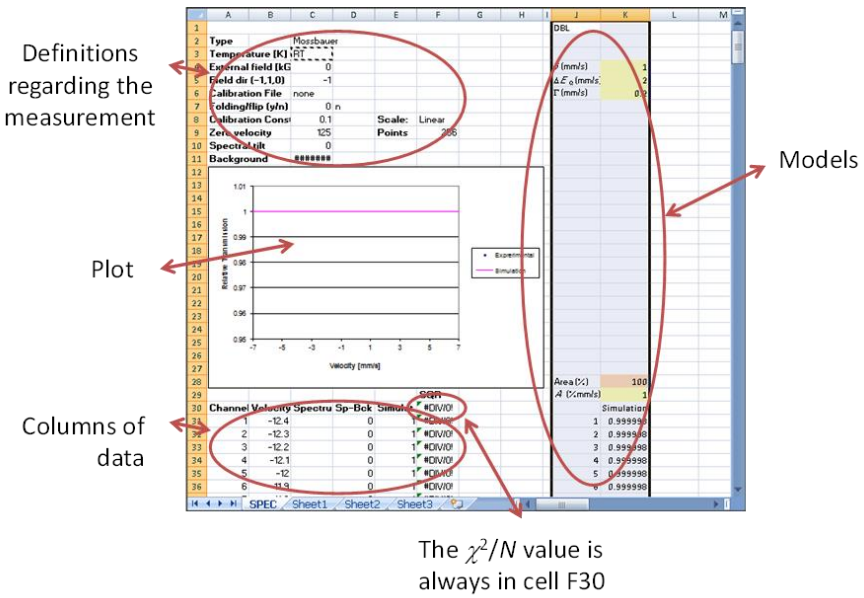

Figure B2: Vinda spec-sheet with explanations of the main fields.

The spectrum is loaded into the Spec-sheet and models are inserted to obtain the desired fit for the components selected. The chi-square value located in cell F30, is minimised by solving the background, hyperfine parameters, line-widths and areas. The solver parameters for the dialog box is shown in Figure B3.

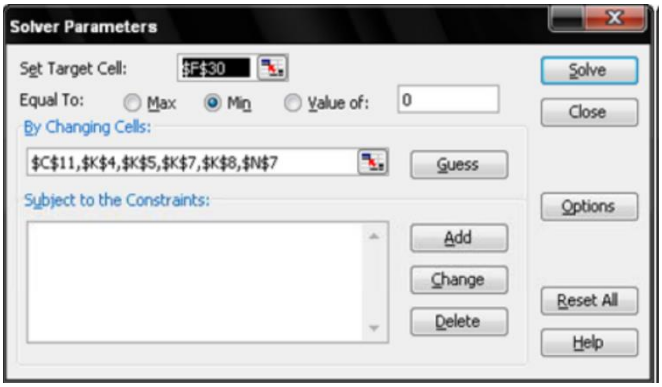

Figure B3: Dialog box for the solver parameters.

An extract of example of fitting a spectrum after inserting a model and solving the parameters is given in Figure B4.

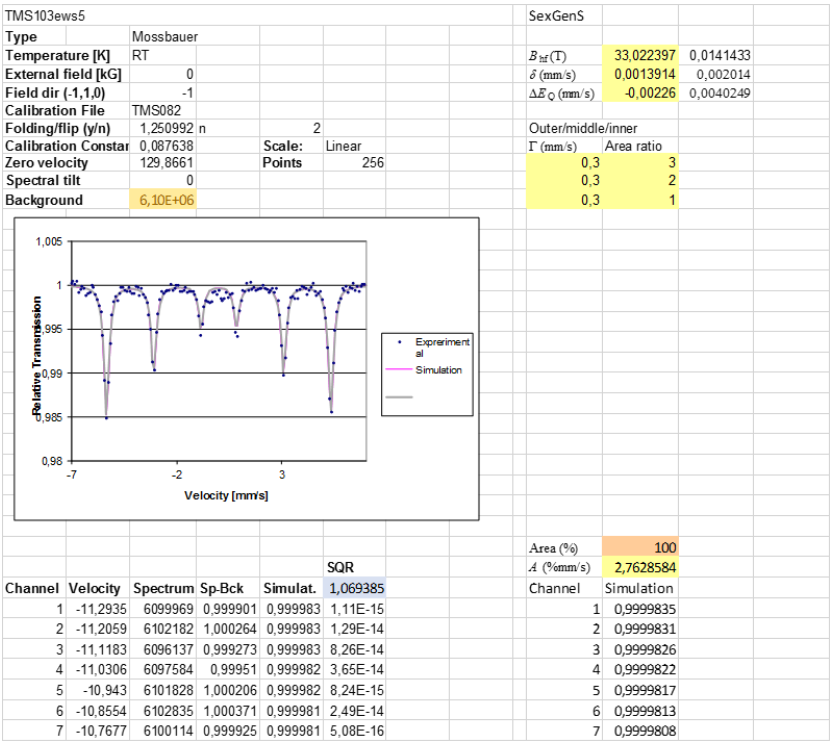

TMS103ews5							SexGenS		
Type		Mossbauer							
Temperature [K]		RT					B_{hf} (T)	33,022397	0,0141433
External field [kG]		0					δ (mm/s)	0,0013914	0,002014
Field dir (-1,1,0)		-1					ΔE_Q (mm/s)	-0,00226	0,0040249
Calibration File		TMS082							
Folding/flip (y/n)		1,250992	n		2		Outer/middle/inner		
Calibration Constar		0,087638		Scale:	Linear		Γ (mm/s)	Area ratio	
Zero velocity		129,8661		Points	256		0,3	3	
Spectral tilt		0					0,3	2	
Background		6,10E+06					0,3	1	
							Area (%)	100	
							A (%mm/s)	2,7628584	
						SQR			
Channel	Velocity	Spectrum	Sp-Bck	Simulat.	1,069385		Channel	Simulation	
1	-11,2935	6099969	0,999901	0,999983	1,11E-15		1	0,9999835	
2	-11,2059	6102182	1,000264	0,999983	1,29E-14		2	0,9999831	
3	-11,1183	6096137	0,999273	0,999983	8,26E-14		3	0,9999826	
4	-11,0306	6097584	0,99951	0,999982	3,65E-14		4	0,9999822	
5	-10,943	6101828	1,000206	0,999982	8,24E-15		5	0,9999817	
6	-10,8554	6102835	1,000371	0,999981	2,49E-14		6	0,9999813	
7	-10,7677	6100114	0,999925	0,999981	5,08E-16		7	0,9999808	

Figure B4: Example of single spectrum fitting.

B.2 Error analysis

The error analysis is based on the chi-square value (cell F30) and is normalised with the number of points as shown by the dialog box given in Figure B5. Reasonable analysis is obtained after running three iterations.

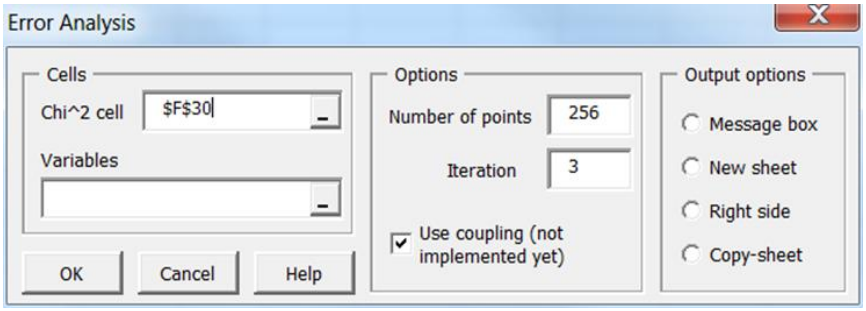

Figure B5: Error analysis dialog box.

The chi-square value (x^2) is defined by the following equation

$$x^2 = \sum_{i=1}^{N} \frac{(Data_i - Simulation_i)^2}{Data_i}$$

The value displayed in the worksheets is this value normalised by the number of points. As x^2 = 1 signifies a perfect fit, the number of points has to be supplied to the error analysis dialog box.

References

[1] Hanyaloglu, C., Aksakal, B. and Bolton, J.D., "Production and indentation analysis of WC/Fe-Mn as an alternative to cobalt-bonded hardmetals," *Materials Characterisation,* vol. 47, pp. 315-322, 2001.

[2] Shubert, W.D., Fugger, M., Wittmann, B. and Useldinger, R., "Aspects of sintering of cemented carbides with Fe-based binders," *Internation Journal of Refractory Metals and Hard Materials,* vol. 47, pp. 315-322, 2014.

[3] Wittmann, B., Schubert, W. and Lux, B., "WC grain growth and grain growth inhibition in nickel and iron binder hardmetals," *International Journal of Refractory and Hard Materials,* vol. 20, pp. 51-60, 2002.

[4] Upadhyaya, G. S., Cemented Tungsten Carbides - Production, Properties and Testing, New Jersey: Noyes Publications, 1998.

[5] Waldorf, D., Lui, S., Stender, M. and Norgan, D., "Alternate Binder Carbide Tools for Machining Superalloys," in *Proceedings of the International Conference on Manufacturing Science and Engineering,* Illinois, 2008.

[6] Norgren, S., Garcia, J., Blomqvist, A. and Yin, L., "Trends in the PM hard metal industry," *International Journal of Refractory Metals and Hard Materials,* vol. 48, pp. 31-45, 2014.

[7] Fernandes, C.M. and Senos, A.M.R., "Cemented carbide phase diagrams: A review," *International Journal of Refractory Metals and Hard Materials,* vol. 29, pp. 405 - 418, 2011.

[8] Maccio, M.R. and Berns, H., "Sintered hardmetals with iron-manganese binder," *Powder Metallurgy,* vol. 55, no. 2, pp. 101 - 109, 2012.

[9] Sarin, V.K., Mari, D. and Llanes, L., Comprehensive Hard Materials Volume 1 Hardmetals, Oxford, UK: Elsevier, 2014.

[10] Uhrenius, B., Pastor, H. and Pauty, E., "On the composition of Fe-Ni-Co-WC based cemented carbides," *Internation Journal of Refractory Metals and Hard Materials,* vol. 15, pp. 139 - 149, 1997.

[11] Ojo-Kupoluyi, O.J., Tahir, S.M., Baharudin, B.T.H., Azmah Hanim, M.A., Anuar, M.S., "Mechanical properties of WC-based hardmetals bonded with iron alloys - a review," *Materials Science and Technology,* vol. 33, pp. 507 - 517, 2016.

[12] Tracy, V., "Nickel in Hardmetals," *Refractory and Hard Materials,* vol. 11, pp. 137 - 149, 1992.

[13] National Physical Laboratory, "Measurement Good Practice Guide No. 20 Mechanical Tests for Hardmetals," Queen's Printer, Scotland, 2009.

[14] Setaram Instrumentation, "Sigmameter instruction manual," Caluire.

[15] Lassner, E. and Schubert, W-D., Tungsten - Properties, Chemistry, Technology of the Element, Alloys, and Chemical Compounds, New York: Springer US, 1999.

[16] Karbasi, M.I., Karbasi, M.A., Saidi, A. and Fathi, M.H., "The effect of sintering temperature on microstructure and hardness of milled WC- 20 Wt.% equiatomic (Fe,Co) cemented carbides," *Journal of Advanced Materials and Processing,* vol. 3, no. 1, pp. 29 - 38, 2015.

[17] Chang, S-H. and Chen, S-L., "Characterisation and Properties of sintered WC-Co and WC-Fe-Ni hard metal alloys," *Journal of Alloys and Compounds,* vol. 585, pp. 407-413, 2014.

[18] Gonzalez, R., Echeberria, J., Sanchez, J.M. and Castro, F., "WC-(Fe,Ni,C) hardmetals with improved toughness through isothermal treatments," *Journal of Materials Science,* vol. 30, pp. 3435 - 3439, 1995.

[19] Shon, I.J., Jeong, I.K., Ko, I.Y., Doh, J.M. and Woo, K.D., "Sintering behaviour and mechanical properties of WC-10Co, WC-10Ni and WC-10Fe

hard materials produced by high-frequency induction heated sintering," *Ceramic International*, vol. 35, pp. 339 - 344, 2009.

[20] Royal Society of Chemistry, "Introduction to Mössbauer Spectroscopy," [Online]. Available: http://www.rsc.org/Membership/Networking/InterestGroups/MossbauerSpect/part1.asp.

[21] Maluba-Bafubiandi, A., "Mössbauer spectroscopy study of mechanically alloyed Fe2O3-(Al, Co and WC) systems," *Hyperfine Interact*, pp. 1017-1022, 2006.

[22] Banganayi, C., Mulaba-Bafubiandi, A. and Luyckx, S., "On the formation of CoFe2O4 when drilling hematite with WC-Co drill bit inserts," *International Journal of Refractory Metals and Hard Materials*, vol. 24, pp. 177-182, 2005.

[23] Wang, G.M., Cambell, S.J., Calca, A. and Kaczmarek, W.A., "Synthesis and structural evolution of tungsten carbide prepared by ball milling," *Journal of Materials Science*, vol. 32, pp. 1461 - 1467, 1997.

[24] Mercado, W.B., Cuevas, J., Castro, I.Y., Fajardo, M., Perez Alcazar, G.A. and Sanchez Sthepa, H., "Synthesis and characterization of Fe6W6C by mechanical alloying," *Hyperfine Interactions*, vol. 175, pp. 49 - 54, 2007.

[25] Sufianu, A., *MSc Dissertation - A Mössbauer Spectroscopy Investigation of Fe enriched WC-Co*, Johannesburg: University of the Witwatersrand, 2016.

[26] Ibwanga, M., *MSc Dissertation - Spectroscopic Study of Fe Phases in Cemented Carbides*, Johannesburg: University of the Witwatersrand, 2016.

[27] Gütlich, P., Link, R. and Trautwein, A., Mössbauer Spectroscopy and Transition Metal Chemistry, New York: Springer-Verlag, 1978.

[28] Langford, J.I. and Louër, D., "Powder Diffraction," *Reports on Progress in Physics,* no. 59, pp. 131 - 234, 1996.

[29] West, A., Basic Solid State Chemistry, Ney York: John Wiley and Sons, 1999.

[30] Stanjek, J. and Häusler, W., "Basics of X-ray Diffraction," *Hyperfine Interactions,* vol. 154, pp. 107 - 119, 2004.

[31] Wang, G. and Lu, T., RHEED Transmission Mode and Pole Figures, New York: Springer Science and Business Media, 2014.

[32] Azároff, V., Introduction to Solids, New York: McGraw-Hill, 1960.

[33] Hammond, C., The Basics of Crystallography and Diffraction, Oxford Science Publications, 2001.

[34] Fultz, B. and Howe, J., Transmission Electron Microscopy and Diffractometry of Materials, Berlin: Springer-Verlag, 2013.

[35] Dinnebier, R.E. and Billinge, S.J.L., Powder Diffraction - Theory and Practice, Cambridge: Royal Society of Chemistry, 2008.

[36] Education website; Physics and Radio-Electronics;

http://www.physics-and-radio-electronics.com/physics/magnetism

[37] Royal Society of Chemistry, "Introduction to Mössbauer Spectroscopy," [Online]. Available: http://www.rsc.org/Membership/Networking/InterestGroups/MossbauerSpect/part1.asp.

[38] Mössbauer, R., *Recoilless nuclear resonance absorption of gamma radiation, Nobel Lecture,* 1961.

[39] Seda, T., “Basic theory of the Mössbauer effect,” Western Washington University, [Online]. Available: http://courses.washington.edu/phys431/Mössbauer/Mössbauer.pdf.

[40] Yang, Q. and Chen, C., “Mössbauer Spectroscopy,” in *Nuclear Analytical Techniques for Metallomics and Metalloproteomics*, Royal Society of Chemistry, 2010, p. Chap.5.

[41] Melissisinos, A., Experiments in Modern Physics, New York: Academic Press, 1968.

[42] Devanarayanan, S., “Mössbauer Spectroscopy,” in *Refresher Course in Physics for College Teachers*, Kerala, 2011.

[43] Chen, Y and Yang, D., Mössbauer Effect in Lattice Dynamics, Weinheim: Wiley-VCH, 2007.

[44] Gütlich, P. and Garcia, Y., “Chemical Applications of Mössbauer Spectroscopy,” in *Mössbauer Spectroscopy Tutorial Book*, Berlin, Springer-Verlag, 2013, pp. 23-90.

[45] Yoshida, Y. and Langouche, G., Mössbauer Spectroscopy, Berlin: Springer-Verlag, 2013.

[46] Luyckx, S., *An Introduction to Hardmetals Lecture notes*, Johannesburg: University of the Witwatersrand, 2005.

[47] Gallant, R., “Physical Properties of Hydrocarbons,” Gulf Publishing, Houston, 1968.

[48] Exner, H., “Physical and chemical nature of cemented carbides,” *International Metals Review, No. 4*, pp. 149-173, 1979.

[49] Roebuck, B., Gee, M., Bonnett., E.G. and Morrel, R., Mechanical tests for hardmetals; Measurement good practice guide No.20, Middlesex: Queen's Printer, 2009.

[50] International Organisation for Standardisation, *ISO3369 Impermeable sintered metals and hardmetals - Determination of density,* 2006.

[51] Institut Dr Foerster, "Koerzimat 1095 manual," Reutlingen, 2014.

[52] England, G., "Hardness Test," [Online]. Available: http://www.gordonengland.co.uk/hardness/vickers.htm.

[53] International Organisation for Standardisation, *ISO3878 Hardmetals - Vickers hardness test,* 1983.

[54] Longworth, G. and Window, B., "The preparation of narrow-line Mössbauer sources of 57Co in metallic matrices," *Journal of Appl. Physics,* vol. Vol. 4, pp. 835 - 839, 1971.

[55] Dickson, D. and Berry, F., Mössbauer Spectroscopy, Cambridge: Cambridge University Press, 1986.

[56] Kelly, J., "The Mössbauer Effect, Physics 121 Lecture notes, University of California Irvine," [Online]. Available: http://www.physics.uci.edu/advanlab/mossman1.pdf.

[57] Wissenschaftliche Elektronik GMBH, *Data Acquisition Module CMCA-550 Instruction Manual,* Starnberg Germany, 2004.

[58] Kuzmann, E., Homonnay, Z., Nagy, S. and Nomura, K., Mössbauer Spectroscopy Handbook of Nuclear Chemistry, vol. Chap.25, New York: Springer, 2010.

[59] Wissenschaftliche Elektronik GMBH, *Conversion Electron Detector Rikon-5 Instruction Manual,* Stamberg Germany, 1994.

[60] Schlaak, D., "Construction of a Conversion Electron Mössbauer Spectroscopy Detector," Hampden-Sydney College, Sydney, 2013.

[61] Daoush, W.M., Lee, K.H., Park, H.E. and Hong, S.H., "Effect of liquid phase composition on the microstructure and properties of (W,Ti)C

cemented carbide cutting tools," *International Journal of Refractory Metals and Hard Materials,* vol. 27, pp. 83 - 89, 2008.

[62] Ettmayer, P., "Hardmetals and cermets," *Annual Review Materials Science,* vol. 19, pp. 145 - 164, 1989.

[63] Prakash, L., Holleck, H., Thummler, F. and Walter, P., Modern Developments in Powder Metallurgy, vol. 14, 1981, pp. 255 - 268.

[64] Penrice, T., "Alternative Binders for Hardmetals," *J. Mater. Shaping Technol.,* vol. 5, no. 1, pp. 35 - 39, 1987.

[65] Miranda, F., "Nickel in Hardmetals," 2003. [Online]. Available: http://www.ipen.br/biblioteca/cd/ptech/2003/pdf/11.07.pdf.

[66] Morton, C.W., Willis, D.J. and Stjernberg, K., "The temperature ranges for maximum effectiveness of grain growth inhibitors in WC-Co alloys," *Journal of Refractory Metals and Hard Materials,* vol. 23, pp. 287 - 293, 2005.

[67] Fernandes, C.M., Popvich, V., Matos, M., Senos, A.M.R. and Viera, M.T., "Carbide phases formed in WC-M(M=Fe/Ni/Cr) systems," *Ceramics International,* vol. 35, pp. 369 - 372, 2009.

[68] "Principles of Mössbauer Spectroscopy," *Physics and Chemistry of the Earth,* vol. 18, no. 2, pp. 1 - 46, 1992.

[69] Gunnlaughsson, H., *Vinda User Manual,* Cern, 2015.

[70] Violet, C.E. and Pipkorn, D.N., "Mössbauer line positions and hyperfine interactions in α-iron," *Journal of Applied Physics,* vol. 42, pp. 4339 - 4342, 1971.

[71] Idczak, R., Konieczny, R. and Chojcan, J., "Mean hyperfine fields at 57Fe in dilute iron-based alloys studies by Mössbauer spectroscopy," *Nukleonika,* vol. 60, no. 1, pp. 39 - 42, 2015.

[72] Abdel-Fatah, D.L. and Mahmood, S.H., “Mössbauer spectroscopy study of iron and nickel alloys.,” *Hyperfine Interactions,* vol. 139, pp. 387 - 392, 2002.

[73] Kasparova, O.V. and Baldokhin, Y.V., “Hyperfine structure and corrosion-electrochemical behavior of Fe-Ni alloys.,” *Protection of Metals and Physical Chemistry of Surfaces,* vol. 51, no. No. 2, pp. 262 - 266, 2015.

[74] Upadhyaya, G. and Bhaumik, S.K., “Sintering of Submicron WC-10wt%Co Hard Metals containing Nickel and Iron,” *Materials Science and Engineering,* vol. A105/106, pp. 249 - 256, 1988.

[75] Prakash, L., “Global R&D trends in the PM hardmetal Industry,” 2013.

[76] Nasu, S., “General Introduction to Mössbauer Spectroscopy,” in *Mössbauer Spectroscopy Tutorial Book,* Berlin, Springer-Verlag, 2013, pp. 1-22.

[77] Longworth, G. and Hartley, N.E.W., “Mössbauer effect study of nitrogen-implanted iron foils,” *Thin Solid Films,* vol. 48, pp. 95 - 104, 1978.

[78] Gille, G., Bredthauer, J., Gries, B., Mende, B. and Heinrich, W., “Advanced and new grades of WC and binder powder - their properties and application,” *International Journal of Refractory Metals and Hard Materials,* pp. 87-102, 2000.

[79] Devanarayanan, S., “Lecture: Mössbauer Spectroscopy,” 2011. [Online]. Available: http://www.researchgate.net/publication/269039551_Lecture_Mossbauer_Spectroscopy.

[80] Matsuzawa Co. Ltd., “Matsuzawz Product Selection Guide,” [Online]. Available: http://www.matsuzawa-ht.com/us/support/guide.htm.

[81] Dyar, M.D., Agresti, D.G., Schaefer, M.W., Grant, C.A. and Sklute, E.C., “Annu. Rev.Earth Planet. Sci,” vol. 34, no. 8, 2006.

[82] Masenda, H., *PhD Thesis, University of the Witwaterand, 2014* .